Thesis for Doctoral Degree (Ph.D.)
2017

Doctoral Program in Biomedical Engineering

Advanced Bioimpedance Signal Processing Techniques for Hemodynamic Monitoring During Anesthesia

Jesús Escrivá Muñoz

Dissertation Supervisors:

Dr. Erik Weber Jensen, Quantium Medical
Dr. Montserrat Vallverdú Ferrer, Universitat Politècnica de Catalunya

Barcelona, Spain, December 2017

UNIVERSITAT POLITÈCNICA DE CATALUNYA
BARCELONATECH
Departament d'Enginyeria de Sistemes,
Automàtica i Informàtica Industrial

UNIVERSITAT POLITÈCNICA DE CATALUNYA BARCELONATECH

Desarrollo de un kit de control y monitorización telemática de bajo coste para sistemas de energía solar térmica en multivivienda

Aitor González Valero

Assessment Results for the Doctoral Thesis

Academic Year:

Full Name

_____

Doctoral Program

_____

Structural Unit in Charge of the Program

_____

Decision of the Committee

In a Meeting with the examination committee convened for this purpose, the doctoral candidate presented the topic of his Doctoral Thesis entitled

_____

_____.

Once the candidate had defended the thesis and answered the questions put to him, the examiners decided to award a grade of:

☐ FAIL ☐ PASS ☐ GOOD ☐ EXCELLENT

(Full name and signature) Chairperson	(Full name and signature) Secretary	
(Full name and signature) Member	(Full name and signature) Member	(Full name and signature) Member

_____, _____

The votes of the members of the examination committee were counted by the Standing Committee of the Doctoral School, and the result is to award the CUM LAUDE DISTINCTION AUDE:

☐ YES ☐ NO

(Full name and signature) Chair of the Standing Committee of the Doctoral School	(Full name and signature) Secretary of the Standing Committee of the Doctoral School

Barcelona, _____

This page is intentionally left blank.

Universitat Politècnica de Catalunya · Barcelona**TECH**

Department of Automatic Control (ESAII)
Research Center for Biomedical Engineering (CREB)
Bioinformatics and Biomedical Signals Laboratory (B2SLab)
CIBER in Bioengineering, Biomaterials and nanomedicine (CIBER-BBN)

Quantium Medical · **Fresenius Kabi** group

Advanced Bioimpedance Signal Processing Techniques for Hemodynamic Monitoring During Anesthesia

Doctoral Program in Biomedical Engineering

Dissertation Supervisors

Dr. Erik Weber Jensen**,** Quantium Medical
Dr. Montserrat Vallverdú Ferrer**,** Universitat Politècnica de Catalunya

This thesis was supported by the Industrial PhD Program DI-2014/013 (Secretaria d'Universitats i Recerca del Departament d'Economia i Coneixement, Generalitat de Catalunya, Spain), Quantium Medical SL (Spain), and the European Social Fund of the European Union. CIBER of Bioengineering, Biomaterials and Nanomedicine is an initiative of ISCIII.

A mis chicas: mamá, Iris, Charo y Dafne…

This page is intentionally left blank.

Acknowledgement

A famous sportsman once said that no individual can win a game by himself and this Doctoral Thesis is no exception. Performing a Doctoral Thesis in an imbricated environment between a higher education institution and a private company is not a straightforward task and it would have not been possible without the collaboration of many. I wish to express my sincere gratitude to all of them.

First and foremost, I would like to thank Dr. Montserrat Vallverdú Ferrer and Dr. Erik Weber Jensen for the opportunity to join in a research adventure which will definitely have a deep impact on my professional career. I am grateful to them for showing me two complementary professional approaches which have enriched me in many ways.

In Quantium Medical, I would also like to express my deepest appreciation to Carmen González, who has followed my PhD within the qCO project and has offered me countless personal and professional advice which will not be forgotten. Within the company, the qCO project gathered many collaborations which I was happy to enjoy. Here; I would like to mention those who contributed to some of my publications (Alejandro Galea, Eva Gabarrón, Pol Fort) and those who shared valuable input and discussions with me (Joan Fontanet, Dr. Umberto Melià, Daniel Blanch, James Marugg, Patricia Pineda). All in all, the whole QMers' team deserve my acknowledgement for the great time I have been fortunate to enjoy with them: George, Miguel, Joshua, Jamal, Marina, Clàudia, Bea, Rebecca, Aleix…

During this Doctoral Thesis, I have experimented the pleasure of clinical research both in Spain and internationally. I am grateful for the excellent collaboration with Doctor Gambús and his team in Hospital CLINIC in Barcelona, Doctor Yan Pan and her team in Zhongshan Hospital in Shanghai, and Doctor Chan and his team in the Prince of Wales Hospital in Hong Kong. A special thank you is also dedicated to D. Leif Sörnmo and Frida Sandberg for my stay in Lunds Universitet (Sweden).

On the other side of this Doctoral Thesis lies my family and friends. On the one hand, this Doctoral Thesis is dedicated to my family, especially my mother, who has always been courageous to push me further in my career, even despite knowing that «further» often meant physically away from her. On the other hand, this is also dedicated to my second family: my friends, who during the last years have always been there to inspire me and support me around a great Sunday brunch or a drink and much more.

To all of you, thank you.

Abstract

Cardiac output (CO) defines the blood flow arriving from the heart to the different organs in the body and it is thus a primary determinant of global O_2 transport. Cardiac output has traditionally been measured using invasive methods, whose risk sometimes exceeds the advantages of a cardiac output monitoring.

In this context, the minimization of risk in new noninvasive technologies for CO monitoring could translate into major advantages for clinicians, hospitals and patients: ease of usage and availability, reduced recovery time, and improved patient outcome. Impedance Cardiography (ICG) is a promising noninvasive technology for cardiac output monitoring but available information on the ICG signals is more scare than other physiological signals such as the electrocardiogram (ECG).

The present Doctoral Thesis contributes to the development of signal treatment techniques for the ICG in order to create an innovative hemodynamic monitor.

First, an extensive literature review is provided regarding the basics of the clinical background in which cardiac output monitoring is used and concerning the state of the art of cardiac output monitors on the market. This Doctoral Thesis has produced a considerable amount of clinical data which is also explained in detail. These clinical data are also useful to complement the theoretical explanation of patient indices such as heart rate variability, blood flow and blood pressure. In addition, a new method to create synthetic biomedical signals with known time-frequency characteristics is introduced.

One of the first analysis in this Doctoral Thesis studies the time difference between peak points of the heart beats in the ECG and the ICG: the RC segment. This RC segment is a measure of the time delay between electrical and mechanical activity of the heart. The relationship of the RC segment with blood pressure and heart interval is analyzed. The concordance of beat durations of both the electrocardiogram and the impedance cardiogram is one of the key results to develop new artefact detection algorithms and the RC could also have an impact in describing the hemodynamics of a patient.

Time-frequency distributions (TFDs) are also used to characterize how the frequency content in impedance cardiography signals change with time. Since TFDs are calculated using concrete kernels, a new method to select the best kernel by using synthetic signals is presented. Optimized TFDs of ICG signals are then calculated to extract several features which are used to discriminate between different anesthesia states in patients undergoing surgery.

TFD-derived features are also used to describe the whole surgical operations. Relationships between TFD-derived features are analyzed and prediction models for cardiac output are designed. These prediction models prove that the TFD-derived features are related to the patients' cardiac output.

Finally, a validation study for the qCO monitor is presented. The qCO monitor has been designed using some of the techniques which are consequence of this Doctoral Thesis. The main outputs of this work have been protected with a patent which has already been filed.

As a conclusion, this Doctoral Thesis has produced a considerable amount of clinical data and a variety of analysis and processing techniques of impedance cardiography signals which have been included into commercial medical devices already available on the market.

UNESCO codes: 240602 (Bioelectricity), 331110 (Medical Instruments), 241103 (Cardiovascular Physiology).

Resum

La despesa cardíaca defineix el fluix de sang que arriba des del cor als distints òrgans del cos i és, per tant, un determinant primari del transport global d'oxigen. La despesa cardíaca s'ha mesurat tradicionalment emprant mètodes invasius, els riscs dels quals en ocasions excedeixen els avantatges de la monitorització de la despesa cardíaca.

En aquest context, la minimització del risc de la monitorització de la despesa cardíaca en noves tecnologies no invasives podria traduir-se en més avantatges per a metges, hospitals i pacients: facilitat d'ús i disponibilitat de l'equipament, temps de recuperació dels pacients i millors resultats en el pacients. La cardiografia d'impedància (ICG per les seues sigles en anglés) és una tecnologia prometedora i no invasiva per a la monitorització de la despesa cardíaca però la informació disponible sobre els senyals d'ICG és més aviat escassa en comparació amb altres senyals fisiològics com l'electrocardiograma (ECG).

La present Tesi Doctoral contribueix al desenvolupament de tècniques de tractament del de senyal d'ICG per així crear un monitor hemodinàmic innovador.

En primer lloc, es proporciona una extensa revisió bibliogràfica sobre els aspectes bàsics del context clínic en què la monitorització de la despesa cardíaca s'utilitza principalment, així com sobre l'estat de l'art dels monitors de despesa cardíaca que existeixen al mercat. Aquesta Tesi Doctoral ha produït una considerable quantitat de dades clíniques que també s'expliquen en detall. Aquestes dades clíniques també són útils per a complementar les explicacions teòriques dels índexs de pacient de variabilitat cardíaca i de fluix i pressió

sanguínia. A més a més, es presenta un nou mètode de creació de senyals sintètics biomèdics amb característiques de temps-freqüència conegudes.

Una de les primeres anàlisis d'aquesta Tesis Doctoral estudia la diferència temporal entre els pics dels batecs cardíacs de l'ECG i de l'ICG: el segment RC. Aquest segment RC és una mesura del retard temporal entre l'activitat elèctrica i mecànica del cor. S'analitza la relació del segment RC amb la pressió arterial i l'interval cardíac. La concordança entre la duració dels batecs de l'ECG i de l'ICG és un dels resultats clau per a desenvolupar nous algoritmes de detecció d'artefactes i el segment RC també podria ser rellevant per a la descripció de l'hemodinàmica dels pacients.

Les distribucions de temps-freqüència (TFD, per les seues sigles en anglés) s'utilitzen per a caracteritzar com el contingut dels senyals de cardiografia d'impedància canvia amb el temps. Atès que les TFDs han de calcular-se emprant nuclis (*kernels,* en anglés) concrets, es presenta un nou mètode per a seleccionar el millor nucli mitjançant la utilització de senyals sintètiques. Les TFDs d'ICG optimitzades es calculen per extraure distintes característiques que són emprades per discriminar entre diferents estats d'anestèsia en pacients sotmesos a processos quirúrgics.

Les característiques derivades de les distribucions de temps-freqüència també són utilitzades per descriure les operacions quirúrgiques durant tota la seua extensió temporal. La relació entre eixes característiques són analitzades i es proposen distints models de predicció per a la despesa cardíaca. Aquests models de predicció demostren que les característiques derivades de les distribucions de temps-freqüència de senyals d'ICG estan relacionades amb la despesa cardíaca dels pacients.

Darrerament, es presenta un estudi de validació del monitor qCO. Aquest monitor ha sigut dissenyat utilitzant alguna de les tècniques que són conseqüència d'aquesta Tesi Doctoral. Les principals conclusions d'aquest treball han sigut protegides amb una patent que ja ha sigut registrada.

Així doncs, aquesta Tesi Doctoral ha produït una considerable quantitat de dades clíniques i una varietat de tècniques de processat i anàlisi de senyals de cardiografia d'impedància que han sigut integrades en dispositius biomèdics ja disponibles comercialment.

Codis UNESCO: 240602 (Bioelectricitat), 331110 (Instruments mèdics), 241103 (Fisiologia cardiovascular).

Resumen

El gasto cardíaco (GC) define el flujo de sangre que llega desde el corazón a los distintos órganos del cuerpo y es, por tanto, un determinante primario del transporte global de oxígeno. Se ha medido tradicionalmente usando métodos invasivos cuyos riesgos excedían en ocasiones las ventajas de su monitorización.

En este contexto, la minimización del riesgo de la monitorización del gasto cardíaco en nuevas tecnologías no invasivas podría traducirse en mayores ventajas para médicos, hospitales y pacientes: facilidad de uso, disponibilidad del equipamiento y menor tiempo de recuperación y mejores resultados en el paciente. La impedancio-cardiografía o cardiografía de impedancia (ICG) es una prometedora tecnología no invasiva para la monitorización del gasto cardíaco. Sin embargo, la información disponible sobre las señales de ICG es más escasa que otras señales fisiológicas como el electrocardiograma (ECG).

La presente Tesis Doctoral contribuye al desarrollo de técnicas de tratamiento de señal de ICG para así crear un monitor hemodinámico innovador.

En primer lugar, se proporciona una extensa revisión bibliográfica sobre los aspectos básicos del contexto clínico en el que se utiliza la monitorización del gasto cardíaco así como sobre el estado del arte de los monitores de gasto cardíaco que existen en el mercado. Esta Tesis Doctoral ha producido una considerable cantidad de datos clínicos que también se explican en detalle. Dichos datos clínicos también son útiles para complementar las explicaciones teóricas de los índices de paciente de variabilidad cardíaca y el flujo y la presión sanguíneos. Además, se presenta un nuevo método de creación de señales sintéticas biomédicas con características de tiempo-frecuencia conocidas.

Uno de los primeros análisis de esta Tesis Doctoral estudia la diferencia temporal entre los picos de los latidos cardíacos del ECG y del ICG: el segmento RC. Este segmento RC es una medida del retardo temporal entre la actividad eléctrica y mecánica del corazón. Se analiza la relación del segmento RC con la presión arterial y el intervalo cardíaco. La concordancia entre la duración de los latidos del ECG y del ICG es uno de los resultados claves para desarrollar nuevos algoritmos de detección de artefactos y el segmento RC también podría ser relevante en la descripción de la hemodinámica de los pacientes.

Las distribuciones de tiempo-frecuencia (TFD, por sus siglas en inglés) se utilizan para caracterizar cómo el contenido de las señales de impedancia cardiográfica cambia con el tiempo. Dado que las TFDs deben calcularse usando núcleos (*kernels*, en inglés) concretos, se presenta un nuevo método para seleccionar el mejor núcleo mediante el uso de señales sintéticas. Las TFDs de ICG optimizadas se calculan para extraer distintas características que son usadas para discriminar entre los diferentes estados de anestesia en pacientes sometidos a procesos quirúrgicos.

Las características derivadas de las distribuciones de tiempo-frecuencia también son utilizadas para describir las operaciones quirúrgicas durante toda su extensión temporal. La relación entre dichas características son analizadas y se proponen distintos modelos de predicción para el gasto cardíaco. Estos modelos de predicción demuestran que las características derivadas de las distribuciones tiempo-frecuencia de señales de ICG están relacionadas con el gasto cardíaco de los pacientes.

Finalmente, se presenta un estudio de validación del monitor qCO, diseñado con alguna de las técnicas que son consecuencia de esta Tesis Doctoral. Las principales conclusiones de este trabajo han sido protegidas con una patente que ya ha sido registrada.

Como conclusión, esta Tesis Doctoral ha producido una considerable cantidad de datos clínicos y una variedad de técnicas de procesado y análisis de señales de cardiografía de impedancia que han sido incluidas en dispositivos médicos ya disponibles comercialmente.

Códigos UNESCO: 240602 (Bioelectricidad), 331110 (Instrumentos médicos), 241103 (Fisiología cardiovascular).

Contents

This page is intentionally left blank.

List of Figures

List of Tables

Abbreviations

AIMDD	Active Implantable Medical Device Directive
ANFIS	Adaptive Neuro-Fuzzy Inference System
ANS	Autonomous Nervous System
AUC	Area Under the Curve
BJD	Born-Jordan Distribution
BMI	Body Mass Index
BP	Blood Pressure
BSA	Body Surface Area
CI	Cardiac Index
CO	Cardiac Output
CREB	Biomedical Engineering Research Centre
CWD	Choi-Williams Distribution
DBP	Diastolic Blood Pressure
ECG	Electrocardiogram
EDV	End Diastole Volume
EEG	Electroencephalogram
EMBD	Extended Modified Beta Distribution
EMG	Electromyogram
ESAII	Enginyeria de Sistemes, Automàtica i Informàtica Industrial
FN	False Negative
FP	False Positive
GDT	Goal-Directed Therapy
HF	High Frequency
HR	Heart Rate
HRV	Heart Rate Variability
ICG	Impedance Cardiography
IF	Instantaneous Frequency
IIR	Infinite Impulse Response
IQR	Inter-Quartile Range
ISO	International Organization for Standardization
LBM	Lean Body Mass

LF	Low Frequency
LOA	Limits of Agreement
LOC	Loss of Consciousness
MBD	Modified Beta Distribution
MBP	Mean Blood Pressure
MDD	Medical Device Directive
NN	Normal-to-normal ECG beats
MSE	Mean Square Error
NMBA	Neuromuscular Blocking Agents
NMR	Non-Depolarizing Muscular Relaxants
PAC	Pulmonary Artery Catheter
PCA	Pulse Contour Analysis
PEP	Pre-Ejection Period
PRD	Percentile Root Mean Square Difference
PWA	Pulse Wave Analysis
PWTT	Pulse Wave Transit Time
QMS	Quality Management System
RAP	Right Atrial Pressure
RP	Recurrence Plot
ROC	Receiver Operating Characteristic
SBP	Systolic Blood Pressure
SD	Standard Deviation
SM	S-Method
SNR	Signal-to-Noise Ratio
STFT	Short-Time Fourier Transform
SV	Stroke Volume
SVD	Singular-Value Decomposition
SVI	Stroke Volume Index
SVR	Systemic Vascular Resistance
SVV	Stroke Volume Variation
TFCM	Time-Frequency Complexity Measure
TFD	Time-Frequency Distribution
TFNRE	Time-Frequency Normalized Rényi Entropy
TFRE	Time-Frequency Rényi Entropy
TPR	Total Peripheral Resistance
VLF	Very Low Frequency
WVD	Wigner-Ville Distribution
ZAO	Zhao-Atlas-Marks Distribution

Chapter 1

Introduction

Abstract

This introductory chapter aims to give an initial overview of the topics addressed in the present Doctoral Thesis. The basic problem on which this research focuses is explained. Furthermore, the specific objectives to accomplish with this study are defined. Finally, the framework where this thesis was developed is provided as a guide for the reader.

1.1 Introduction

This chapter is divided into three main parts. The first part will state the problem this work concentrates on. Thanks to the analysis of the initial problem, concrete objectives are therefore established as a guideline for the Doctoral Thesis. The special framework in which the Doctoral Thesis has been developed is explained in detail. Finally, the outline of the present document is also provided at the end of this Chapter.

1.2 Problem Statement

Cardiac output (CO) is a primary determinant of global O_2 transport from the heart to the body. It defines the blood flow arriving to the different organs in the body. As a consequence, determination of CO is essential in any advanced hemodynamic monitoring system in perioperative and intensive care medicine.

Traditionally, CO has been measured using invasive methods such as the intracardiac catheterization. The risk involved in such invasive methods posed a burden on the standardization of this measurement since clinicians needed to evaluate the balance between the risk and the advantages of the CO measurement.

Today, there is a continuous search for methods of CO measurement which are less invasive than its predecessors in order to minimize risk. Such risk minimization in new noninvasive technologies for CO monitoring could translate into major advantages for clinicians, hospitals and patients: ease of usage and availability, reduced recovery time, and improved patient outcome.

New technologies are nowadays available for noninvasive CO monitoring but further research is required to improve the different options for noninvasive continuous CO with regard to signal acquisition, signal processing, and clinical applicability.

Impedance Cardiography (ICG) is a promising solution for noninvasive continuous CO monitoring. The technique to calculate the CO using the ICG was first proposed by Kubicek in 1966 but due to the state of the art, it did not further devolved [1]. The latest advances in biomedical signal processing allow us to further explore this technique, which is the main topic of this Doctoral Thesis. There exists a vast bibliography about electrocardiogram (ECG) but information on ICG is scarce. In this Doctoral Thesis, the impedance cardiography signal has been studied and characterized using time-

frequency distributions (TFDs) and Recurrence Plots (RPs). The relationship between TFD-derived and RP-derived features and the hemodynamic state of patients has been studied. Finally, some of the resulting algorithms have also been implemented and validated in the new noninvasive CO monitor qCO by Quantium Medical.

1.3 Objectives

The ideal CO monitor should be reliable, continuous, noninvasive, operator-independent and cost-effective and should have a fast response beat-to-beat time [2]. Impedance cardiography is a technique which can definitely fulfill all those requirements but the technology is still under development. Main issues arise when trying to find the exact parameters to extract from the ICG curve but, mostly, the most important problems are associated with high levels of noise and artifacts which appear due to the movement of the patient.

The main final contribution of this Doctoral Thesis is the **development of signal treatment techniques for the thoracic bioimpedance signals in order to create an innovative hemodynamic monitor**. The development of this Doctoral Thesis under the framework of the Industrial PhD program by the Catalan government has reinforced the availability of resources and the practical focus which all the developed signal treatment techniques must fulfill in order to be applicable to marketable real-time medical devices.

Specific objectives of the present Doctoral Thesis are:

- Research on the available technologies for CO measurement: there is a vast amount of literature regarding CO measurement, which has historically been an invasive technique. Today, a large number of methodologies have appeared promising to be noninvasive and this Doctoral Thesis provides a compilation of several research works as a background for innovation.

- Evaluation of the relation between CO and anesthesia: the qCO monitor is used to record the CO of patients undergoing anesthesia and statistical tests have been conducted in order to quantify the effect of anesthesia on CO and other hemodynamic indices.

- Time-frequency distributions of impedance signals: the complexity and variability of ICG signals in both frequency and time domains imposed the need to apply time-frequency analysis. Several time-frequency distributions have been applied to bioimpedance signals:

Wigner-Ville, Choi-Williams, Beta Distribution, etc. TFD-derived features applied to bioimpedance signals have been extracted with the best-performance TFD kernels.

- Relation between hemodynamic indices and TFD-derived features: several studies have been executed in order to investigate whether TFD-derived features of impedance signals relate to the hemodynamic state of the patient. The relation between hemodynamic indices and features derived from Recurrence Plots has also been investigated.

- Statistical comparison between the qCO monitor and other CO monitors: in order to check the performance of the algorithms developed in this Doctoral Thesis.

- Publication of a Patent: according to the contractual agreement between Universitat Politècnica de Catalunya and Quantium Medical, the advancements developed during this Doctoral Thesis must be protected. Thus, in order to ensure the rights of the company and to foster the society of knowledge, a patent has been submitted with the algorithms implemented in the commercial qCO monitor and will be owned by Quantium Medical, as agreed with the university. The patent will comprise all the processing techniques used to improve the calculation of hemodynamic indices.

1.4 Thesis Framework and Outline

Quantium Medical specializes in the design and development of noninvasive patient monitoring methods and applications in the field of anesthesia. Since 2016, Quantium Medical is a Fresenius Kabi company, a global healthcare company that specializes in medicines and technologies for infusion, transfusion and clinical nutrition. Quantium Medical reinforces Fresenius Kabi products by providing monitoring technology for infusion and transfusion technology. There has also been a long, fruitful collaboration between Quantium Medical and the Automatic Control Department (Enginyeria de Sistemes, Automàtica i Informàtica Industrial, ESAII) and Biomedical Engineering Research Centre (CREB), both belonging to the Universitat Politècnica de Catalunya.

ESAII and Quantium Medical have led this Doctoral Thesis within the framework of the Industrial PhD program of the regional Catalan Government (Generalitat de Catalunya, DI-2014). This program aims to

contribute to the competitiveness and internationalization of the Catalan industrial fabric, retain talent and place doctoral students where they can develop research and innovation projects.

The synergy of both entities under the patronage of the Catalan Government has provided a vast amount of resources for this Doctoral Thesis. On the one hand, Quantium Medical's knowledge on the biomedical market needs and former experience in anesthesia monitoring have ensured access to a large amount of proprietary databases, contacts and know-how. On the other hand, the experience of ESAII in biomedical signal processing has been a key to success for this project.

The main techniques developed within this Doctoral Thesis relate to template searching, time-frequency characterization for ICG signals, and statistical methods for the calculation of CO using the ICG signals. Several of these techniques have been implemented and validated onto a new device which measures CO in a noninvasive, continuous way.

1.5 Outline

After the introduction to the problems analyzed and the main objectives of this Doctoral Thesis, Chapter 2 explains all necessary aspects regarding the medical and technical background. An introduction to Impedance Cardiography and Electrocardiography is also included in the first part of the second chapter. It then includes details of the state of the art regarding medical devices for CO monitoring. Nowadays, there are several technologies in the market which differ in the degree of invasiveness. Nevertheless, more invasive technologies imply a higher risk which is not always worth to take and therefore, noninvasive technologies are being developed. Impedance Cardiography is a promising technology which can combine the characteristics required by clinicians for noninvasive CO monitors. Methods of validation of CO monitor are also included at the end of this chapter.

Chapter 3 introduces the databases which have been developed during this Doctoral Thesis. The synergies between the private company and the public university supervising this Doctoral Thesis have produced numerous opportunities for data collection. Finally, this chapter also explains a new procedure to create synthetic biomedical signals with known time-frequency characteristics. These synthetic database will also be used in subsequent chapters.

Chapter 4 describes the relationship between heart rate variability, blood flow and blood pressure during anesthesia. Anesthesia procedures are one of the situations where CO monitors are most useful. Anesthetic drugs exert an influence on heart rate variability, blood flow and blood pressure which are analyzed in this chapter in order to complement, from a statistical point of view, the explanations offered in chapter 2 regarding the medical background.

Chapter 5 introduces the RC segment as the time difference between characteristic points in the electrocardiogram and the impedance cardiogram. This RC segment is a measure of the time delay between the electrical and mechanical activity of the heart. The RC segment is statistically described in different situations and its relationship with blood pressure and heart interval is analyzed. The concordance of beat durations of both the electrocardiogram and the impedance cardiogram is key to develop new artefact detection algorithms and the RC could also have an impact in describing the state of a patient.

Chapter 6 explains time-frequency distributions as a methodology to analyze how the frequency content in impedance cardiography signals change with time. Since time-frequency distributions are calculated using concrete kernels, this chapter focuses on selecting the best kernel by using the synthetic signals created in Chapter 3.

Chapter 7 explores different features derived from the time-frequency distributions analyzed in the previous chapter. These features are used to discriminate between awakeness and anesthesia states in patients undergoing surgery.

Chapter 8 extends the work in the previous chapter by analyzing the behavior of features derived from the time-frequency distributions during the whole process of surgical operations. In addition, features from Recurrent Plots – a methodology to analyze periodicities in non-stationary signals – are also included in the analysis. Relationships between all the presented features with hemodynamic parameters and depth of anesthesia are studied. Prediction models for CO trained with the before-mentioned features are also created.

Chapter 9 presents a validation of the CO monitor which has been developed during this Doctoral Thesis. The qCO monitor is compared with the LiDCOrapid monitor and results on agreement between both methods are explained. Finally, the main conclusions of this Doctoral Thesis are presented. In addition, guidelines for further work are proposed.

Chapter 2

Medical and Technical Background

Abstract

This chapter introduces the clinical and technical background for the understanding of this Doctoral Thesis. It starts with the physiological aspects which justify the analysis of the electrocardiogram (ECG) and impedance cardiogram (ICG) signal, which are also explained in detail. Important information is also provided regarding blood flow management, monitoring during anesthesia, and the variety of cardiac output monitoring technologies. Finally, the main validation techniques for cardiac output monitoring are explained.

2.1 Introduction

The first part of the present chapter deals with general concepts on physiology and hemodynamics: the heart, the circulatory system and its nervous connections regulating both blood pressure and blood flow. ECG and ICG signals are also detailed. Anesthesia settings are explained with a special focus on how important flow monitoring is for patient safety.

The second major part of this chapter explains the available medical device technology. Finally, the design and validation of new medical devices is described.

2.2 Hemodynamics

Hemodynamics is the study of the blood pumped by the heart across the circulatory system. The main components which we need to analyze to understand hemodynamics are the heart, as the central part of the circulatory system, and the nervous innervation. All these components interact to change blood pressure and blood flow, which are central topics in anesthesia management.

2.2.1 The Heart and the Circulatory System

The heart is a biological pump which supplies the blood flow through the blood vessels of the circulatory system. It does so by adjusting the required pressure and amount of blood [3].

This muscular organ is composed of four chambers (**Figure 2.1**), two superior or atria and two inferior or ventricles. Blood enters the right atrium and passes through the right ventricle, which pumps the blood to the lungs for oxygenation. The oxygenated blood returns to the heart via the pulmonary veins which enter the left atrium. From there, blood flows to the left ventricle. The latter is in charge of pumping the blood into the aorta which distributes the oxygenated blood through the circulatory system. This pathway is described in **Figure 2.1**.

The circulatory or cardiovascular system collects the blood pumped by the aorta and permits its circulation in order to transport nutrients, oxygen, carbon dioxide, etc. Adequate blood circulation is a necessary condition for adequate supply of oxygen to all tissues.

Hemodynamics is concerned with the mechanical and physiological properties which control blood pressure and blood flow through the body.

Hemodynamic monitoring is the observation of hemodynamic parameters over time, such as blood pressure, heart rate or CO.

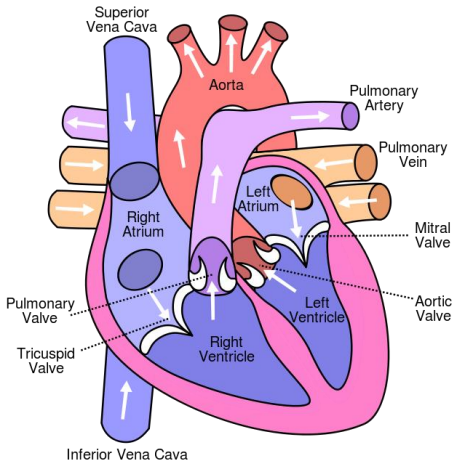

Figure 2.1 Diagram of the human heart showing the four cardiac chambers, valves, arteries and veins (Creative Commons)

2.2.2 Vagal and Sympathetic Innervation

The autonomic nervous system is the primary neural mediator of physiological responses to internal and external stimuli. It is composed of 2 branches: the sympathetic nervous system, which ultimately innervates blood vessels and the heart, and the parasympathetic (vagal) nervous system, which also innervates the heart [4].

Sympathetic stimulation of the heart increases the rate of sinoatrial node diastolic depolarization, heart rate, atrioventricular conduction velocity (positive dromotropy), and heart contractility in the atrial and ventricular muscles (increasing the capability of the heart to pump larger volumes of blood). Parasympathetic stimulation of the heart has some opposite effects: it decreases the rate of diastolic depolarization, heart rate, and the atrioventricular conduction velocity. Sympathetic and parasympathetic effects on heart function are mediated by beta-adrenoceptors and muscarinic receptors, respectively. One of the most important functions of nervous control of the circulation is its capability to cause rapid increases in arterial pressure and heart rate, beginning and accomplishing the circulatory adaptation within seconds [4].

2.2.3 Blood Flow

Cardiac output is defined as the volume of blood ejected from the heart every minute [5]. At rest the normal adult CO is approximately 5–6 L/min and the normal cardiac index (CI) is 2.6–3.2 L/min/m^2. CO is the product of stroke volume (SV) and heart rate (HR). Stroke volume is the volume of blood pumped from the left ventricle of the heart per beat and is determined by the volume of blood in the ventricles at the end of the diastole (end diastole volume or EDV), the impedance to blood flow in arteries (total peripheral resistance or TPR) and the strength of ventricular contraction or contractility. The typical value of stroke volume is 70 mL and its normal range varies from 55 to 100 mL. The three major determinants of stroke volume, and thus CO, are preload, afterload, and contractility. Preload and contractility are directly correlated to stroke volume while afterload is inversely correlated.

$$\mathrm{CO} = \mathrm{SV} \cdot \mathrm{HR}\ (\mathrm{L/min}) \tag{1}$$

Cardiac index (CI) is a parameter which relates the CO from the left ventricle to the body surface area (BSA) and it is calculated using (2). The unit of measurement is liters per minute per square meter and the BSA is the measured or calculated surface area of a human body. It can be approximated by several methods and the most widely used is the Du Bois formula reported in Equation (3).

$$\mathrm{CI} = \frac{\mathrm{CO}}{\mathrm{BSA}}\ (\mathrm{L/min/m^2}) \tag{2}$$

$$\mathrm{BSA} = 0.007184 \cdot \mathrm{W}^{0.425} \cdot \mathrm{H}^{0.725}(\mathrm{m^2}) \tag{3}$$

where W(kg) and H(cm) are the patient's weight and height, respectively.

Similar to the cardiac index, the stroke volume index (SVI) relates the stroke volume to the size of the person body surface area (BSA):

$$\mathrm{SVI} = \frac{\mathrm{SV}}{\mathrm{BSA}} = \frac{(\mathrm{CO/HR})}{\mathrm{BSA}} = \frac{\mathrm{CO}}{\mathrm{HR} \cdot \mathrm{BSA}}\ (\mathrm{mL/beat/m^2}) \tag{4}$$

Stroke volume variation (SVV) is a natural phenomenon in which the stroke volume falls during inspiration and increases during expiration because of the changes in intra-thoracic pressure during ventilation. SVV represents

the variation (as a percentage) of SV during the ventilation cycle and is traditionally calculated according to Equation (5).

$$\mathrm{SVV}(\%) = 100 \cdot \frac{\mathrm{SV_{max}} - \mathrm{SV_{min}}}{\mathrm{SV_{mean}}} \tag{5}$$

Currently, there is no consensus on the use of SVV in patients with spontaneous ventilation. However, literature supports its usage when patients are mechanically ventilated. Normal SVV values are less than 10-15% [6].

2.3 ECG Signals

The electrocardiogram (ECG) is one of the most widely used biomedical signals in medical practice since it is a noninvasive measure and can be easily acquired. As **Figure 2.2**, the ECG signal is composed by several waves: a P wave, a QRS complex (formed by three waves Q, R, and S), a T wave, and occasionally a U wave. The QRS complex is the reference point for ECG applications because it is the most prominent wave in the cardiac cycle.

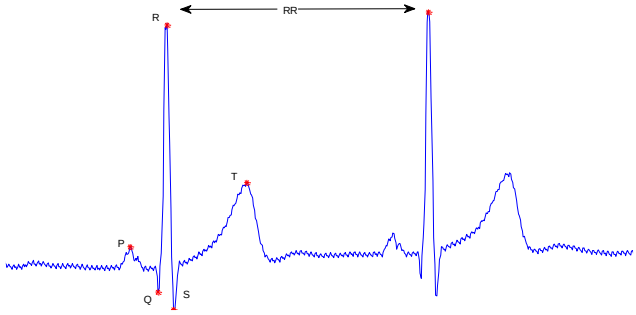

Figure 2.2 A pair of cardiac beats with the P and T waves and the QRS complex. The RR segment is the distance between two consecutive R peaks

The ECG signal may be affected by several sources of noise and interferences, which can significantly alter the morphology of the signal, producing errors in the measurement systems. The most common noise or interferences are: (a). baseline wandering due to for example respiration signal or movements of patient; (b). electromyographic (EMG) noise; (c). 50/60 Hz power line interference; (d). electrosurgical instruments interferences [7].

From the QRS detection standpoint, noise might also have physiological origins, i.e., tall P or T waves, ectopic beats, etc. These noises or interferences cause extreme values in the inter-beat interval time series which are seen in form of false positive (FP, non-existent QRS complex is detected as true) or false negative (FN, detection of an existing QRS complex is omitted).

However, a normal-to-normal (NN) time series, i.e., a clear R-R time series (free of artifacts or ectopic beats), is crucial for a proper heart rate variability analysis [8] which is an important part of the qCO monitor.

Furthermore, the detection of characteristic points in the impedance cardiogram might also depend on the position of the R peak in the ECG. Thus, any algorithm implemented for the QRS complex identification has to be able to reject or to at least attenuate the adverse effects of such noise sources.

2.4 ICG Signals

Impedance cardiography is the study of cardiac function determined from measurements of the electrical impedance of the thorax [9]. Typically, the impedance is measured at around 50 kHz using currents of around 1 mA rms, which ensures no physiological effects. Four electrodes are situated on the patient: two on the neck and two on the lower end of the thorax. The outer electrodes supply the current and the inner electrodes are used for voltage pick-up.

As shown in **Figure 2.3**, during systole, the impedance Z decreases which fosters the assumption that the blood volume in the region measured has increased. On the ICG waveform, the letters represent labels to indicate cardiac activity: A. atrial activity, B. synchronous wave with first heart sound, C. largest decrease in impedance during systole, X. aortic wave closure, Y. pulmonary valve closure and O. largest decrease in impedance during diastole. The CC segment is the heart period in the ICG.

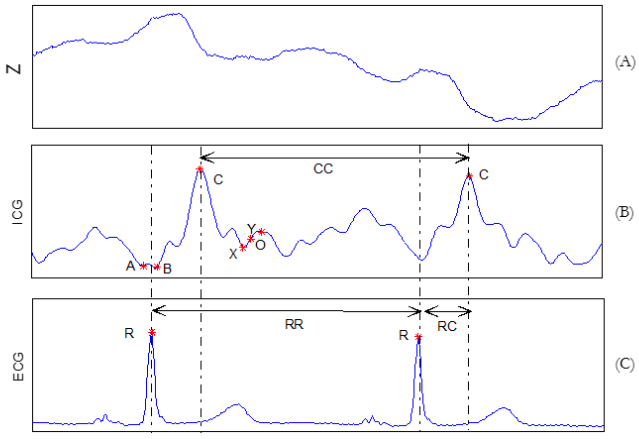

Figure 2.3 Typical impedance waveforms from the thorax of a human subject: (A) impedance wave Z; (B) ICG signal with all characteristic points; (C) ECG signal with R peaks, RR heart period and RC segment (distance between R peaks in the ECG and C peaks in the ICG)

In **Figure 2.3**, the ECG is also included to show the RR segment, the heart period in the ECG, and the RC segment which is the difference between the C peak in the ICG and the R peak in the ECG. The RC segment will be further explained in Chapter 5.

2.5 Anesthesia in the Operating Room

2.5.1 Introduction

Anesthesia aims at three objectives: hypnosis, analgesia, and muscle relaxation. This is achieved by the use of intravenous or inhalational anesthetics. The most common hypnotic, inhaled drugs are nitrous oxide, sevoflurane and desflurane while barbiturates, benzodiazepines, ketamine, and propofol are some of the main intravenous anesthetic drugs [10].

Analgesia refers to the avoidance of pain in the patient. Some of the most common analgesics are fentanyl, remifentanil and alfentanil. These drugs cancel the sensation of pain, resulting in a sedation state and a respiratory depression. As a consequence of decreased alveolar ventilation, the pressure of CO_2 in blood increases, whereas arterial pH and the pressure of O_2 in blood decreases. The degree of depression not only depends on the dose but also on the route of administration and speed of access to the central nervous system [10].

During anesthesia, remifentanil is known to cause hypotension and bradycardia either by parasympathetic activation or by other negative chronotropic effects [11]–[14]. Remifentanil also decreases sympathetic action [15]. Propofol during anesthesia reduces parasympathetic tone to a lesser degree than sympathetic tone [16]–[24]. The combination of remifentanil and propofol could therefore imply a maintained or slightly reduced vagal tone and a reduced sympathetic tone.

Neuromuscular blocking agents (NMBA) are used to facilitate operations which require muscular tissues to be relaxed such as endotracheal intubation. NMBAs can be depolarizing and non-depolarizing. Non-depolarizing muscular relaxants (NMR) such as pancuronium, vecuronium, coruronium, atracurium, cisatracurium and mivacurium prevent the depolarization from happening so that the muscle action potentials are not propagated [10].

Not a single drug produces all the effects required during a surgery. Therefore, combinations of different drugs are used. Over-dosages or under-

dosages are to be avoided during anesthesia procedures and therefore different methods are used to monitor the degree of anesthesia and analgesia. Several technologies have been developed during the last years.

In this Doctoral Thesis, the Conox® monitor (Quantium Medical, Barcelona) has been used during the registration of several databases to investigate the relationship between ICG characteristics and the patient's depth of anesthesia. The Conox monitor includes a depth-of-anesthesia index, qCON, which ranges from 0 to 99. This index can be divided into four different patient states: awakeness (qCON > 80), sedation (qCON ∈ [60, 80]), general anesthesia (qCON ∈ [40, 60]) and deep anesthesia (qCON < 40).

2.5.2 Importance of Flow Monitoring in the Operating Room

Oxygen is constantly required to maintain aerobic metabolism in human tissues. Low cardiac output and/or inadequate oxygen transportation in the blood can impair this oxygen supply. When this impairment is severe, the body tissues slowly revert to anaerobic metabolism, producing toxic metabolic breakdown products, such as lactic acid. Therefore, maintenance of cardiac output above the minimum threshold for aerobic metabolism is necessary for the health and survival of body tissues [25].

Critical illness or major surgery are two situations when a systemic inflammatory response syndrome might occur. This syndrome causes an increased demand of oxygen which results in compensation mechanism to meet such demand. Failure to increase cardiac output can lead to tissue hypoxia and an eventual organ dysfunction. Therefore, monitoring of cardiac output is vital in these situations. In fact, researchers have reported that low cardiac output in critically ill patients may be related to increased morbidity and mortality [25].

In patients with insufficient tissue perfusion, fluid resuscitation is often the first option. Nevertheless, only 50% of hemodynamically unstable patients have been reported to be volume responsive [26]. Volume responsiveness is the situation when an increase in patients' fluids corresponds to an increase in stroke volume. Fluid resuscitation aims to increase the stroke volume and therefore in unresponsive patients this therapy is not beneficial at all. Therefore, fluid challenges also require monitoring blood flow.

2.5.3 Fluid Management

During an operation, the classical approach to fluid management used to be based on the prediction of the amount of fluids needed during the surgery based on the duration and severity of the particular operation. Fluids were therefore empirically replaced based on these calculations.

Nowadays, fluid management is based on the concept of goal-directed therapy (GDT). Fluid management strategies based on stroke volume optimization are extremely well-validated approaches that have shown to reduce patient morbidity [27]–[30].

During surgery, hypovolemia (decreased blood volume) and hypervolemia (excessive body fluid) represent a severe risk for patients and either situation is related to higher perioperative morbidity risk [31]. Hypovolemic situations are related to tissue hypoxia, organ failure, tachycardia, hypotension, renal failure, etc. Hypervolemic situations are related to volume overload, poor oxygenation, organ failure, peripheral edema, respiratory failure, poor wound healing, etc. In **Figure 2.4**, discontinuous line B represents a division between patients who are hypovolemic and hipervolemic. Discontinuous line C represents the limits over which the risk associated to the hypovolemic and the hypervolemic situations increases dramatically.

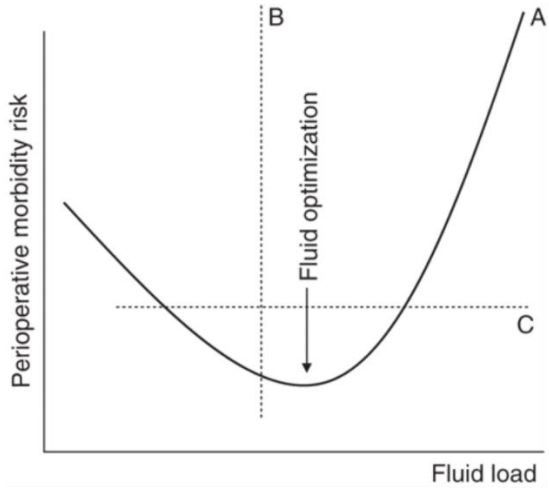

Figure 2.4 Lines of risk in fluid management during surgery [31]: discontinuous line B separates hypovolemic and hypervolemic patients and discontinuous line C represents the limit of excessive patient risk. Patients should be loaded with fluids so that the morbidity risk is minimized

In fluid management strategies, the ideal approach should be able to define the nadir of the curve in **Figure 2.4** in a tight manner [31] in order to maintain the patient in such state. However, this requires individualized measurements since the volume required to achieve this may vary dramatically between patients even in the same standard of care [32]. However, this nadir point can be analyzed by the Frank-Starling law. This law represents the relationship of the stroke volume and the end diastolic volume or the venous return and the right atrial pressure (RAP).

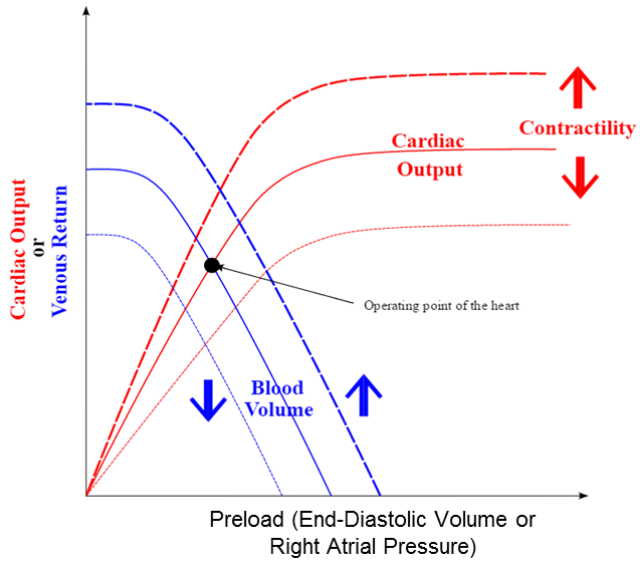

Figure 2.5 Frank-Starling law of the heart. As preload increases, cardiac output increases and venous return decreases and there is an operating point which makes cardiac output equal venous return

The red curves in **Figure 2.5** represent the relationship between the CO and the end-diastolic volume (EDV) and the different curves depend on the contractility of the heart. If contractility of the heart, i.e., the strength of the myocardial fibers of the heart, increases, the amount of blood which is pumped out by the heart increases. The blue curves in the figure represent the relationship of the RAP as a consequence of the venous return. Both venous return and RAP increase as the blood volume increases [33]. The optimal point is therefore the point in which the venous return (i.e., the input into the heart) equals the CO (i.e., the output of the heart). The optimal point can be achieved when fluid is infused in a patient until CO stops growing in a linear fashion.

2.6 Medical Devices Technology for Cardiac Output Monitoring

Over the last years, there has been a great variety of reviews and papers on the available methods to measure CO [2], [25], [26], [34], [35]. Generally, the most ideal CO monitor should be reliable, continuous, noninvasive, operator-independent and cost-effective and should have a fast-response time [2]. This subsection includes a review of the main techniques available, which are classified as invasive, minimally invasive and noninvasive.

2.6.1 Invasive Monitoring

In the late 19th century, Adolph Fick described how the changes in the concentration of a substance dissolved in blood could be used as an indicator for determining the blood flow. This concept was known as the Fick principle but never reached the clinical practice.

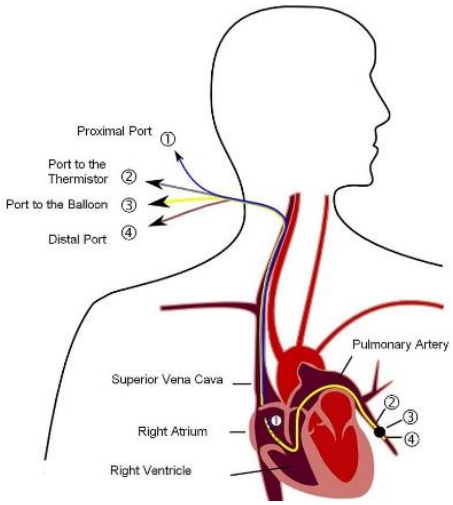

Figure 2.6 Swan-Ganz catheter for cardiac output measurements

Today, the pulmonary artery catheter (PAC) or Swan-Ganz catheter using the thermodilution technique is still considered to be the gold standard. As **Figure 2.6** shows, the catheter is introduced through a large vein, threaded though the right atrium of the heart, the right ventricle, and the pulmonary artery. An inflatable balloon at the tip inflates and can provide an indirect measurement of the pressure in the left atrium of the heart. A small thermistor behind the tip detects the passage of a cooler fluid and can then calculate the CO in the heart thanks to a thermodilution curve.

Despite being the gold standard, the use of this method is only recommended in patients in extreme situations with whom the benefits of a higher accuracy compensate for the higher risks. Abundant complications of PACs have been reported: damage to carotid and subclavian artery, pneumothorax, dysrhythmias, perforation of heart chambers, tamponade, valve damage, etc. Furthermore, issues arising with its usage and related to

operator, indicator and patient pathologies have to be emphasized [36]. Its use in low-risk cardiac surgery, vascular surgery and major abdominal, orthopedic or neurosurgical procedures is therefore not justified and minimally invasive or noninvasive alternatives are recommended.

2.6.2 Minimally Invasive Monitoring

There are several systems to measure CO which are considered semi-invasive or even minimally invasive. Transesophageal aortic Doppler ultrasound in the descending aorta can also be performed [37]–[40]. Special Doppler probes have been developed [ODMII (Abbott, Maidenhead, UK); CardioQ/Medicina TECO (Deltex Medical Ltd, Chichester, UK); HemoSonic100 (Arrow, Reading, Pennsylvania, USA)] although its clinical practice is very limited. In these devices, CO is calculated with the velocity time integral derived from the Doppler signal and the aortic cross-sectional area, which is estimated.

Other monitoring devices are based on the concept of pulse contour analysis or pulse wave analysis (PWA or PCA). This is based on the relation between blood pressure, stroke volume, arterial compliance and systemic vascular resistance (SVR). Flow indices can be calculated from the arterial pressure waveform if the arterial compliance and the SVR are known and different monitors use different approaches to obtain these variables in a minimally invasive way.

The PiCCO (Pulsion Medical Systems, Munich, Germany) combines pulse contour analysis with the transpulmonary thermodilution via femoral access [41]–[45]. It calculates the area under the systolic portion of the arterial waveform and it requires both central venous and central arterial catheterization. The calibration provided by the thermodilution remains accurate for six hours. It offers a broad range of hemodynamic parameters (including SVV) and is robust during hemodynamic instability.

The LiDCO system (LiDCO Ltd, London, UK) combines pulse contour analysis with lithium indicator dilution for continuous SV and SVV monitoring [38], [46]–[50]. This indicator is used to calibrate the measurement: lithium is injected into a peripheral vein and does not have an effect from a pharmacological point of view. It requires recalibration after acute hemodynamic changes. It obtains multiple cardiac parameters (such as SVV and SVR) by calculation of the root-mean-square value of the arterial pressure signal.

The FloTrac sensor combined with the Vigileo monitor (Edwards Lifesciences, Irvine, California, USA) also uses pulse contour analysis but requires no calibration. Instead, it needs some patient demographic and physical characteristics and a peripheral arterial catheter only to execute an automated, internal calibration. It is based on the calculation of a standard deviation of 2,000 arterial waveform points. Its main advantage is that it is minimally invasive, operator independent and easy to use. Its weak points are that it is inaccurate especially in vasoplegic patients and does not accurately track changes in SV [40], [50]–[54].

2.6.3 Noninvasive Monitoring

The ClearSight system (Edwards Lifesciences, Irvine, California, USA) provides noninvasive continuous blood pressure and CO through the method of the volume clamp. It involves clamping the finger artery with a cuff to a constant volume by dynamically providing equal pressure on either side of the arterial wall [42], [43], [55], [56]. This volume is measured by a photoplethysmograph built into the cuff. The ClearSight system inherits from the former Nexfin system (BMEye, Amsterdam, The Netherlands). The CNAP system (CNSystems Medizintechnik AG, Graz, Austria) also provides noninvasive continuous arterial pressure measurements by using the volume clamp method [57], [58].

The MostCare system (Vytech Health, Padova, Italy) uses pulse contour analysis and it calculates the area under the curve of the arterial waveform with no external calibration or pre-estimated data. It uses high time resolution (1,000 Hz) and it analyzes the entire cardiac cycle [59].

Pulse wave transit time (PWTT) is defined as the time between the R-wave in the ECG and the pulse wave rise-point assessed by pulse oximetry [60], [61]. The esCCO technology (Nihon Kohden) uses this technology by analyzing the ECG, the pulse oximeter waveform and the arterial pressure and it is based on an inverse correlation between the PWTT and the SV.

The partial CO_2 rebreathing technique evaluates respiratory CO_2 and applies the Fick principle to calculate CO [37], [62], [63]. Pulmonary blood flow can be calculated by relating the content of alveolar gas in pulmonary capillary blood to the quantity of gas passing to the lung.

The transthoracic Doppler (USCOM, Sidney, Australia) determines CO via flow measurements at the aortic or pulmonary valve but it requires a considerable level of experience for its usage and is not suitable for thoracic surgery [40], [63].

Electrical Bioimpedance

Electrical bioimpedance is a promising method which relies on the fact that the impedance of the thorax is dependent on the amount of fluid in the thoracic compartment. Standard bioimpedance systems apply a high-frequency electric current of known amplitude and frequency across the thorax and measure changes in voltage. The ratio between voltage and current amplitudes is a measure of transthoracic direct current resistance and varies in proportion to the amount of fluid in the thorax. CO is then computed based on mathematical equations under the assumption that thoracic impedance changes over time are proportional to the stroke volume.

Drawbacks of this technique include motion artifact, arrhythmias, pulmonary edema, and pleural effusions among others [64]. However, the totally noninvasive character of this technology exceeds these limitations.

There have been other attempts to use this technology in the past. Drazner and his colleagues studied patients with cardiomyopathy and found modest agreement between bioimpedance and thermodilution cardiac output monitoring [65]. Moreover, in Spiess' work general agreement was found in cardiac output from bioimpedance and pulmonary artery thermodilution [66]. In 2009 Simon and his colleagues reported a device named ICG Monitor 862146 (Phillips Medical System) which showed a significant statistical relation with the PAC. Unfortunately, the error percentage was 49% and this monitor ceased to exist some years ago [67]. SonoSite also discontinued its ICG monitor named BioZ in 2013 due to a business decision.

Electrical velocimetry [68] is a novel algorithm of electrical impedance cardiography used by the AESCULON monitor (Osypka Medical, Berlin, Germany). This algorithm includes the maximum rate of change of impedance of peak aortic blood acceleration.

Thoracic bioreactance [69] is another evolution of the electrical bioimpedance method which seeks to improve the signal-to-noise ratio using the bioreactance, which represents the phase shift in voltage across the thorax. The only commercially available system at present (NICOM, Cheetah Medical, Portland, Oregon, USA) uses 4 electrode patches each consisting of 2

electrodes and calculates cardiac output separately for the right and left side of the body with the final cardiac output being the average of these two values.

The qCO monitor (Quantium Medical)

A large quantity of studies evaluating and comparing different cardiac output monitors have been published [2], [25], [26], [34], [35], [39], [61], [63], [64], [67], [68], [70]–[79]. The new qCO monitor, by Quantium Medical, seeks to learn from past experiences and introduce new, advanced processing techniques to improve the cardiac output calculations. The new signal processing techniques in artifact removal and in time-frequency characterization are some interesting options to obtain a cardiac output monitor which improves the fulfillment of current market requirements compared to previous experiences.

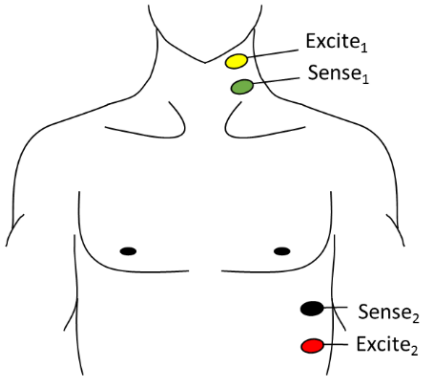

Figure 2.7 Location of the qCO electrodes. There are two exciting and two sensing electrodes positioned on the neck and on the side of the body under the ribs

The qCO monitor records the ICG and ECG signals by using 4 electrodes, with one pair injecting a constant current (at 50 kHz), and a second pair of electrodes measuring the resulting voltage (**Figure 2.7**). The voltage is amplified and digitized with a sampling frequency of 1,000 Hz. The qCO monitor uses the information from the impedance curve to calculate different hemodynamic indices.

2.7 Validation Techniques for Hemodynamic and Anesthesia Monitors

During the last years, the number of available monitors which claim to analyze the patient's hemodynamic situation in a noninvasive manner has considerably increased. Therefore, it is of outmost importance to select a range of techniques which permits comparing the different technological options which either have been launched into the market or are currently being developed.

2.7.1 Time Plot and Regression Plots

Some authors use simple time plots in which the results from both methods are plotted against time (either in seconds or samples). These methods permit to compare visually whether the indices calculated by two or more methods diverge.

Regression plots compare the values of one method versus the values of the other method. This plot usually includes a regression analysis with the Pearson's correlation coefficient. In the example in **Figure 2.8**, in plot (A) both methods have similar results and thus data points lie along the line of identity. However, in plot (B) there is a discrepancy causing the regression line not to coincide with the line of identity, which is not detected by Pearson's correlation coefficient.

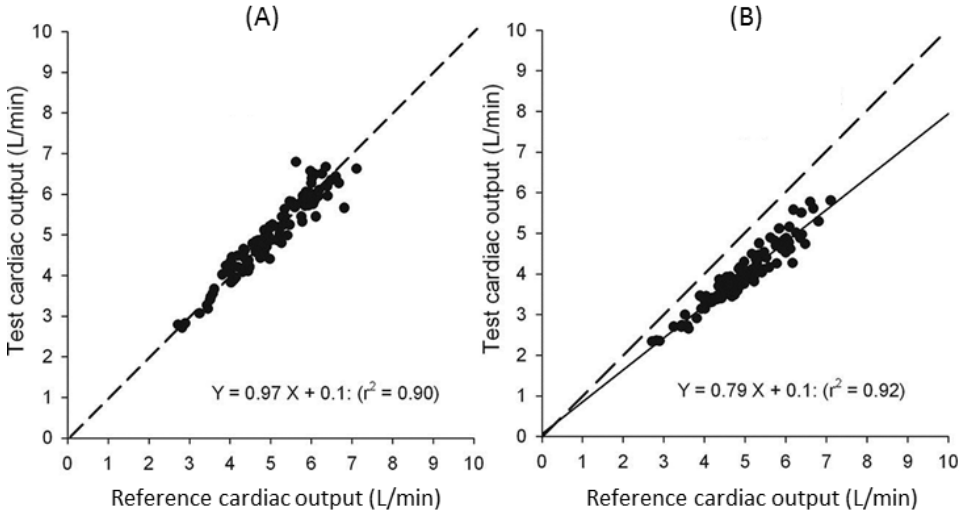

Figure 2.8 Regression plots for CO trending: cardiac output (CO) data demonstrate trending ability by lying along the line of regression, which lies along the line of identity (A) or with an offset (B)[80]

2.7.2 Bland-Altman Plots

The most popular method to evaluate cardiac output monitors is the Bland and Altman method [81]. This method analyzes the agreement between two different assays by plotting the mean of the two measurements as the abscissa value against the difference of the measurements as the ordinate value. Let S_1 and S_2 be the measurement given by two different methods, the Cartesian coordinates of a given sample S is:

$$S(x,y) = \left(\frac{S_1 + S_2}{2}, (S_1 - S_2)\right) \quad (6)$$

The 95% limits of agreement for each comparison are usually computed as the average difference ± 1.96 standard deviation of the difference. This explains how distant measurements by the two methods are more likely to be for most individuals. If the differences within mean ± 1.96 standard deviation (SD) are not clinically significant, the two methods may be used interchangeably.

Nevertheless, the Bland and Altman method only describes the coincidence of the evaluated method with the reference method but does not show whether the new method reliably detects changes in cardiac output or trending. Monitors can still be useful if they are capable of showing trends despite not providing a reliable measure of the absolute value of the cardiac output.

Critchley and Critchley [79] stated that when bias and precision statistics were used, mean cardiac output, bias, limits of agreement, and percentage error should be presented. Using current reference methods, acceptance of a new technique should rely on limits of agreement of up to ±30%.

Adjustment for Pooled Data

Bland and Altman plots consider that data points are statistically independent which is not true when repeated measures are taken from the same patient. This coupling of data results in smaller standard deviations and produces limits of agreement that underestimate the true variability of the readings. Both Bland and Altman [82] and Myles and Cui [83] have published articles that provide guidance on how to correct the analysis and limits of the agreement in the repeated-measures model.

2.7.3 The Four-Quadrant Plots

The four-quadrant plot was proposed by Perrino and his colleagues in 1994 [84]. It was presented as an analytical method based on regression analysis and concordance to compare a test device and a reference device. The figure plots the difference of the test cardiac output ΔCO_{test} against the difference of the reference cardiac output ΔCO_{Ref}. The pairs of values in the

center of the plot should be scattered around the four quadrants, which bring no statistical significance and thus are excluded in many studies. However, the pairs of data ($\Delta CO_{test}, \Delta CO_{Ref}$) outside the exclusion zone tend to fall into only one of the quadrants on the line of identity. Concordance in these plots is expressed as the percentage of data points falling in only one of the quadrants. **Figure 2.9** shows an example of the four-quadrant plot.

These four-quadrant plots offer more information on trending than other methods presented before. Exclusion zones are usually taken as 0.5 L/min, 1 L/min or < 10-15% of percentage change. Concordance rates should be > 90% to indicate reliable trending ability. Nevertheless, it should not be forgotten that the four-quadrant plot obliterates information about the magnitude of the underlying CO change and the absolute difference between measures.

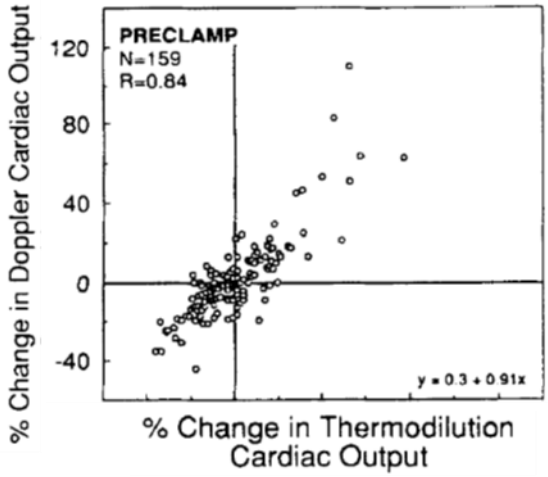

Figure 2.9 Four-Quadrant Scattergram which illustrates the trending capability of the Transesophageal Doppler [84]

2.7.4 The Polar Plot

To overcome the deficiencies of the four-quadrant plot, Critchley and his colleagues [80] suggest to convert the pairs ($\Delta CO_{test}, \Delta CO_{Ref}$) to polar coordinates, where agreement is shown by the angle the vector makes with the line of identity and the magnitude of change by length of the vector. In **Figure 2.10**, reproduced from the same work, polar plots perfectly show trending ability. For instance, polar plot (A) shows how most of the points lie within the 0.5 L/min as a sign of good trending ability, while in polar plot (C) many points lie outside the limits of agreement of 0.5 L/min.

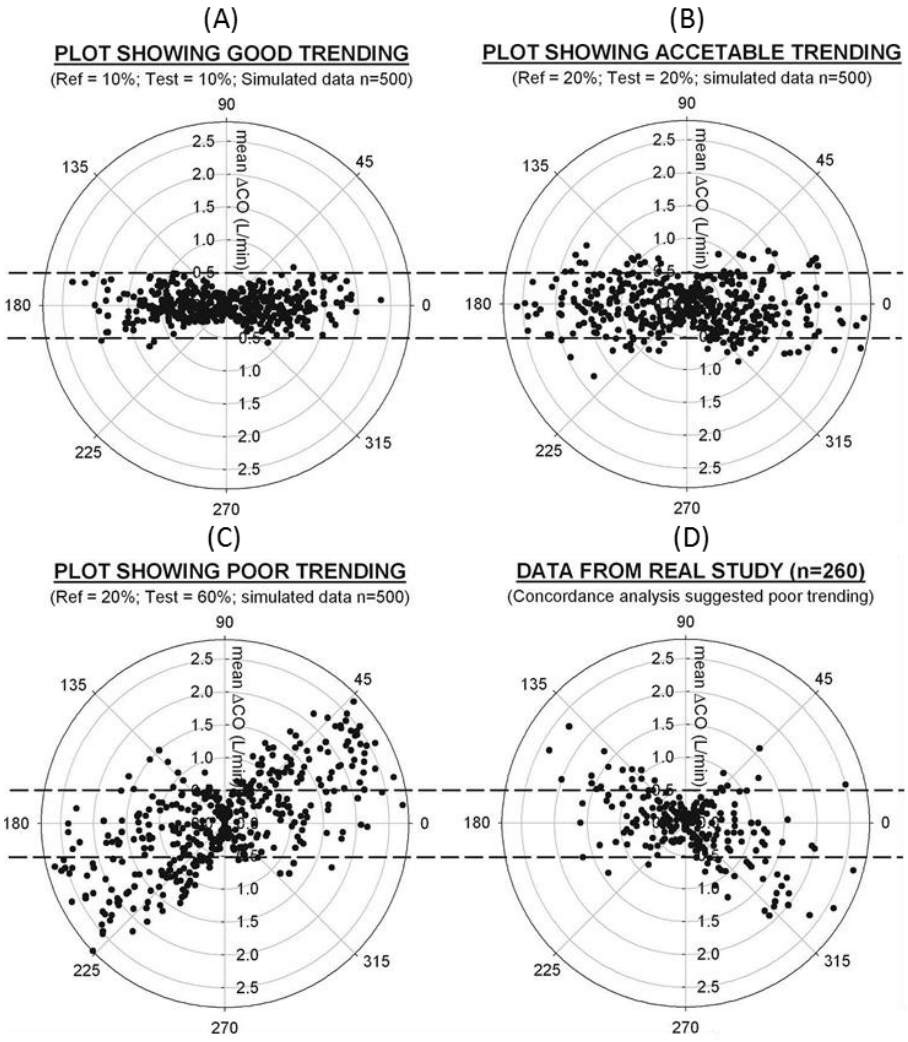

Figure 2.10 Polar plots used to show trending ability. The distance from the center of the plot represents the mean change in cardiac output (ΔCO) and the angle with the horizontal axis represents agreement. Data with good trending in (A) and (B) will lie within 0.5 L/min, or 10%, limits of agreement, compared to (C) and (D) [80]

2.7.5 Prediction Probability P_k

The prediction probability P_k is a performance measure recommended especially when comparing depth-of-anesthesia indicators with a gold standard. In such cases, Smith and his colleagues [85] propose to use the

prediction probability P_k and several authors have employed this performance measure [52]–[56].

This statistical measure is able to show the prediction probability with no dependence on scale units and it does not require knowing underlying distributions, linearizing or transforming scales. The P_k value must be between 0 and 1 and these extreme values are interpreted as an exact prediction, negative or positive, respectively. Meanwhile, a result of 0.5 implies a random chance of being correct.

Chapter 3

Databases

Abstract

This chapter contains the description of the databases used throughout the entire Doctoral Thesis. The databases have been recorded in a large variety of locations in Barcelona and Santiago de Compostela (Spain), Hong Kong and Shanghai (People's Republic of China). A synthetic signal database is also explained in this chapter.

3.1 Introduction to Clinical Trials

The collaboration between private and public entities has produced a large quantity of clinical data. The preparation of clinical trial protocols has also been a relevant part of the work completed in this Doctoral Thesis. Some important details to be defined in protocols are as follows:

- Rationale of the study
- Objectives: main and secondary study parameters
- Study design
- Study population: inclusion and exclusion criteria, sample size calculation
- Treatment of subjects
- Investigational medical devices
- Non-investigational medical devices
- Methods: randomization, withdrawal of individuals, etc.
- Safety reporting
- Statistical analysis: primary and secondary study parameters, statistical tests, interim analysis (if any), etc.
- Risk analysis
- Ethical considerations
- Administrative aspects: data protection, reporting, etc.

3.2 Shanghai Database

3.2.1 Aims of the Protocol

The aim of this protocol was to estimate the cardiovascular and cerebral synchronization between cardiovascular and brain oscillators. Brain oscillators are the different frequencies contained in the EEG. Example of brain cardiovascular oscillators are the heart rate and the respiratory rate. The relationship between oscillators was already studied by Musizza [92]. Furthermore, Steriade showed that oscillators were desynchronized during the patient's awake state unlike during anesthesia [93].

3.2.2 Recorded Data Description

Fifteen patients undergoing major surgery under general anesthesia at the Zhongshan Hospital in Shanghai were assessed in this observational study. Details of the patients and operations are reported in **Table 3.1**. Age ranged between 43 and 67 years, with a mean age of 58.9 ± 6.7.

The anesthesia was induced with propofol and remifentanil or fentanyl and sevoflurane was also used for maintenance. Rocuronium, a non-depolarizing agent, was administered to block neuromuscular response. In some cases lidocaine, morphine, atropine or ephedrine were additionally administered. Surface wet-get electrodes (Ambu® BlueSensor for ECG) were used for the qCO monitor. The pressure waveform for LiDCOrapid was obtained with an arterial line. The recordings were assessed simultaneously during the complete procedure, from 3 minutes before induction of anesthesia to 3 minutes after the recovery. The ICG and ECG signals were recorded by the qCO monitor (Quantium Medical, Spain).

SHANGHAI DATABASE PATIENT CHARACTERISTICS

Gender (male:female)	9:6
Age (years)	58.9 ± 6.7
Height (cm)	163.7 ± 6.8
Weight (kg)	61.1 ± 9.1
BMI (kg m^{-2})	22.8 ± 2.6
Operative procedure (No. of patients)	Mastectomy (1) Carotid endarterectomy (1) Cytoreductive surgery (1) Gastrostomy (2) Hepatectomy (2) Nephrectomy (1) Ovarian cystectomy (1) Thyroidectomy (1) Uretescope lithotripsy (4) Hysteroscopic Resection (1)

Table 3.1 Patient Characteristics. Qualitative data are given as absolute frequencies. Age, Height, Weight and body mass index (BMI) are given as mean ± standard deviation

This observational study adhered to the principles of the Declaration of Helsinki and it was conducted in compliance with the requirements of the Zhongshan Hospital Ethical Committee. Exclusion criteria were patients under eighteen years old and pregnant women. Different types of surgeries were included in this database since the objective was the direct comparison between cardiac output monitors in a large variety of clinical situations.

3.3 CMA Database

3.3.1 Aims of the Protocol

The objective of this protocol was to register physiological data in order to validate eventual indicators of anesthetic effects. It was conducted at the Hospital CLINIC de Barcelona (Spain) under the leadership of D. Pedro Luís Gambús, from the Anesthesia department.

3.3.2 Recorded Data Description

One hundred and fifty-three patients undergoing major surgery under general anesthesia were assessed in this observational study. Details of the patients are reported in **Table 3.2**. Age ranged between 18 and 88 years, with a mean age of 50.9 ± 16.4 years and a mean body mass index (BMI) of 25.8 ± 4.6 kg/m².

CMA DATABASE PATIENT CHARACTERISTICS

Gender (male:female)	37:116
Age (years)	50.9 ± 16.4
Height (cm)	162.2 ± 8.2
Weight (kg)	67.8 ± 12.7
BSA (m^2)	1.73 ± 0.21
BMI (kg/m^2)	25.8 ± 4.6

Table 3.2 Patient Characteristics. Gender is given as an absolute frequency. Age, Height, Weight, body surface area (BSA) and body mass index (BMI) are given as mean ± standard deviation

Patients were administered propofol and remifentanil. Anesthesia was induced with a target-controlled infusion system (TCI). The infusion rate of remifentanil was controlled by Minto's pharmacokinetic-pharmacodynamic model with 3 ng/mL (range 1.5 to 5 ng/mL) as effect-site target concentration and the infusion rate of propofol was controlled by Schnider's pharmacokinetic model with 7 μg/mL (range 6 to 10 μg/mL) as effect-site target concentration [94], [95]. Rocuronium, a short-to-intermediate-term muscle relaxant, was administered only in those cases requiring laryngoscopy (54 cases, 35.3%). The single bolus dose of rocuronium was 30 mg administered 2 minutes before laryngoscopy. In two cases, the initial dose was 40 mg.

After intubation, anesthesia was maintained with propofol and remifentanil whose target concentrations were lowered according to the clinician's criteria to an average of 4 μg/mL (range 2 to 7 μg/mL) and 2

ng/mL (range 1.5 to 4 ng/mL), respectively. Additional maintenance doses of rocuronium were used in the form of 10 mg or 20 mg boluses when needed. In some cases, ephedrine and atropine were additionally administered, as **Table 3.3** shows. Methadone was used at the end of surgery as an analgesic in 31% of patients.

The impedance cardiography and electrocardiogram were recorded by the qCO monitor (Quantium Medical, Spain). The Infinity® Gamma monitor (Dräger, Germany) for blood pressure was also used. It offered systolic blood pressure (SBP: the maximum value of the arterial pressure waveform inside the consecutive RR interval), the diastolic blood pressure (DBP: the following minimum value of the pressure waveform) and mean blood pressure (MBP: the average arterial pressure during a single cardiac cycle). The recordings were assessed simultaneously during the complete procedure.

CMA DATABASE PATIENT CHARACTERISTICS

Propofol	153 (100%)
Remifentanil	153 (100%)
Rocuronium	54 (35.3%)
Methadone	47 (30.7%)
Ephedrine	5 (3.3%)
Atropine	26 (17.0%)

Table 3.3 Medications during surgical procedures. Data are presented as absolute frequencies and percentages over the total sample

This observational study was conducted in compliance with the requirements of the Hospital CLINIC de Barcelona. All patients gave their written informed consent. The protocol adhered to the principles of the Declaration of Helsinki and it was approved by the Institutional Review Board of Hospital CLINIC de Barcelona. Patients under eighteen years old or morbidly obese were excluded from the study.

3.4 Other Databases

Some other clinical trials have taken or are taking place thanks to this Doctoral Thesis. The institutions where these studies have taken place are as follows:

- Prince of Wales Hospital (Shatin, Hong Kong Special Administrative Region, People's Republic of China): fluid challenge, tilt changes and

bleeding challenges were applied to fifteen pigs in order to validate the qCO monitor ability to detect those changes.

- Hospital Clínico Universitario de Santiago (Santiago de Compostela, Spain): a comparison between the qCO monitor and FloTrac monitor is currently taking place.

- Universitair Medisch Centrum Groningen (Groningen, the Netherland): a clinical trial to study qCO monitor's ability to track fluid challenges is expected to start in January 2018.

3.5 Synthetic Signals

Using the Shanghai database, synthetic ICG signals were generated in order to use them when known time-frequency characteristics are necessary. This synthetic signals are used for the evaluation of TFDs in Chapter 6.

In order to construct these synthetic signals, the most typical waveform of a real ICG recording was recognized. In our case, a randomly chosen patient from the Shanghai database was chosen. This pattern was later used to create a Fourier-model approximation with several instantaneous frequencies (IFs) and synthetic signals were created including concrete variable time-frequency characteristics.

3.5.1 Pattern Recognition

A pattern recognition algorithm was designed to detect the most typical waveforms which are contained in the ICG signals. Each ICG beat was isolated and normalized for zero mean and unit standard deviation. Moreover, the length of all ICG beats was resampled to a constant number of samples. The starting and end points were defined as the QRS peaks in the ECG before and after an ICG maximal peak. Moreover, ICG maxima were located using the QRS peaks in the ECG as an initial search point. QRS peaks are easy to locate with a Pan-Tompkins approach [96]

The first pattern of the database was the first ICG beat available in the recording. The rest of ICG beats were correlated with all the patterns in the database. For each ICG beat, the pattern which offered a higher Pearson correlation above a threshold th with the beat was then averaged with such beat. Two correlation thresholds were independently studies: $th > 0.85$ and $th > 0.90$. If the correlation threshold was not met, a new pattern was created. Moreover, the algorithm ensured that there will not be two patterns with a cross-correlation higher than 0.95. All this procedure is explained in **Figure**

3.1. In this concrete implementation, when there are 100 patterns, infrequent patterns (<10 repetitions) are canceled.

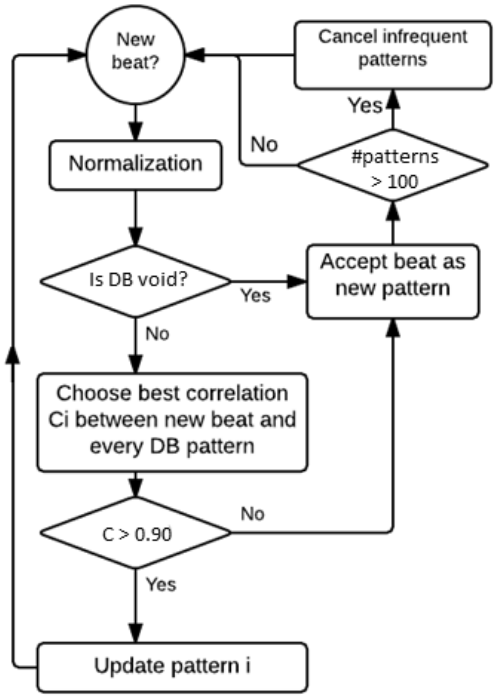

Figure 3.1 Flowchart of the ICG pattern recognition algorithm. Each new beat is normalized and correlated with the rest of the pattern database. The pattern for which the best correlation above 0.90 is obtained is updated with the new beat. Infrequent patterns are also regularly canceled

3.5.2 Template Fourier Modelling

A periodic signal with a frequency $\omega_n = 2\pi/N_p$ can be represented as a Fourier series according to Equation (7). This Fourier series requires an infinite number of terms to accurately reproduce the square wave signal. Generally, a Fourier model for the pattern ICG signal will have a structure with a defined number of terms of a discrete-time Fourier series of frequency $\omega_n = 2\pi/N_p$ where N_p will be the length of the single pattern.

$$x(t) = \sum_{n=0}^{\infty} [a_n \cos(n\Omega_0 t) + b_n \sin(n\Omega_0 t)] = \sum_{n=-\infty}^{\infty} c_n e^{jn\Omega_0 t} \quad (7)$$

where a_n y b_n are real constants and c_n is a complex constant.

Equation (7) implies that the Fourier series requires an infinite number of terms to exactly reproduce the original signal. If this series is truncated, the accuracy of the representation decreases.

3.5.3 Fourier Modelling with Time-Frequency Variations

The Fourier model for the template signal allows modifying the time-frequency characteristics of a longer signal $x(n)$ in a controlled, straightforward fashion, similar to the time-frequency dependency in chirp signals.

Linear and Quadratic Variations

The frequency sweeps considered were linear, which specifies an instantaneous frequency IF sweep given by

$$IF(n) = f_0 + Bn \tag{8}$$

$$B = (f_1 - f_0)/2n_1 \tag{9}$$

In the linear sweep, B ensures that the desired frequency breakpoint f_1 at the time $n = n_1$ is maintained departing from an initial frequency f_0 at the time $n = 0$. For ICG signals, it would be desirable to implement frequency variations from $f_0 = 50$ bpm to $f_1 = 90$ bpm in $n_1 = 10$ seconds in order to test extremely variable conditions.

Furthermore, this frequency sweep can also be quadratic by using Equations (10) and (11).

$$IF(t) = f_0 + Bt^2 \tag{10}$$

$$B = (f_1 - f_0)/3n_1^2 \tag{11}$$

3.5.4 Results

In total, 7,544 beats were analyzed for the first patient. The correlation threshold of 0.85 produced 92 different patterns with at least 4 appearances but 8 patterns covered more than 60% of beats. **Figure 3.2** shows the most typical patterns for this correlation threshold.

A correlation threshold of 0.90 was also studied for comparison. The ICG patterns obtained using either threshold were very similar. However, the number of patterns with at least 100 repetitions differ between both thresholds: it was higher with the th = 0.90 (11 patterns) compared to 10

relevant patterns obtained with a th = 0.85. Moreover, the main pattern was appeared 699 times in the case of the th = 0.90, while in the case of the th = 0.85, the same pattern was repeated 1,154 times.

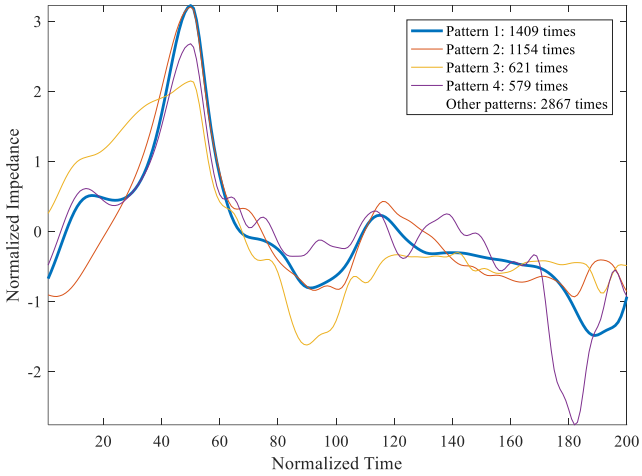

Figure 3.2 Five most frequent patterns in an ICG recording calculated with a correlation threshold of 0.85

The most repetitive pattern with th = 0.85 was selected as the template for the Fourier modeling. However, it was necessary to slightly modify the endpoints of the signal with a smoothing window so that the beginning and the end of the templates happen to meet at the same point without creating noticeable transitions when concatenating several templates together to form a longer signal. All templates have been normalized to zero mean and adjusted to a length N_p = 200 samples.

Two-Term Fourier Model Approximation Results

An approximation of two tones has been used for the Fourier series with a fixed frequency. The results of the model can be observed in **Figure 3.3**. Characteristic points B, C and X are marked on the ICG curve: the point B coincides with the opening of the aortic valve; the point C corresponds to the peak of the ICG signal and it coincides with the ventricular contraction; and the point X corresponds to the closure of the aortic valve [9].

The previous modelled Fourier approximation has been modified in order to include a linear frequency variation. **Figure 3.4A** presents a synthetized ICG with a constant IF and **Figure 3.4B** shows a synthetized

ICG signal which frequency changes in a linear fashion from $f_0 = 50$ bpm to $f_1 = 90$ bpm in 10 seconds.

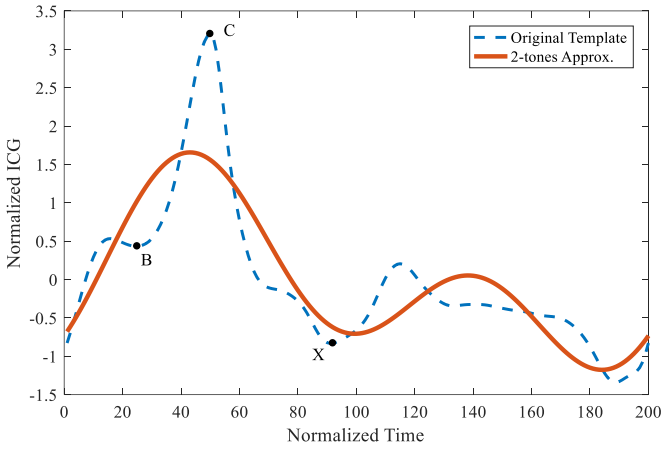

Figure 3.3 Fourier Model of the ICG Pattern: original ICG template (dashed blue) and an approximation of 2 tones of the Fourier model (red). Characteristic points B, C and X are marked on the ICG curve

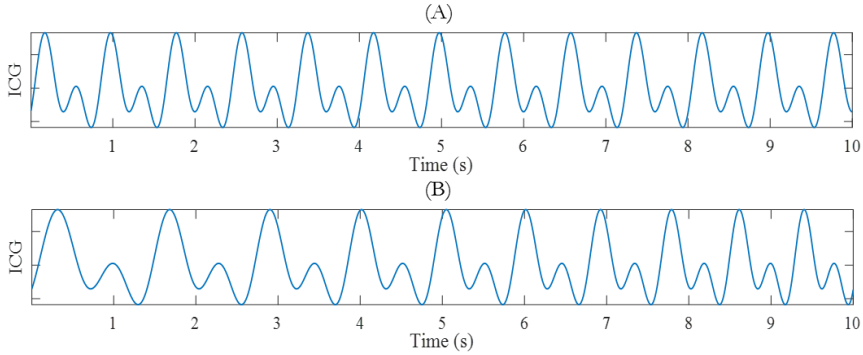

Figure 3.4 ICG signals with a constant instantaneous frequency (A) and a linear frequency variation (B) from $f_0 = 50$ bpm to $f_1 = 90$ bpm in 10 seconds synthetized with 2 tones

The frequency response for the Fourier model of the ICG pattern and for the linearly variable time-frequency ICG in **Figure 3.4B** are expected to have a similar frequency response with some important differences in the shape of the frequency spectrum. The frequency response of the constant-frequency ICG presents a set of periodically distributed peaks corresponding to each of the Fourier terms, as shown in **Figure 3.5A**. For the case of the two-tone synthesized ICG, the linear variation in the signal instantaneous frequencies makes both frequency peaks IF_1 and IF_2 wider (see **Figure 3.5B**), which causes them to interfere with each other as the resulting spectrum shows (in black).

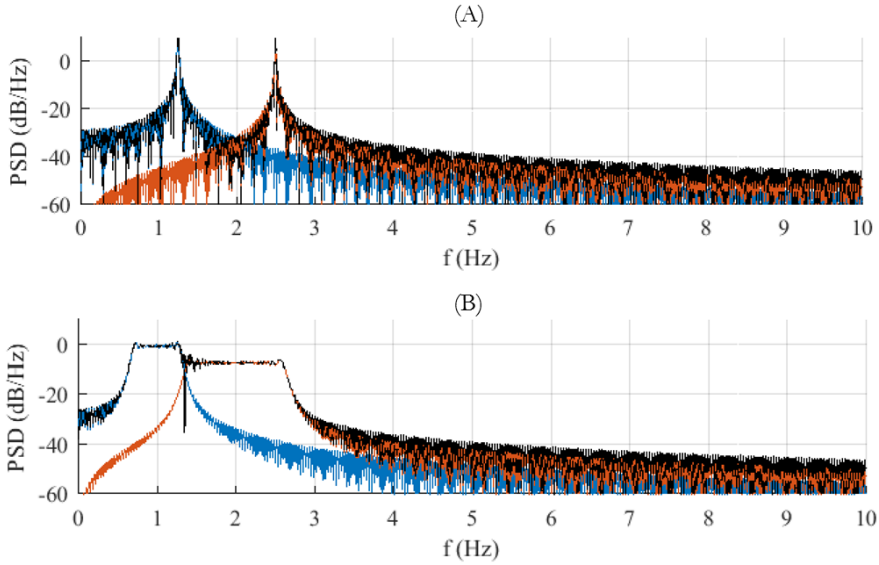

Figure 3.5 Periodograms of the synthetized ICG signals with no frequency variation (A) and with a linear frequency variation (B). Each instantaneous frequency is plotted individually (in color) and the total resulting spectra is also included (in black)

3.5.5 Conclusions

In this chapter, a procedure to create synthetic signals with a concrete exemplification of ICG signals is described. The synthetic ICG signals will be useful to evaluate the performance of different TFDs in Chapter 6.

This page is intentionally left blank.

Chapter 4

Relationship between Heart Rate Variability, Blood Flow and Blood Pressure during Anesthesia

Abstract

Anesthesia is known to exert an influence on the sympathetic and vagal tones of the autonomous central system. This leads to a modification of the hemodynamic state in the patient. This chapter analyses these modifications and relates them to the patient's heart rate variability.

4.1 Introduction

During surgery, the effects of anesthetics in patients have been vastly studied. Propofol-induced hypotension is known to be mediated by an inhibition of the sympathetic nervous system and the impairment of baroreflex regulatory mechanisms [18], [19], [21]–[24]. Besides, propofol also reduces cardiac parasympathetic tone depending on the depth of hypnosis [20] although research showed that its suppression is lower than in the case of the sympathetic tone [17].

Blood pressure (BP) and cardiac output (CO) can be affected by the activity of the parasympathetic and sympathetic stimulations. On the one hand, parasympathetic stimulation decreases heart rate (HR), which in turn, decreases CO and thus BP. On the other hand, sympathetic stimulation influences the heart by increasing its heart rate and its contractile strength. This increases stroke volume (SV) which in combination with the increased HR causes the BP to augment. Besides, the sympathetic stimulation also increases the vasoconstriction of arterioles and veins, which can also cause an increase in the arterioles total peripheral resistance and venous return, respectively. This ultimately also increases BP [97]. Some authors have found some correlation between CO and BP [98].

CO is also related to age in a negative fashion according to different studies [99]–[101]. In a study [99], resting CO was measured in 151 healthy patients by the earpiece dye-dilution method. Cardiac index (CI, as defined in Equation (2)) had a significantly inverse correlation to age in volunteers older than 20 years old. Brandfonbrener reached the same conclusions with a smaller cohort [100] and Boss and his colleagues [101] reported that CO decreases linearly after the third decade at a rate of about 1 percent per year in normal subjects otherwise free of cardiac disease.

Several authors have already studied heart rate variability (HRV) as a way to monitor the activity of the autonomous nervous system (ANS). Deutchman and colleagues [16] used the fact that high-frequency HRV reflects parasympathetic tone to explain that propofol anesthesia reduces parasympathetic tone to a lesser degree than sympathetic tone. This autonomic milieu predisposes the patient to developing bradycardia in response to parasympathetic stimuli. According to previous studies, CO, SV, and HR should decrease after the induction of anesthesia [102] due to the changes in sympathetic and parasympathetic activity, which should also be reflected in HRV indices.

However, the results have sometimes been controversial. Hidaka and colleagues [103] stated that after sedation with propofol, HRV high-frequency (HF) power (HF: 0.15-0.40 Hz) did not change, whereas low-frequency (LF) power (LF: 0.04-0.15 Hz) and LF/HF, an indicator of cardiac autonomic nervous system balance, significantly decreased with propofol. Low-frequency changes are more difficult to interpret since they reflect both sympathetic and parasympathetic activity. Nevertheless, several authors [13] consider LF changes to mainly reflect changes in sympathetic activity. Thus, the LF/HF ratio would reflect the balance between sympathetic and parasympathetic activity.

Remifentanil is an anesthetic often used in combination with propofol. It is known to stimulate the parasympathetic nervous system, and patients with increased parasympathetic tone may be at greater risk of bradycardia after its administration [12], [13], which is reflected in the HF of the HRV [11]. Zaballos and colleagues [14] compared an anesthesia based on propofol with and without remifentanil and results showed that remifentanil depresses sinus node function and most parameters of atrioventricular nodal function such as HRV. This contributes to an explanation for clinical observations of remifentanil-related severe bradyarrhythmias.

In this study, our main objective is to analyze blood flow indices (CO and SV), heart rate variability, and blood pressure during a propofol-remifentanil anesthesia in order to describe how indices are affected after the patients' loss of consciousness. Moreover, the relations of the studied indices with each other and with the patient characteristics such as age are also analyzed. There are several hypothesis which are taken into account. Firstly, CO, SV, and HR should decrease after the induction of anesthesia due to the changes in sympathetic and parasympathetic activity, which should also be reflected in HRV indices. Secondly, CO is to be related to age in a negative fashion according to the studies mentioned previously (although other patient characteristics will also be studied). Finally, BP should also decrease during anesthesia.

4.2 Data Preparation

In total, one hundred and fifty-three consecutive patients undergoing major surgery under general anesthesia at the Hospital CLINIC de Barcelona (Spain) were assessed in this observational study. The details of this database

have been explained in the Chapter 3. Data from a blood pressure monitor and the qCO monitor were recorded.

The synchronization between a noninvasive blood pressure monitor and the qCO monitor was ensured by annotating the exact start time given by the two devices. The BP monitor updates the diastolic, systolic and mean blood pressure values (DBP, SBP, and MBP) every 120 seconds. The qCO monitor updates its indices (HR, CO and SV) every second. This study aimed to compare two anesthesia-related patient states: consciousness and unconsciousness.

During the induction of anesthesia, the moment of loss of consciousness (LOC) was assumed to occur when patients lost response to verbal stimulation. To characterize each state, after checking normality, the registered indices HR, CO, SV and blood pressure corresponding to one-minute length taken 4 minutes after LOC (i.e., unconscious state) were averaged and data corresponding to one-minute length taken 4 minutes before LOC (i.e., conscious state) were also averaged for comparison. Signals were excluded when patient movement corrupted the recorded signal or when the period before the induction had not been registered. For the present analysis, in order to avoid confounding factors, patients were discarded when ephedrine and atropine had been used between 4 minutes before and 4 minutes after LOC.

4.3 Heart Rate Variability

The electrocardiogram (ECG) is the result of recoding the electrical activity of the heart over a period of time using electrodes placed on a patient's body. These electrodes detect the tiny electrical changes on the skin arising from the depolarization of the heart muscle during each heartbeat. This is a noninvasive medical procedure referred to as electrocardiography.

Regarding hemodynamics, the ECG is useful to detect the morphology, amplitude and duration of the cardiac cycle waves. It can also be used to derive other parameters such as the HR and the HRV, which are useful to describe the hemodynamic state of a patient.

4.3.1 Heart Rate

The HR is the speed of the heartbeat measured by the number of beatings of the heart per unit of time – typically beats per minute (bpm). The HR can vary according to the body's physical needs, including the need to absorb oxygen and excrete carbon dioxide.

The normal resting adult human HR ranges from 60–100 bpm. Tachycardia is a fast HR, defined as above 100 bpm at rest. Bradycardia is a slow HR, defined as below 60 bpm at rest. During sleep a slow heartbeat with rates around 40–50 bpm is common and considered normal. When the heart is not beating in a regular pattern, this is referred to as an arrhythmia. These abnormalities of HR sometimes indicate disease.

The correct identification of the QRS complexes of the electrocardiogram signal is the first and the most important stage for analyzing HRV. The RR intervals represent the difference (in time) between consecutive QRS complexes and this is directly related to the instant heart rate ($\mathrm{HR_{ins}}$) according to Equation (12).

$$\mathrm{HR_{ins}\ (bpm)} = \frac{60}{\mathrm{RR_{ins}(s)}} \tag{12}$$

Heart rate can be calculated in an instantaneous way or averaged over a certain period of time (typically, over one minute). In **Figure 4.1**, the QRS complexes can be observed with the different RR intervals. In the lower part of the figure, the series of RR intervals is also plotted.

4.3.2 Heart Rate Variability Calculation

The European Society of Cardiology and the North American Society of Pacing and Electrophysiology [8] refers to HRV as:

"the oscillation in the interval between consecutive heartbeats".

Measurements of HRV are the most widely used indirect techniques for assessing the autonomous nervous system function in the study of several physiological states and diseases. Recent studies [104] have shown that immune system is controlled by vagus nerve through the cholinergic anti-inflammatory pathway. The HRV indices that reflect vagal activity are related to inflammatory markers [7, 8].

Changes in HRV may be evaluated using a variety of methods. The most common are the time-domain and the frequency-domain measures [8]. After detecting each QRS complex in an ECG, the so-called normal-to-normal (NN) intervals are simple to calculate. NN intervals refer to the intervals between normal R peaks. Simple HRV time-domain indices that can be calculated

include the mean NN interval, the mean heart rate, the difference between the longest and shortest NN interval, etc.

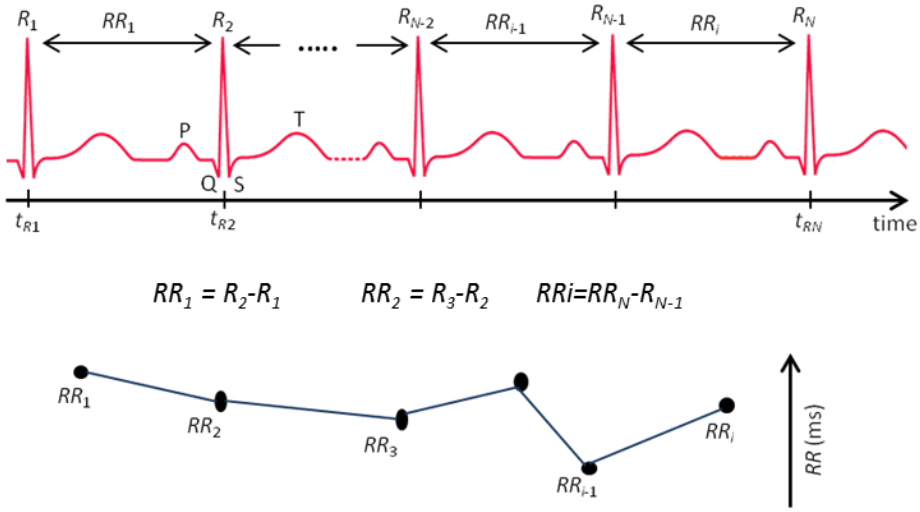

Figure 4.1 ECG waveform and RR interval time series

Frequency-domain parameters can also be calculated using different techniques. Power spectral density analysis provides the basic information of how power distributes as a function of the frequency. Methods for its calculation may be generally classified as non-parametric and parametric. In the real-time algorithm implemented in the qCO monitor, non-parametric methods are preferred due to the simplicity of the Fast Fourier Transform (FFT) and the high processing speed.

Three different frequency ranges can be identified: very low frequency (VLF: < 0.04 Hz), low frequency (LF: 0.04-0.15 Hz) and high frequency (HF: 0.15-0.4 Hz). However, VLF assessed from short-term recordings (< 5 min) is a dubious measure and should be avoided if short-term measurements are desired. The main indices to assess the HRV are shown in **Table 4.1**. Some of them have been implemented in the qCO monitor.

For the calculation of the HRV indices, the beat-to-beat RR intervals were linearly-splined and interpolated at 2 Hz to obtain a constant sampling frequency. The HRV power spectral density was calculated by means of a Fast Fourier Transform with a Hamming window.

HEART RATE VARIABILITY INDICES

Index	Description
RMSSD (ms)	Root mean square differences between successive RR intervals
SDSD (ms)	Standard deviation of differences between successive NN intervals
pNN50 (%)	Number of interval differences of successive NN intervals greater than 50 ms divided by the total number of NN intervals.
HF (ms^2)	Power in high frequency range (0.15 – 0.4 Hz)
HFn (n.u)	HF power in normalized units, HFn = HF/(LF + HF)
LF (ms^2)	Power in low frequency range (0.05 – 0.15 Hz)
LFn (n.u)	LF power in normalized units, HLn = HF/(LF + HF)
LF/HF (n.u.)	Energy balance between LF and HF.
TP (ms^2)	Total Power

Table 4.1 Heart Rate Variability Indices [8]

The following indices for HRV were then calculated: VLF (up to 0.05 Hz), LF, and HF. Derived indices were: normalized LF (LFn = LF/(HF+LF)), normalized HF (HFn = HF/(HF+LF)) and the LF/HF ratio. Three time-derived indices were also calculated: the standard deviation of differences between adjacent intervals (SDSD), the square root of the mean of the sum of the squares of differences between adjacent intervals (RMSSD) and the rate of pairs of adjacent intervals differing by more than 50 ms in the recording (pNN50). These indices were calculated once during the pre-induction segment and once during the post-induction segment. HR was included as a default index in the qCO monitor.

4.4 Statistical Analysis

Normality was assessed using the Kolmogorov-Smirnov test. Normally-distributed, quantitative data are presented as mean ± SD and qualitative data as frequency (percentage). Non-parametric quantitative data are presented as median (Inter-Quartile Range, IQR [range of maximum and minimum values]).

Since some data were non-normally distributed, a non-parametric test, the Wilcoxon signed-rank test, was used to investigate whether the analyzed indices changed after induction of anesthesia. Receiver operating

characteristic (ROC) analysis was used to assess the ability of the studied indices to detect the occurrence of LOC. Another non-parametric test, the Mann–Whitney U-test, was applied to investigate the differences in the decrease of hemodynamic values between men and women. All p-values reported are two-sided and p-value<0.05 was considered to be statistically significant.

The relationship between indices from hemodynamic, time-domain, frequency-domain analysis and patient characteristics was assessed using Spearman's coefficient of correlation (ρ).

4.5 Variations after Loss of Consciousness

After discarding the cases for which the period prior to the induction of anesthesia had not been recorded and the cases in which the recorded signals contained artifacts during the periods before and after the loss of consciousness, a total of eighty-two patients were finally included in the final study. The details of the patients are reported in **Table 4.2**. The patient characteristics which were analyzed during this study included age, height, weight, lean body mass (LBM), body surface area (BSA), body mass index (BMI) and gender.

Table 4.3 shows the results comparing all the indices before and after patients' LOC. There is a reduction in CO, SV, and HR and a reduction in DBP, SBP, and MBP. All time-derived and frequency-derived HRV indices also significantly decrease after LOC except from the normalized high frequency index (HFn) which significantly increases. The decrease in BP (either DBP, SBP, and MBP) is always higher than 20% (median value), slightly higher than the decrease in CO. The SV and HR indices decrease by around less than 10% (median value). Absolute frequency-derived HRV indices decrease by around 63% (median values for VLF, LF, HF, Total Power), while the ratio LF/HF decrease by 34%, HFn increases by 28% and LFn decreases by 8%. Time-derived HRV indices decrease by between 20% for pNN50 and around 33% for RMSSD and SDSD (median values).

The Wilcoxon test shows that the variation in all indices is always statistically significant with the exception of the LF/HF ratio. **Table 4.3** shows the characteristics of the ROC curve for the detection of LOC. The ROC curves for frequency-derived HRV indices have an area under the curve (AUC) around 0.56-0.59 while the time-derived HRV AUCs are slightly higher (0.62-0.68) and hemodynamic AUCs are the highest, around 0.63-0.85.

PATIENT CHARACTERISTICS	
Age; years	51.9 ± 14.9
Height; cm	162.6 ± 8.8
Weight; kg	69.3 ± 13.6
LBM; n.u.	47.6 ± 7.8
BSA; m^2	1.75 ± 0.2
BMI; kg/m^2	26.3 ± 5.0
Gender; male/female	21/61

Table 4.2 Patient characteristics: qualitative data are presented as absolute frequencies; quantitative data are presented as mean ± standard deviation. LBM: lean body mass; BSA: body surface area; BMI: body mass index.

4.6 Relationship between Blood Flow, Blood Pressure and HRV Indices

Results showed that CO does not significantly correlate with blood pressure (either DBP, MBP or SBP) but SV presents certain negative correlation with blood pressure. The percentage variation Δ(%) between before and after induction in fluid indices and pressure indices does not correlate either. The results in **Table 4.3** confirm that all HRV indices decrease after the induction of anesthesia except from the HFn which increases after loss of consciousness.

All time-derived HRV indices in **Table 4.4** (SDSD, RMSSD, and pNN50) are much related to each other although their correlations are higher before the loss of consciousness than afterwards. The same time-derived HRV indices are also related to the absolute frequency-derived HRV indices (VLF, LF, HF, and total power) in a positive fashion both before and after LOC.

Finally, time-derived HRV indices are weakly correlated to HFn in a positive fashion but so are they to LFn and LF/HF in a negative fashion. Regarding the variations of the HRV indices, ΔSDSD and ΔTotal power, and ΔHF and ΔRMSSD strongly correlate with each other. No statistically-significant correlations for HRV indices above 0.50 have been found with either blood flow indices (CO and SV) or blood pressure indices.

Regarding the normalized HRV frequency indices (not included in **Table 4.3**), both before and after LOC, weak correlations were found for RMSSD and pNN50 with LFn (negative) and with HFn (positive). All correlations for normalized HRV indices were similar with $|\rho| < 0.36$, p-value < 0.05.

RECORDED INDICES BEFORE AND AFTER LOSS OF CONSCIOUSNESS

Indices	Pre- LOC	Post-LOC	Δ (%)	AUC
Hemodynamics				
CO (L/min) +	4.8 (1.3 [3.1–10.1])	4.0 (0.9 [2.6–6.5])	-15.7 (12 [-60 – -2])	0.74
SV (mL/beat) +	68 (15 [43–127])	63 (11 [39–104])	-8.1 (12 [-55 – 7])	0.63
SBP (mmHg) +	135 (39 [93–197])	101 (33 [51–160])	-24 (15 [-59–9])	0.85
DBP (mmHg) +	78 (16 [45–100])	59 (23 [34–97])	-24 (21 [-47–23])	0.84
MBP (mmHg) +	102 (23 [63–132])	77 (27 [41–121])	-23 (21 [-51–17])	0.84
Time-derived HRV				
HR (bpm) *	69.4 (13 [55–117])	62 (12 [46–104])	-9.5 (7.7 [-35 – 13.2])	0.67
RMSSD (ms) +	22 (20 [0–346])	14 (14 [0–300])	-32 (58 [-80 – 580])	0.66
SDSD (ms) +	38 (27 [0–237])	24 (21 [0–223])	-34 (62 [-87 – 306])	0.68
pNN50 (%) *	1.6 (7.2 [0–45])	0 (1.9 [0–36])	-20 (161 [-87 – 625])	0.62
Frequency-derived HRV				
VLF (ms^2) *	396 (615 [0–6981])	114 (371 [0–8441])	-60 (128 [-99 – 3804])	0.69
LF (ms^2) +	387 (713 [0–5401])	98 (196 [0–17663])	-67 (104 [-100 – 2633])	0.68
HF (ms^2) *	110 (238 [0–13391])	35 (112 [0–15367])	-67 (110 [-98 – 6273])	0.66
T.P. (ms^2) +	1105 (1529 [0–25884])	379 (874 [0–45875])	-66 (126 [-98–2165])	0.56
LF/HF (n.u.)	2.8 (5 [0–21])	1.9 (4 [0–80])	-34 (234 [-99 – 3513])	0.56
HFn (%) *	26 (28 [0–82])	34 (41 [0–94])	28 (192 [-90 – 1155])	0.56
LFn (%) *	74 (28 [0–96])	65 (41 [0–99])	-8 (60 [-94 – 401])	0.56

Table 4.3 Average values before and after loss of consciousness (pre-LOC and post-LOC) presented as median (IQR [Range]). The mean variation Δ(%) from pre- to post-LOC and the Area Under the Curve (AUC) of the ROC characteristics are also included. n.s. non-significan level; T.P. total power; Wilcoxon test p-values < 0.05 *, <0.001

4.7 Relationship between Indices and Patient Characteristics

Regarding the blood flow indices (CO and SV), no index correlates with patients' height. CO and SV indices weakly correlate with the remaining characteristics of the patients, both before ($\rho \in$ [-0.36, -0.26], p-value < 0.05) and after induction of anesthesia ($\rho \in$ [-0.47, -0.29], p-value < 0.05). Age also correlates with CO (before LOC) and SV. In all cases, statistically significant correlations are negative and rather weak ($\rho = \in$ [-0.42, -0.28], p-value < 0.05).

Regarding the blood pressure indices, all of them follow the same pattern: SBP, DBP, and MBP before induction all correlate with age (ρ is 0.59, 0.57 and 0.66, respectively, p-value < 0.05), height (ρ is -0.40, -0.42 and -0.42, respectively, p-value < 0.05), and BMI (ρ is 0.30, 0.52 and 0.42, respectively, p-value < 0.05). The percentage decrease in SBP and MBP after LOC also has certain correlation with age in a positive way (ρ is 0.50 and 0.41, p-value < 0.05).

The relationship between patient characteristics and HRV indices has been quantified. HR does not correlate with patient characteristics either before or after induction, but its variation after induction shows a slight correlation with weight (ρ = -0.30, p-value < 0.05) and LBM (ρ = -0.35, p-value < 0.05). Age correlates positively with SDSD, RMSSD, LF, HF, HFn, and the LF/HF ratio. In all cases, p-values are below 0.05. No meaningful differences have been found for the remaining patient characteristics.

Finally, in regard to gender, statistically significant differences have been found for the percentage decrease in heart rate and cardiac output. The ΔHR(%) was -5.4±7.2 for men and -10.7±8.2 for women (p-value = 0.011). The ΔCO(%) was -13.8±6.5 for men and -19.2±10.2 for women (p-value = 0.033). Statistically significant differences have been found for the CO at pre-LOC according to gender (COpre = 4.47±0.86 for men and COpre = 5.13±1.16 for women, p-value = 0.016). No statistically significant differences have been found for gender and SV, BP, and HRV indices.

CORRELATION P BETWEEN HRV INDICES.

SDSD	Pre-LOC																					
	Post-LOC	0.54																				
	Δ(%)	-0.24	0.61																			
RMSSD	Pre-LOC	**0.92**	0.65	-																		
	Post-LOC	0.65	**0.81**	0.31	**0.79**																	
	Δ(%)	-	0.24	0.65	-	0.35																
pNN50	Pre-LOC	**0.84**	0.53	-	**0.88**	0.67	-															
	Post-LOC	0.61	0.63	0.22	**0.70**	**0.86**	0.36	0.63														
	Δ(%)	-	-	-	-	-	0.68	-	0.49													
VLF	Pre-LOC	0.65	0.27	-	0.48	0.32	-	0.42	0.42	-												
	Post-LOC	0.35	**0.88**	0.62	0.42	0.55	-	0.36	0.29	-	-											
	Δ(%)	-	0.37	0.45	-	-	-	-	-	-	-	0.54										
LF	Pre-LOC	**0.85**	0.36	-0.24	**0.73**	0.46	-	0.67	0.42	-	0.53	0.22	-									
	Post-LOC	0.42	**0.74**	0.37	0.51	**0.75**	0.29	0.47	0.43	-	-	**0.74**	0.39	0.31								
	Δ(%)	-	0.30	0.50	-	0.26	0.54	-	-	-	-	0.33	0.27	-	0.50							
HF	Pre-LOC	**0.82**	0.65	-	**0.96**	**0.79**	-	**0.77**	0.65	-	0.37	0.43	-	0.62	0.53	-						
	Post-LOC	0.52	**0.75**	0.33	0.63	**0.83**	0.27	0.58	0.58	-	-	0.69	0.34	0.39	**0.92**	0.38	0.61					
	Δ(%)	-	-	0.58	-	0.23	**0.87**	-	-	-	-	-	-	-	0.31	0.47	-	0.28				
Total Power	Pre-LOC	**0.95**	0.57	-	**0.93**	**0.70**	-	**0.78**	0.64	-	**0.71**	0.37	-	**0.84**	0.45	-	**0.88**	0.54	-			
	Post-LOC	0.48	**0.84**	0.44	0.59	**0.81**	0.27	0.53	0.52			**0.83**	0.43	0.35	**0.97**	0.43	0.59	**0.96**	0.28	0.51		
	Δ(%)		0.56	**0.77**		0.43	0.62					0.67	0.56		**0.72**	**0.70**		0.63	0.64		**0.71**	
		Pre-LOC	Post-LOC	Δ(%)	Pre-LOC	Post-LOC	Δ(%)	Pre-LOC	Post-LOC	Δ	Pre-LOC	Post-LOC	Δ(%)	Pre-LOC	Post-LOC	Δ(%)	Pre-LOC	Post-LOC	Δ(%)	Pre-LOC	Post-LOC	
		SDSD			RMSSD			pNN50			VLF			LF			HF			Total Power		

Table 4.4 Correlation ρ between HRV indices. The values presented correspond to the Spearman's coefficient when p-value < 0.05 (*) or p-value < 0.01 (**). Otherwise, non-significant values are obtained

4.8 Discussion of Results

Results show that after LOC, there was a decrease in blood pressure indices, blood flow indices, and HRV indices (p-value < 0.05). The decrease in LF band indexes can be directly related with an increase in high-frequency HRV (p-value < 0.05). However, no significant differences were observed in the LF/HF ratio of the HRV between before and after LOC.

This work has obtained similar results as former studies with much larger cohorts. In previous studies, Gabarrón et al. [102] showed that the decrease in CO after induction was 23% and Momota [107] showed that blood pressures at loss of response to stimulation and 5 to 15 minutes after intubation were significantly lower than those before induction.

In our study, SV was inversely-correlated with any BP but these indices decreased after LOC. These facts are compatible since the decrease in BP was much larger than the decrease in SV. No correlation was found between BP and CO. Guyton [108] explained that the pumping action of the heart is ultimately responsible for BP. Increases or decreases in CO can result in increases or decreases respectively in BP. Several studies [98], [109] have reported a positive correlation between CO and BP and in our study only SV has shown a statistically significant relationship with BP. Theoretically, MBP is related to systemic vascular resistance and CO, which in turn is related to HR and SV. In our study, the correlations between MBP and the HR and between MBP and SV are similar with opposite sign, which makes interpretation non-trivial.

In the HRV spectral decomposition, the HF band (0.15–0.4 Hz) is claimed to reflect the parasympathetic autonomic modulations [8], [110], while the LF band (0.04–0.15 Hz) has been suggested to primarily represent sympathetic cardiac activation [111]. Nevertheless, evidence supporting the cardiac sympathetic origin of the LF component is not very strong, and recent work suggests that the LF band does not reflect cardiac sympathetic outflow per se but simply modulation of cardiac autonomic drive via the baroreflex. This is a rapid negative feedback loop in which an elevated BP reflexively causes the HR to decrease and the BP to decrease, and which has been explained by several research groups [111]–[113].

During anesthesia, remifentanil is known to cause hypotension and bradycardia either by parasympathetic activation (HF) and/or by other

negative chronotropic effects [11]–[14]. Remifentanil also decreases sympathetic action [15]. Propofol during anesthesia reduces parasympathetic tone to a lesser degree than sympathetic tone [16]–[24]. The combination of remifentanil and propofol could therefore imply a maintained or slightly-reduced vagal tone and a reduced sympathetic tone.

In our case, the total power decreased after the loss of consciousness, which is in line with the previous statements and is an index of sympathetic nerve predominance [114]. In fact, the LF/HF ratio had an increased tendency and LF remained higher than HF (vagal tone) after the induction of anesthesia. This could be in line with the before-mentioned assumptions by some authors regarding the sympathetic character or the modulation of cardiac autonomic drive via the baroreflexes of the low-frequency HRV.

Most time-derived HRV indices positively correlate to each other as suggested in previous studies [8] since all these measurements of short-term variation are estimates of high frequency variations in heart rate. Moreover, time-derived HRV indices decrease as frequency-derived HRV indices decrease although, as already discussed, the variation in HF is larger than the variation in LF and therefore time-frequency indices correlate in a positive way with HFn and in a negative way with LFn.

Confounders like age, gender, height, weight, and BMI that might have possible influences on hemodynamics and HRV have been considered. Our results show that BP (SBP, DBP, and MBP) both before and after LOC is higher when age and BMI also are. The BP before LOC is inversely proportional to height. Nonetheless, several articles reported a decrease in blood fluid indices with age [99]–[101]. CO and SV indices correlated in a negative fashion with age, weight, LBM, BSA, and BMI while HR showed no correlation. In a study by Park and colleagues, there was no significant decrease in HR with increasing age [115] but some other studies have found evidence of such a decrease [116]. Regarding HRV, Fagard [117] and Piccirillo [118] found an age-related decrease in nearly all spectral components in healthy subjects: SDSD, LF and HF were significantly decreased with age. In our case, we have found that almost all spectral components after loss of consciousness and the percentage variation of HRV indices correlated in a positive way with age. Since most HRV variations were negative, the previous statement suggests that HRV indices changed in a lesser degree as their age increased.

Our study presents some limitations which must be considered. First, the qCO monitor is not a gold standard method for cardiac output monitoring. All noninvasive methods for the detection of the cardiac output are known to exhibit a certain error. Furthermore, the pharmacological effects of the drugs infused in the patients may vary depending on the target concentrations. This is especially true when analyzing the modifications in the vagal and sympathetic tones caused by propofol and remifentanil. Therefore, the hemodynamic and HRV measurements might also be affected by the different concentrations used in every case. In fact, Kanaya [20] and colleagues showed that propofol reduces cardiac parasympathetic tone depending on the depth of hypnosis. These facts do not reduce the validity of results but should be taken into account especially in future works for which information from depth-of-anesthesia monitors should be included. Subsequent studies in this Doctoral Thesis have taken into account the depth of anesthesia in the analysis.

4.9 Conclusions

In conclusion, this work has provided extensive results regarding the changes in blood flow, blood pressure, and HRV during surgical operations with remifentanil and propofol and has validated previous results found in the literature. There was a decrease in CO and all BP indices after LOC. HRV indices except HFn have also decreased after LOC indicating a decrease in both sympathetic and vagal activity. Finally, gender differences in HR and CO, and age differences in HRV measurements have been found after LOC, but not before.

This page is intentionally left blank.

Chapter 5

Time Distance between the ECG and the ICG: the RC Segment

Abstract

Several studies have concluded that the time difference between the R peak in the electrocardiogram and the C point in the impedance cardiogram is a measure for the time delay between the electrical and mechanical activity of the heart. This chapter investigates the RC segment and compares it with other hemodynamic measures.

5.1 Introduction

The organization of this chapter is as follows. The basic calculations for the ECG and the ICG signals by the qCO monitor are presented. Then, the RC segment which relates ECG and ICG is discussed and analyzed on a large set of cases from the CMA database described in Chapter 3. Results are finally presented and discussed.

5.2 ECG Calculations

The qCO implementation is based on the well-known algorithm of Pan and Tompkins [96] for the real-time QRS complexes detection. This algorithm takes into account information about slope, amplitude and width of the QRS complexes in order to detect a large number of QRS morphologies. The set of filters and methods enhances QRS complexes while suppressing noise and artifacts (**Figure 5.1**). We have partially modified some of its stages to adapt it to our sampling rate (250 Hz).

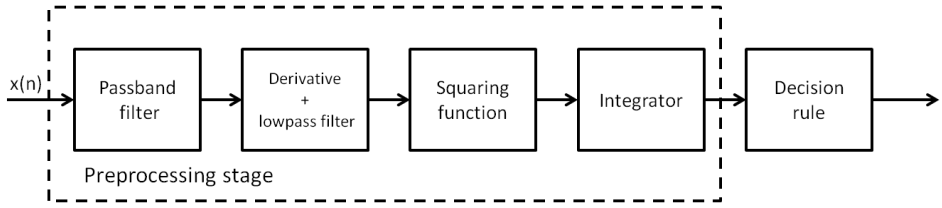

Figure 5.1 Block diagram of the implemented QRS-detection algorithm. The output is the position within the QRS complex where the R peak is situated

The main goal of the band-pass filter is to improve signal-to-noise ratio to achieve good detection performance. The filter is a band-pass 4^{th}-order IIR Butterworth filter with unitary gain between 10 and 30 Hz. It therefore attenuates influence of noise due to EMG, 50/60Hz interference, baseline wander, and P and T waves interferences whilst preserving the spectral contents of the QRS complex.

The differentiation is based on a high-pass filter. The general aim is to find the slope information in the QRS complexes, which is essentially different from the other waves in the ECG. With this procedure, higher frequencies that are characteristic for the QRS complex are emphasized and lower frequencies that are characteristic for P and T waves and baseline wander are attenuated. However, differentiation also amplifies higher frequencies due to noise, thus a low-pass 2^{nd}-order Butterworth filter with $f_c = 15\ \text{Hz}$ is used for smoothing the output.

Squaring is a nonlinear operation which turns all samples positive. This is better suited for the threshold detection and it is also important since:

- it enhances QRS complex attenuating the remaining background noise, and
- it emphasizes the QRS complex (emphasizing large differences arising from QRS complex whereas small differences from P and T waves are suppressed).

The final processing stage is a moving window integrator whose main goal is to obtain a signal which includes information about both the slope and the width of the QRS complex. The result is a smoothing version of the output from the preceding operations. It is very important to choose a proper width of the window. If it is excessively wide, the resulting integration waveform will contain the QRS complexes and T waves together; if it is excessively narrow, the resulting waveform will contain several peaks caused by the same QRS complex. The transfer function of this block is given by Equation (13).

$$H(z) = \frac{1 + z^{-1} + z^{-2} + \cdots + z^{-(N-1)}}{N} \tag{13}$$

where N is the window length. In the qCO monitor, N = 38.

After the processing stage, the decision block locates the QRS complexes in an adaptive manner taking into account refractory periods of the QRS complex, eventual high T waves and abnormally high QRS complexes which might distort thresholds. In the qCO monitor, R peaks will be necessary for the calculation of the heart rate, the heart rate variability and the search of characteristic points in the impedance cardiogram.

5.3 ICG Calculations

The impedance cardiograph signal (ICG) represents the changes of the thoracic impedance due to variations in the blood flow. In practice, the raw impedance signal Z (in **Ω**) is transformed into the ICG waveform (in **Ω**/s) by using the first derivative to remark inflection points of the raw Z signal. The most important characteristics points of the ICG waveform are points B, C and X **(Figure 2.3**). All these points are associated to distinct physiological events within the systolic part of the cardiac cycle. In that sense, R wave from ECG signal can be an important reference for detecting such events.

ICG signal is extremely sensitive to artifacts due to movements and respiration. Baseline variations can considerably alter hemodynamic parameters obtained with the ICG characteristic points. High frequency interferences can also affect accuracy in estimating some characteristics points, essentially the B point. Therefore, a combination of low pass filters is applied after the derivative as it can be seen in **Figure 5.2**.

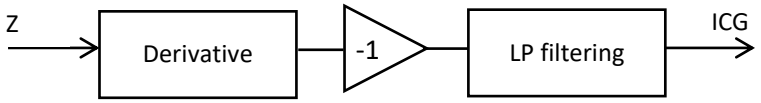

Figure 5.2 Blocks diagram of the algorithm for calculation of ICG signal from the impedance signal (Z)

The goal of the first derivative procedure is to remark inflection points on Z signal. These inflection points are indeed the characteristic points of interest. Derivative procedure also amplifies the high frequency noise so a block to attenuate this adverse effect is crucial. The derivative operation is indeed a high-pass filtering which attenuates the baseline drifts (due to movement or respiration) and low-pass filtering stage attenuates the high-frequency noise improving accuracy when detecting the characteristic points. Finally, the middle block in **Figure 5.2** provides the negated version of the ICG signal, according to a typical medical representation.

The last step in the initial ICG process is to find the C and B points of each ICG beat taking the R peak in the ECG as a reference. These points are located by searching the minimum and maximum points within a window before and after the R peak as shown in **Figure 2.3**.

5.3.1 Basic Artifact Rejection and Correction Criteria

There are several criteria which have been implemented in order to improve the quality of the detection of characteristic points of ECG and ICG. Some of them are as follows:

- Out of range of the raw ECG and ICG signals: segments are discarded if any sample is out of range according to some amplitude thresholds.

- Adjustment of RR in the ECG and C and B in the ICG according to moving exponential averages (MAEs). MAEs are stored for the RR segment and the amplitude values of C and B points. Thresholds based on such MAEs are used in order to detect and correct aberrant detections.

In addition, in this chapter, the relationship between ECG and ICG periods (i.e., RR and CC segments) is investigated in order to set a new artifact rejection criterion.

5.3.2 Indices extracted from ICG signals

In addition to the heart rate variability indices described in the Chapter 4, the qCO monitor also displays the patient's cardiac output and stroke volume, which are calculated by using the ICG signal.

When determining stroke volume from thoracic impedance changes, Kubicek and his colleagues [119] made some assumptions concerning the relationship between stroke volume and the net change in the thorax blood volume. In a very simple model, the impedance of the thorax can be considered to be divided into two parts: the impedance of tissues and the impedance of fluids. When the patient does not breath, the impedance is constant, except the amount and distribution of blood.

The amount of blood in a patient's thorax changes as a function of the heart cycle [120]. During systole, the right ventricle ejects an amount of blood into the lungs which equals the stroke volume. This can be determined by means of the impedance cardiography. Several formulation has been employed during the past years but Kubicek's original equation was as in (14):

$$SV = \rho_b \frac{l^2}{Z^2} \left|\frac{dZ}{dt}\right|_{min} \cdot t_e \tag{14}$$

where ρ_b is the resistivity of the blood ($\Omega \cdot cm$), l is the mean distance between the inner electrodes (cm), Z is the mean impedance of the thorax (Ω), t_e is the ejection time and $|dZ/dt|_{min}$ is the absolute maximum deviation of the first derivative signal during systole (Ω/s), which is written as ICG in the rest of this text.

5.4 The RC Segment

Electrical impedance on the thorax varies in a synchronous manner with the heart activity. Several applications have been found using the derivative of this variation, which is called Impedance Cardiogram (ICG). A major application is the work developed by Kubicek [121] on the cardiac output characterization of patients through ICG signals.

According to the work developed by Meijer [122], the comparison of the time relationships between ICG and the ECG can be of special interest to evaluate the hemodynamic behavior of a patient. Regardless of the multiple sources of the signal, the ICG reflects the mechanical and hydrodynamical aspects of the cardiac cycle, while the ECG reflects the electrical aspect of the cardiac activity. Therefore, the time difference between ECG and ICG can be regarded as the time difference between the electrical and the mechanical aspects of the heart.

The advantage of this perspective is that both ECG and ICG signals are easily recorded: ECG and ICG systems are noninvasive, simple to apply and do not require sophisticated hospital environment. ECG and ICG signals have proven to be useful even in complicated setting such as during functional magnetic resonance [123]. The time difference between the ECG and ICG can be estimated using the cardiac pre-ejection period (PEP). Several authors [124], [125] have studied the PEP, which has been found to relate to the sympathetic autonomous nervous activation, but not to the parasympathetic activity.

The autonomic nervous system controls mainly automatic body functions that are engaged in homeostasis, such as heart rate, respiratory rate and renal function. The sympathetic nervous system prepares the human body when danger and stress occur while the parasympathetic nervous system regulates resting states. This activity can be measured using ICG and ECG signals through the PEP [126]. A large variety of applications of the PEP has been developed during the last years. For instance, since an increased pre-ejection period is an indication of decreased contractility [127], Ashouri proposed to measure PEP and stroke volume changes outside the clinic to provide insight into the severity of their condition [128]. Other recent works relate PEP to stress assessment [129] or hypotension [130], [131].

PEP is measured between the Q wave onset of the ECG signal and the C point or upstroke in the ICG signal. Nevertheless, these points are not easy to locate and can be greatly distorted in some cases. In fact, from a mathematical point of view, it would be more efficient to calculate the difference between the R peak in the ECG and the C point in the ICG, the RC interval, since these are local maxima. Meijer and colleagues [122], [132] have already worked on this RC interval, which they called the initial systolic time interval. In their study, the PEP and the initial systolic time interval were analyzed under different conditions and behaved largely similarly in all cases and maintained a significant correlation. Besides that, this interval has also

been studied against other intervals such as the RR [133] and under different perturbations such as a Valsalva maneuver [134]. During exercise, the RC interval decreased with increasing heart rate (amount of heart beats per minute, HR) and the relative proportion of RC, RC/RR, was found to also decrease with increasing HR [133]. During a Valsalva maneuver, the influence of the Frank-Starling mechanism (explained in Chapter 2) was definitely observed, which is to some extent consistent with reports on the time course of sympathetic activation [134].

Theoretically, the initial systolic time interval or RC interval depends on three factors: the preload of the heart by way of the Frank-Starling mechanism, the afterload of the heart caused by the peripheral resistance, and the autonomic nervous control. Smorenberg et al. [135], [136] studied the RC interval and PEP in patients during fluid infusion. Preliminary results showed significant relationships between the initial systolic time interval and cardiac output (CO) and between changes in both of these indices before and after fluid administration. This indicated that the initial systolic time interval is dependent upon preload via the Frank-Starling mechanism, and that the initial systolic time interval has the potential to be used as a clinical parameter assessing preload.

Nevertheless, the conclusions of one of the last works published about this interval highlighted the need to further analyze these parameters in different settings [134]. Several studies have compared the RC interval with several time markers of the heart cycle but databases are always comparatively small. For instance, van Eijnatten [137] and colleagues used a database of 16 healthy patients to show that the shortening of the RC interval with increasing heart rate in response to an exercise stimulus was caused by a shortening of the PEP. To the best of our knowledge, all studies have been conducted in laboratory settings.

The present study uses a large database to characterize the RC interval and its relationship with the RR and CC intervals during surgery in operating rooms. Furthermore, the RC interval has also been compared with the patients' blood pressure during the whole surgical procedures. The relationship between these intervals and patient characteristics is also studied.

5.5 Data Preparation

The synchronization between both the qCO monitor and the noninvasive blood flow monitor (Dräger Infinity® Gamma monitor) was ensured by annotating the exact start time given by the two devices. The blood pressure monitor updates its blood pressure values (diastolic, systolic and mean) every 120 seconds. The ECG and ICG signals registered by the qCO monitor were processed to detect the R peaks in the ECG and the C peaks and B points in the ICG. **Figure 2.3** shows the position of these characteristic points.

Once R and C peaks were found, for each consecutive heart beat the intervals RR, RC and CC were calculated. Since RR, RC and CC intervals occurred in every heart beat but the blood pressure was measured less often, there were more RR, RC and CC intervals detected than blood pressure points. Thus, the nearest RR, RC and CC intervals were chosen for each blood pressure measurement point in order to create pairs of data points to compare.

This study also aims to compare two anesthesia-related patient states: consciousness and unconsciousness. During the induction of anesthesia, the moment of loss of consciousness was considered to occur when patients lost response to verbal stimulus. To characterize each state, data corresponding to one-minute length taken 4 minutes before LOC (i.e., conscious state) were averaged and data corresponding to one-minute length taken 4 minutes after LOC (i.e., unconscious state) were also averaged for comparison. Signals were excluded when patient movement corrupted the recorded signal.

5.6 Statistical Analysis

Normality of distributions was assessed using a Kolmogorov-Smirnov test. Relationships between time intervals, blood pressure indices, and patient characteristics were assessed using Spearman's coefficient of correlation (ρ). A non-parametric test, the Mann–Whitney U-test, was applied with the significance level set at p-value < 0.05 to investigate the differences in gender. Since some indices were normally distributed, the t-Student test was used to investigate whether those hemodynamic indices changed after LOC. Quantitative data are presented as mean $\pm$ standard deviation (SD) and qualitative data are presented as frequency (percentage).

The RR, RC, CC and RC/RR intervals were statistically described and so were SBP, DBP and MBP. The relation between all those indices was analyzed using correlation and regression techniques. Moreover, the correlation between time-shifted versions of RR and RC was studied and the decorrelation velocity, the negative slope of the linear regression of the Spearman's coefficients once the decrease in the correlation is linear, was calculated. Finally, the relationship between the mean of all indices before and after LOC was investigated.

5.7 Description of the Time Segments and Pressure Indices

A total of 502,343 RR, RC and CC intervals have been extracted and a total of 4,456 sets of RR, RC, CC and blood pressure values have been formed from 149 patients (from 8 to 108 points per patient). The mean and standard deviation values (mean ± SD) of the time segments RR, RC, and CC and the ratio RC/RR are reported in **Table 5.1**, where the blood pressure indices as systolic blood pressure (SBP, mmHg), diastolic blood pressure (DBP, mmHg) and mean blood pressure (MBP, mmHg) are also presented. It can be observed that the value of the ratio between RC and RR intervals is of 21.6 ± 3.8 % and the mean value of RR and CC intervals is coincident.

MEASURED HEMODYNAMIC INDICES

Indices	Mean ± SD
RR	959.8 ± 155.2 ms
RC	202.0 ± 20.4 ms
CC	959.8 ± 155.2 ms
RC/RR	21.6 ± 3.8 %
SBP	110.1 ± 23.5 mmHg
DBP	63.9 ± 15.7 mmHg
MBP	83.2 ± 18.5 mmHg

Table 5.1 Mean and standard deviation of measured hemodynamic indices in the sample of patients undergoing surgery. SBP: systolic blood pressure; DBP: diastolic blood pressure; MBP: mean blood pressure

The relationship between pressure indices (systolic, diastolic and mean blood pressure) and time segments (RR, CC and RC intervals) was studied. The ratio RC/RR was also included. **Table 5.2** reports the values of this relationship. The highest correlation was observed between RR intervals (or CC intervals) and the DBP index with ρ = -0.341 (p-value < 0.01) and RR

intervals with the MBP index, ρ = -0.317 (p-value < 0.01). A lower correlation was obtained between CC and SBP, ρ = -0.259 (p-value < 0.01). However, all of these are considered as weak correlations.

Figure 5.3 includes a graphical representation of the relationships between the time segments (RR, CC and RC) with their correlations. **Figure 5.3A** shows that there exists a very strong, positive correlation between RR and CC with ρ = 0.998 (p-value < 0.0005). In order to study the relation between the electrical and mechanical activity of the heart provided by the RR and RC intervals taking into account that the RC interval is in fact a portion of the RR interval the dispersion plot between RR and the ratio RC/RR has been evaluated in **Figure 5.3B**. It proved to be inversely proportional according to Equation (15).

$$\mathrm{RC/RR(\%)} = \mathrm{a} + \mathrm{b/RR} \tag{15}$$

where a = 3.94 (no units); b = 16.47 s, with ρ = 0.662 (p-value < 0.01). RR intervals between 700 and 1000 ms correspond with RC/RR ratios lower than 30%.

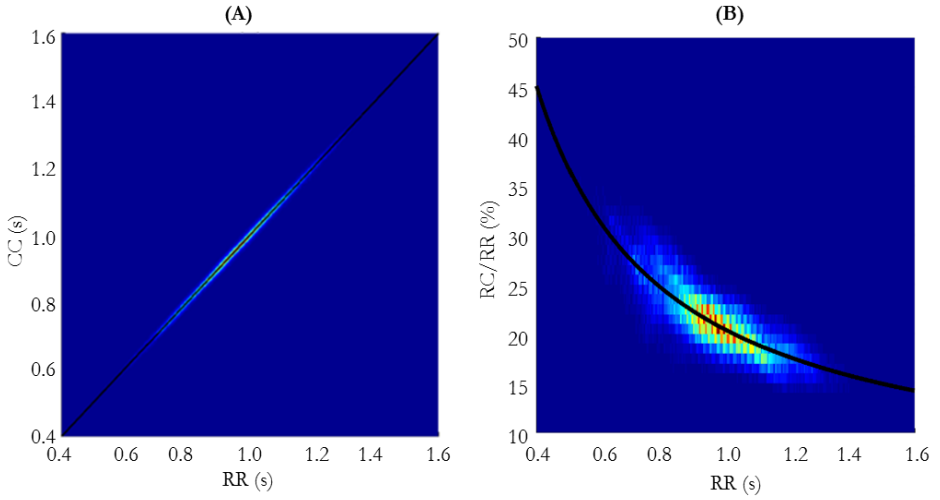

Figure 5.3 Regression plots between RR, RC and CC of patients undergoing surgery. (A) CC (ms) = 0.999·RR (ms) + 0.704, ρ = 0.998, with a significance of p-value < 0.0005; (B) RC/RR (%) = 3.94+16.47/RR, being RR in seconds, ρ = 0.662, with a significance of p-value < 0.01

MEASURED HEMODYNAMIC INDICES

Indices	SBP	DBP	MBP
RR	-0.260	-0.341	-0.317
CC	-0.259	-0.341	-0.316
RC	-0.218	-0.127	-0.179
RC/RR	+0.116	+0.249	+0.195

Table 5.2 Spearman's coefficients between time segments and blood pressure indices. All correlations are statistically significant with p-value < 0.01.

Furthermore, the linear relationships between the current RC with the previous RR or RC intervals, and also between the current RR with the previous RR or RC have also been analyzed. A maximum time lag of 40 beats was considered for this study.

In order to describe these relationships, the decorrelation velocity (Dv) for each pair of measurements was calculated as the negative slope of the linear regression of the Spearman's coefficients once the decrease in ρ is linear and it is measured in percentage decrease per time lag difference. The variation of ρ between RC[n] and RC[n-1] was -17.1%, much higher than the variation presented between RR[n] and RR[n-1] ($\Delta\rho$ = -4.5%) as can be seen in**Table 5.3**. The variation of ρ between RC[n] and RR[n-1] was +0.9% while it was $\Delta\rho$ = +0.6% in the case of RR[n] vs RC[n-1]. In all cases, Dv was very low.

RR AND CC CORRELATION AND DECORRELATION VELOCITY

	$\Delta\rho$	Dv
RR[n] vs RR[n-1]	-4.5%	0.14%
RC[n] vs RC[n-1]	-17.1%	0.12%
RR[n] vs RC[n-1]	+0.6%	0.04%
RC[n] vs RR[n-1]	+0.9%	0.02%

Table 5.3 Variation of Spearman's coefficient ($\Delta\rho$) and decorrelation velocity (Dv), considering n = 502,343 samples

5.8 Effect of Induction of Anesthesia on Time Segments and Blood Pressure Indices

Taking into consideration both the time segments (RR and RC) and the blood pressure values, the t-Student test has shown that the variation in these values before and after LOC is statistically significant (p-value < 0.0005) as

reported in **Table 5.4**. An increase in the value of the RR intervals and in the value of RC intervals (p-value < 0.0005) can be observed. However, the values of the blood pressure indices significantly decreased from after LOC during surgery (p-value < 0.0005). **Figure 5.4** shows the evolution of the relationship between instant RR and RC intervals in a patient undergoing anesthesia. The reduction of RC/RR between before and after LOC can be clearly noted.

CHANGES IN HEMODYNAMIC INDICES WITH ANESTHESIA

	Pre-LOC	Post-LOC	p-value
RR (ms)	872.1 ± 121.7	959.7 ± 142.7	< 0.0005
RC (ms)	186.4 ± 13.6	205.0 ± 15.8	< 0.0005
SBP (mmHg)	135.2 ± 24.4	102.3 ± 21.1	< 0.0005
DBP (mmHg)	78.5 ± 11.3	61.3 ± 11.3	< 0.0005
MBP (mmHg)	102.2 ± 15.8	79.1 ± 16.9	< 0.0005

Table 5.4 Mean ± SD for several measurements before (Pre) and after (Post) loss of consciousness (LOC)

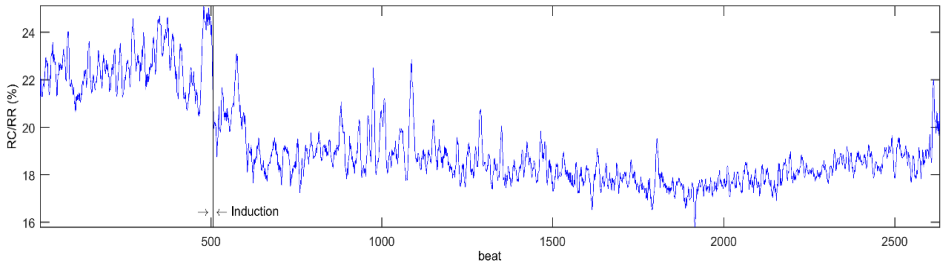

Figure 5.4 RC/RR ratio in a patient undergoing anesthesia. The vertical line marks the instant of LOC

The relationships between the mean of the time segments RR, RC and CC before and after LOC have also been analyzed using 83 available comparisons. The RR intervals presented a higher correlation between before and after LOC (ρ = 0.764, p-value < 0.01) than the correlation RC intervals before and after LOC (ρ = 0.601, p-value < 0.01), as it can be seen in **Table 5.6**. Before LOC, RC intervals were correlated with RR intervals (ρ = 0.427, p-value < 0.0005), also RC and RR intervals were correlated after LOC, (ρ = 0.488, p-value < 0.0005) as seen in **Table 5.5**. However, the RC intervals both before and after LOC are more dependent on the RR values before LOC than those after LOC. Non-significant differences were observed when the influence of age and gender in all analyzed indices was measured.

CORRELATION COEFFICIENTS FOR HEMODYNAMIC INDICES BEFORE AND AFTER LOSS OF CONSCIOUSNESS

Variable A		Variable B		ρ	p-value
RC	Pre-LOC	RR	Pre-LOC	0.427	< 0.0005
			Post-LOC	0.252	0.029
		SBP	Pre-LOC	-0.290	0.039
			Post-LOC	-0.181	n.s.
		DBP	Pre-LOC	-0.093	n.s.
			Post-LOC	-0.181	n.s.
	Post-LOC	RR	Pre-LOC	0.488	< 0.0005
			Post-LOC	0.252	0.021
		SBP	Pre-LOC	-0.206	n.s.
			Post-LOC	-0.452	0.001
		DBP	Pre-LOC	-0.103	n.s.
			Post-LOC	-0.369	0.008
RR	Pre-LOC	SBP	Pre-LOC	-0.290	0.039
			Post-LOC	-0.240	n.s.
		DBP	Pre-LOC	-0.173	n.s.
			Post-LOC	-0.283	0.044
	Post-LOC	SBP	Pre-LOC	-0.229	n.s.
			Post-LOC	-0.270	n.s.
		DBP	Pre-LOC	-0.258	n.s.
			Post-LOC	-0.361	0.009

Table 5.5 Spearman's correlation coefficients between variables A and B before (Pre) and after LOC (Post). n.s.: statistically non-significant

AUTOCORRELATION COEFFICIENTS FOR HEMODYNAMIC INDICES

Pre vs. Post-LOC	ρ	p-value
RR (ms)	0.764	< 0.0005
RC (ms)	0.601	< 0.0005
SBP (mmHg)	0.463	< 0.001
DBP (mmHg)	0.478	< 0.0005

Table 5.6 Spearman's auto-correlation coefficients for RR and RC before (Pre) and after LOC (Post)

Table 5.7 contains the results according to variation responsiveness of the studied indices between pre and post-LOC. If VAR is any of the studied indices in this chapter, the variation responsiveness was defined as ΔVAR =

(VARpost-VARpre)/VARpost. It is observed that an increase of RC intervals with anesthetic drug infusion negatively correlated with a decrease in SBP (ρ = -0.445, p-value = 0.001). In addition, RC and SBP correlate after LOC (ρ = -0.452, p-value = 0.001) as seen in **Table 5.5**. No correlation was found between the increase in RR and the increase in RC (ρ = 0.113, p-value = 0.310).

CORRELATION COEFFICIENTS BETWEEN HEMODYNAMIC INDICES

Variable A	Variable B	ρ	p-value
ΔRR	ΔSBP	-0.200	n.s.
	ΔDBP	-0.051	n.s.
ΔRC	ΔSBP	-0.445	0.001
	ΔDBP	-0.277	0.01

Table 5.7 Spearman's correlation coefficients between variables A and B. n.s.: statistically non-significant

5.9 Discussion of Results

In the present study, the use of a noninvasive method based on an approximation of the pre-ejection period to study the response of induced anesthesia was investigated. In this way, RR, RC, CC cardiac intervals obtained from ECG and ICG signals, and systolic, diastolic and mean blood pressures responses were compared. The use of these signals for any pharmacologic effect related to anesthetic depth detection is attractive: recordings can be obtained entirely noninvasively, rapidly, and easily.

Both RR and CC intervals have been found to be almost identical with a Spearman's coefficient of 0.998 (p-value < 0.01). This coincidence can be used in order to detect artifacts in the ICG and ECG signals. The RC interval correlates in a positive way with both RR and CC, as several studies also showed [133], [137].

Regarding the RC/RR rate, the relationship with the RR interval is relevant. In fact, the RC/RR clearly decreases with the increase of the RR interval. The inversely proportional Equation (15) has a regression coefficient of 0.66 and the behavior shown in **Figure 5.3** is very similar to the relation between the RR interval and the RC/RR ratio found by Hoekstra [133] where exercise stimulus effects were studied. In those studies, highly trained subjects had an RC interval and a RC/RR interval higher than the control group, indicating that the time delay between electrical and mechanical activity was longer in such group. This could eventually lead to sports applications.

The positive linear relationship between the RC and RR intervals demonstrates that with a decrease in the RR interval, the RC is also shortened. The inversely proportional relationship between the RC/RR and RR interval shows that when RR decreases, the RC interval phase decreases less than the total cardiac cycle. This goes in line with the conclusions by Eijnatten [137] when he states that the shortening of the initial systolic time interval with increasing HR in response to an exercise stimulus can be attributed to a shortening of the pre-ejection period in every individual: when the HR increases, the time interval between the R peak and the opening of the aortic valves decreases while the time between the opening of the aortic valves and the C point remains constant. It is important to note that van Lien [138] already concluded that despite the RC interval being an important tool, it should not be used to estimate PEP with only a single regression equation.

The present study also analyzed how the RC interval depends on its previous values, obtaining correlations varying from 0.641 (consecutive beats) to 0.333 (between two beats delayed 8 beats). The dependence between the RC interval and RR also decreased in time but was always lower than such of the RC with itself, as it can be seen in **Table 5.3**.

Our study has also found a negative relationship between the RC interval and blood pressure (systolic, diastolic and mean) but a positive relationship between the RC/RR proportion and blood pressure. Biesheuvel [139] also found a negative relationship between the RC interval and the systolic blood pressure and so did Muehlsteff [140] and Wong [141]. The latter also claimed that PEP had some potential to predict systolic blood pressure. However, it is necessary to highlight the complicated nature of the relationships between HR, BP and PEP. Whitsett [142] conducted a study comparing these measurements in patients with Parkinson's disease using different drugs looking for the mechanisms responsible of varying and control these parameters.

Both RR and RC have shown to decrease after LOC, which is consistent with previous studies [102], [136]. This response was similarly observed in predicting fluid responsiveness after cardiac surgery [136]. In addition, systolic and diastolic pressures presented a statistically decreasing difference. This decrease is compensated by an increase in RR, and as well RC, that is secondary to vagal withdrawal and increased cardiac sympathetic activity [143], [144]. However, it is know that SBP is affected by the pulse pressure and

vascular dimensions [145], whereas the RC is a more direct measure of electromechanical coupling of the heart. The RC interval has shown no relationship to most variables such as age and gender. An increase of RC intervals with anesthetic drug infusion negatively correlated with a decrease in SBP (ρ = -0.445, p-value = 0.001, as can be seen in **Table 5.7**). Also, RC and SBP correlate after induction (ρ = -0.452, p-value = 0.001) as seen in **Table 5.5**.

Some limitations may arise when comparing the results against previous studies found in the literature. Each ICG monitor has different properties concerning the positioning of electrodes and number of electrodes. For instance, in the method used in [133], [139], [146], the four electrodes are completely separated while qCO has two groups of two electrodes which are close to each other. Furthermore, the applied AC currents are different. Also the monitor device in [133], [137], [146] uses 0.3 mA at 64 kHz while the qCO monitor applied an AC current of 0.4 mA at 50 kHz. Finally, the pharmacological effects of the drugs infused in the patients may vary depending on the target concentrations. Therefore, the hemodynamic measurements might also be affected by the different concentrations used in every case. These facts do not reduce the validity of results but should be taken into account when analyzing the values of RC intervals.

5.10 Conclusions

This study has further characterized the relationship between ICG and ECG. Some previous results found in the literature have been validated using a new database and some new results have been reached. The relationship between the different time intervals in ICG and ECG and the blood pressure has been described. According to our analysis, the RC interval could have an important impact in describing the state of a patient and further studies are required to identify further possible applications. Finally, the coincidence of the CC and RR segments are key to develop new artefact detection algorithms and this has been included in a patent developed in this Doctoral Thesis.

.

Chapter 6

Performance of Time-Frequency Distributions for ICG Signals

Abstract

Time-frequency distributions show how the spectral content in a signal changes with time. It is a powerful tool which, however, requires the selection of an appropriate kernel for each type of signal. In order to describe ICG signals, this chapter analyses the performance of several kernels which have been applied to ICG signals. Finally, the proposed kernels are tested for noise resistance and on a clinical database of real ICG signals. The results of this chapter have been accepted for publication in the journal "Medical & Biological Engineering & Computing".

6.1 Introduction

Advanced techniques for the analysis of biomedical signals such as the ICG signals and process automatization techniques are increasingly important for diagnosis. The visual inspection of biomedical signals may be a tedious task and subjective judgements and errors can occur even when skilled interpreters are involved.

In order to improve the calculation of the indices derived from the analysis of impedance cardiography, several authors have exploited the periodic or quasi-periodic behavior of the ICG signals for denoising or for locating their characteristic points [147], [148]. The study of these signals in the frequency domain can shed light on the quasi-periodical behavior of ICG signals and also on ICG features which cannot be directly observed in the time domain. Some features could be related to HRV, for which ECG analysis would be more effective, but other features could be related to the patient's hemodynamic state. However, the ICG behavior in the frequency domain varies with time and, therefore, it is convenient to analyze how the frequency distribution of a biomedical signal changes with time [149].

Time-frequency distributions is a technique which is often used in the case of analyzing electroencephalogram (EEG) [150]–[156], heart rate variability [157]–[162], respiration signals for apnea detection [163], and pathological speech signals [164]–[166], amongst others. There are several different ways to formulate valid TFDs [167] but any application would ideally require high definition in spectral components, no interferences between the spectral components which can cause cross-terms to appear (in order to avoid confusing real components from artifacts or noise), a low computational complexity and some mathematical properties [168]. However, these properties do not normally occur together and the selection of an appropriate TFD depends on the characteristics of the signal to analyze.

When it comes to selecting the best TFD for synthetic signals, several quantitative measurements can be used based on geometrical properties [169], [170], error and entropy properties [156], [171]–[175] of the TFDs. These measurements can be applied when the time-frequency characteristics of real signals are known. Nevertheless, these characteristics are usually unknown in the case of real physiological signals.

In this chapter, in order to test the goodness of TFDs for real biological signals such as the ICG, we propose the usage of synthetic signals modeling the real ICG signals. The TFDs can then be optimized for its usage with real

ICG signals by means of using ICG synthetic signals fulfilling the following requirements: synthetic signals should resemble very much to the original signals from a time and frequency perspectives, and time-frequency parameters should be easily modifiable. To the best of our knowledge, the application of TFDs to ICG signals has not been extensively published.

In order to accomplish these requirements, the synthetic signals explained in Chapter 3 were used to evaluate different TFDs based on geometric criteria. An exemplary signal can be found in **Figure 3.4**. The most common TF distributions available were tested: the Wigner-Ville Distribution (WVD), the Born-Jordan distribution (BJD), the spectrogram, the S-method (SM), the Choi-Williams distribution (CWD), the Zhao-Atlas-Marks distribution (ZAM), the Modified B-Distribution (MBD) and the Extended Modified B-Distribution (EMBD) [167].

The instantaneous frequency of the different spectral components on the TFDs was determined and its errors with the theoretical IFs were measured. The robustness against low signal-to-noise ratios has also been tested. In addition, optimized TFDs were used on synthetic ICG signals derived from patterns of the rest of patients in the ICG database obtained from the Shanghai Study and described in Chapter 3.

6.2 Time-Frequency Distributions

This subsection explains the basic theory of the time-frequency distributions. Concepts such as the analytic associate, the variety of available kernels and the detection of the instantaneous frequency are described.

6.2.1 Analytic Associate

In TFDs, the usage of the analytic associate of a given real signal, rather than the signal itself, is useful for reducing the required sampling rate, and essential for obtaining an unambiguous instantaneous frequency. The analytic associate is obtained via the Hilbert transform:

$$\mathcal{H}\{s(t)\} = \mathcal{F}_{t\leftarrow f}^{-1}\left\{\left(-j\,\mathrm{sgn}(f)\right)\mathcal{F}_{t\leftarrow f}\{s(t)\}\right\} \tag{16}$$

where $\mathcal{F}_{t\leftarrow f}\{\dots\}$ is the Fourier transform.

The detail process to obtain the Hilbert transform of s(t) is as follows:

1. Take the Fourier transform S(f) of s(t).
2. Multiply S(f) by –j for positive, by +j for negative, and by zero for f=0.
3. Take the inverse Fourier transform.

This procedure creates an analytic signal containing no negative frequencies. This does not produce any loss of information in the case of real signals and it introduces two beneficial effects: it halves the total bandwidth and avoid the appearance of interference terms generated by the interaction of positive and negative components in quadratic TFDs which are a consequence of the bilinear nature of the TFD formulation.

6.2.2 TFD Formulation

High-resolution time-frequency analysis is useful for signals which are nonstationary and/or multicomponent. Quadratic TFDs are based on estimating the instantaneous power spectrum of the signal by using a bilinear operator [167]. The Wigner-Ville distribution is the basic quadratic TFD and is defined by taking the Fourier transform of an instantaneous auto-correlation function $\mathrm{K_z}(\mathrm{t},\tau)$.

$$\mathrm{W_z}(\mathrm{t},\mathrm{f}) = \int_{-\infty}^{+\infty} \mathrm{K_z}(\mathrm{t},\tau)\mathrm{e}^{-2\mathrm{j}\pi\mathrm{f}\tau}\mathrm{d}\tau \tag{17}$$

where $\mathrm{K_z}(\mathrm{t},\tau)$ is defined as

$$\mathrm{K_z}(\mathrm{t},\tau) = \mathrm{z}(\mathrm{t}+\tau/2)\mathrm{z}^*(\mathrm{t}-\tau/2) \tag{18}$$

and where $\mathrm{z}(\mathrm{t})$ is the analytic associate of a real signal $\mathrm{s}(\mathrm{t})$ obtained with the Hilbert transform $\mathrm{z}(\mathrm{t}) = \mathrm{s}(\mathrm{t}) + \mathrm{j}\mathcal{H}\{\mathrm{s}(\mathrm{t})\}$ as explained before.

6.2.3 Kernels for TFDs

The WVD provides a high-resolution representation of the signal $\mathrm{x}(\mathrm{t})$ in time and frequency but the presence of cross-terms in multicomponent signals is deleterious for biomedical signal processing. Cross-terms can be reduced by convolving the WVD with a two-dimensional kernel $\gamma(\mathrm{t},\mathrm{f})$ to obtain the general formulation of quadratic TFDs in Equation (19).

$$\rho_{\mathrm{z}}(\mathrm{t},\mathrm{f}) = \gamma(\mathrm{t},\mathrm{f}) \underset{(\mathrm{t},\mathrm{f})}{**} \mathrm{W_z}(\mathrm{t},\mathrm{f}) \tag{19}$$

The two-dimensional kernel $\gamma(t,f)$ reduces cross-terms – the terms created by the interaction of different time-frequency components in a signal – but it also blurs auto-terms – the terms in the TFD which really represent the different time-frequency components in a signal. Therefore, kernels need to be designed to obtain the best tradeoff between minimizing cross-terms and maintaining the auto-terms' resolution.

The general formulation in Equation (21) of the kernels $\gamma(t,f)$ (19) in the time-frequency domain is usually formulated in a so-called ambiguity domain such as $g(\nu,\tau)$, where ν and τ are Doppler and lag, respectively, as indicated in Equation (20). This is because the convolution operation in the time-frequency domain becomes a multiplication in this ambiguity domain, which reduces its complexity.

$$\rho_z(t,f) = \int_{-\infty}^{\infty}\int_{-\infty}^{\infty} g(\nu,\tau)\, A_z(\nu,\tau)\, e^{j2\pi(\nu t - f\tau)} d\nu\, d\tau \tag{20}$$

where $A_z(\nu,\tau)$ is the ambiguity function of the analytic associate $z(t)$ of the real signal $s(t)$. Separable kernels are a special case when $g(\nu,\tau) = G_1(\nu)g_2(\tau)$. If $G_1(\nu) = 1$, the kernel is Doppler independent. If $g_2(\tau) = 1$, the kernel is lag independent. **Table 6.1** shows the TFDs tested along with the corresponding kernels. The spectrogram is calculated using four different windows: rectangular, Hamming, Hanning and Bartlett.

The S-Method is based on the relation of the Short-Time Fourier Transform (STFT) and the WVD: the STFT is a linear operation and does not suffer from any cross-terms [176]. Cross-terms in TFDs appear due to the interaction of the STFTs of different signal components, which can be avoided using a window frequency function $P(\nu) = 0, |\nu| > L_P$. By changing L_P, a gradual transition can be obtained ranging from the spectrogram $(L_P \to 0, P(\nu) = \delta(\nu)/2)$ to the WVD $(L_P \to \text{signal length}, P(\nu) = 1)$. The best choice of L_P would be the value when $P(\nu)$ is wide enough to enable complete integration over the auto-terms, but narrower than the distance between the auto-terms, in order to avoid the cross-terms. Equation (21) describes how the SM is based on the STFT and the window frequency function $P(\nu)$.

$$SM_z(t,f) = 2\int_{-\infty}^{\infty} P(\nu)\, STFT_z(t, f+\nu)\, STFT_z^*(t, f-\nu) d\nu \tag{21}$$

KERNELS FOR TIME-FREQUENCY DISTRIBUTION

TFD	Kernel Type	Kernel $\mathrm{g}(\nu,\tau)$
WVD		1
BJD	Non-separable	$\mathrm{sinc}(2\alpha\nu\tau)$
S-Method	Non-separable	$\mathrm{A_w}(\nu,\tau) \underset{\nu}{*} \mathrm{P}(-\nu/2)$
Spectrogram	Non-separable	$\mathrm{w}(\nu+\tau/2)\,\mathrm{w}(\nu-\tau/2)$
CWD	Non-separable	$\mathrm{e}^{-\nu^2\tau^2/\sigma}$
ZAM	Non-separable	$\mathrm{w}(\tau)\dfrac{a}{2\lvert\tau\rvert}\mathrm{sinc}\left(\dfrac{2\nu\tau}{\mathrm{a}}\right)$
MBD	Lag-independent	$\dfrac{\lvert\Gamma(\beta+\mathrm{j}\pi\nu)\rvert^2}{\Gamma^2(\beta)}$
EMBD	Separable	$\dfrac{\lvert\Gamma(\beta+\mathrm{j}\pi\tau)\rvert^2}{\Gamma^2(\beta)}\dfrac{\lvert\Gamma(\alpha+\mathrm{j}\pi\nu)\rvert^2}{\Gamma^2(\alpha)}$

Table 6.1 Kernels for the TFDs [167] used in this work. The parameters a, α, β and σ and the window w define the kernel shape and are estimated taking into account the characteristics of the signal, where ν and τ are Doppler and lag, respectively

6.2.4 Identification of Instantaneous Frequency

The evaluation of different kernels by using synthetized ICG signals with known time-frequency properties can lead to the most adequate TFD for real ICG signals. To validate this extent, the IF can be calculated in the TFDs with the optimized kernels.

There are several techniques to spot the different IF. One of the approaches used an iterative estimate of the first moment of the spectrogram as the IF in order to also construct a matched spectrogram estimate. This approach is stopped when convergence between two consecutive spectrograms was reached and produces a match spectrogram concentrated along the IF of monocomponent signals [177]. IF estimation from the maxima of the TFDs has a variance and bias highly influenced by the lag window length. Therefore, Stanković and Katkovnik [178], [179] proposed an adaptive algorithm for determining the optimal lag width based on the intersection of upper and lower confidence intervals of the IF estimates for each time instant.

The IF estimation methods of multicomponent signals are highly dependent on the selected TFR and presence of cross-terms which could be mistaken for the IF estimate. A simple approach is to use time-frequency filtering methods to retrieve individual IFs [167]. Other approaches require

extending algorithms for estimation of monocomponent IF to the case of signals with various IF [180].

In general, concrete properties are required for the TFDs when detecting the IF of multicomponent signals: high time-frequency resolution and efficient suppression of cross-terms; direct amplitude estimation for the individual components, and minimum bias of the IF from the true IF laws. TFDs such as the MBD satisfy these requirements and the work by Stanković and Katkovnik in [178], [179] can also be extended for the case of multicomponent signals.

This work proposes an algorithm to search the IF without setting the total number of existing IFs and their approximate frequencies. The steps are as follows:

1. Find the local maximum peaks for every time instant in the TFD higher.
2. Group these peaks so that they form a continuum along time. This is the expected behavior of IF laws since the synthetic TFDs are created as a Fourier series of tones whose frequency varies in a determined manner along time.

It is important to note that the first and last 10% of time of the TFD is not to be taken into consideration in order to detect the IF, since the starting and final instants of the TFD are blurry and can introduce errors in calculations.

6.3 Performance Calculation

Choosing the best kernel for a signal requires a concrete strategy. In some studies, the kernel is selected in a visual way. However, this method is highly unpredictable and biased and therefore quantification methods have been proposed. Since the characteristics of the synthetic ICG signal to analyze are well known, it is possible to quantify which kernel produces the quadratic TFD with characteristics most similar to those of the ICG signal. Boashash and Sucic [169] proposed to measure the difference between the instantaneous frequency $\widehat{IF}(n)$ that a TFD produced and the theoretical instantaneous frequency $IF(n)$. For this purpose, two statistical measures are used in order to quantify these differences: the mean square error (MSE) in

Equation (22) and the percentile root mean square difference (PRD) in Equation (23).

$$\mathrm{MSE} = \frac{\sum_{n=1}^{N}\left[\mathrm{IF}(n) - \widehat{\mathrm{IF}}(n)\right]^2}{(n-1)} \tag{22}$$

$$\mathrm{PRD} = \frac{\sqrt{\sum_{n=1}^{N}\left[\mathrm{IF}(n) - \widehat{\mathrm{IF}}(n)\right]^2}}{\sqrt{\sum_{n=1}^{N}[\mathrm{IF}(n)]^2}} \tag{23}$$

where n is the time instant.

Furthermore, Boashash and Sucic [169], [170], [181] also proposed a method to measure the performance of a TFD with an objective quantitative criterion expressed in Equation (24).

$$P = 1 - \frac{1}{3N}\sum_{n=1}^{N}\left[\frac{A_S(n)}{A_M(n)} + \frac{1}{2}\frac{A_x(n)}{A_M(n)} + \frac{E(n)}{\Delta f(n)}\right] \tag{24}$$

where for a pair of signal components at time n (in the total interval of N time instants), A_M is the average of the components main lobes amplitudes, A_s is the average of the components sidelobes, A_X is the in-between components cross-terms amplitude, E is the average of the components mainlobes bandwidths, and Δf is the frequency separation between the IF components. A low P indicates poor performance while values close to one indicate good performance. Both performance P and the different statistical measures are used to select the best TFD and its parameters.

A new performance P calculation is proposed. It is based on a modification to Equation (24) to take into account that the tones in a synthetized ICG signal will not have the same amplitude. Equation (25) shows the adaptation of the performance for a two-tone synthetized ICG signal.

$$P = 1 - \frac{1}{3N}\sum_{n=1}^{N}\left[\frac{1}{2}\left|\frac{A_{s1}(n)}{A_1(n)}\right| + \frac{1}{2}\left|\frac{A_{s2}(n)}{A_2(n)}\right| + \left|\frac{A_x(n)}{A_1(n) + A_2(n)}\right| - D(n) + 1\right] \tag{25}$$

where, $A_{s1}(n)$ and $A_{s2}(n)$ are the sidelobe amplitudes of tones 1 and 2, $A_1(n)$ and $A_2(n)$ are the tone amplitudes of tones 1 and 2, $A_x(n)$ is the amplitude of the cross-term between both tones, and $D(n)$ is defined in Equation (26).

$$D(n) = (V_1(n)/2 + V_2(n)/2)/(f_2(n) - f_1(n)) \tag{26}$$

where $V_1(n)$ and $V_2(n)$ are the bandwidths, and the instantaneous frequencies of the first and second tones are $f_1(n)$ and $f_2(n)$, respectively.

A new approach has also been used in order to validate the performance of the studied distributions. Taking into account that the WVD of a linear frequency-modulated signal gives an unbiased estimate of the IF of such frequency, the performance of a TFD can also be studied as the likelihood between such TFD and the addition of the WVDs of every single tone in a test signal such as the synthetic ICG signal. This likelihood can be quantified by means of the cross-correlation (CC) between the studied TFD of the synthetized ICG signal, and the addition of the WVDs of every single tone in the synthetized ICG signal.

Finally, the previously mentioned measurements (P, MSE, PRD and CC) have been applied to synthetic ICG signals with and without noise. To test the behavior of the different TFDs, noise tests have been conducted by corrupting the synthetic ICG signals with white noise in signal-to-noise ratios (SNR) decreasing from 20 dB to -5 dB in steps of 1 dB.

According to the literature [167], [182]–[184], the sources of error in the estimation when detecting the IFs by using the TFD maximal positions are the estimate bias, the random deviation of the maxima in the auto-term due to small noise and the large random deviations due to false detection of maximal points outside the auto-terms. In [184], an adaptive IF estimator with a time-varying and data-driven window length is presented and the results are similar to the quality obtained if the IF information was known in advance. The work in [183] shows that the estimator of the polynomial WVD for signals with additive white Gaussian noise can be improved by the adequate selection of the kernel coefficients in the distribution. These works are expanded in [185] and it explains that the crucial parameter is the ratio of auto-term magnitude and the standard deviation of the distribution.

Once the initial synthetic signals have been designed and the optimized TFDs have been selected, these results have been applied to the complete database of 15 patients. Synthetic ICG signals have been designed using ICG patterns extracted from the real ICG signals in every patient. The synthetic ICG signals have been used to test the performance P, cross-correlation, and IF errors for the optimized TFDs.

6.4 Results of TFD Performance for Synthetic ICG Signals

To test the performance of different TFDs, the previous synthetized two-tone ICG signal with a linear frequency variation has been used. The performance has been calculated for each type of TFD kernel with the different characteristic parameters for each type of kernel. For each TFD, the values of the parameters for the best performance have been obtained through an optimization procedure to find the combination of parameters for which the performance P is maximal according to Equation (25).

The results of the optimization process are plotted in **Figure 6.1** and the specifications are included in **Table 6.2**. **Figure 6.1** shows how the performance changes for each type of TFD depending on the values of several parameters such as window length w for the spectrogram (**Figure 6.1A**), σ for the CWD (**Figure 6.1B**), a for the ZAM distribution (**Figure 6.1C**), β for the MBD (**Figure 6.1D**), L_P and window length w for the SM for all window types (**Figure 6.1E**), and α and β for the EMBD (**Figure 6.1F**). As the figure shows, the highest P performances are obtained for the spectrograms (except when the rectangular window is used) and the EMBD, and the lowest P performances are for the CWD. The S-Method provides results very similar to those offered by the spectrogram for all cases although slightly inferior. The blank spaces in **Figure 6.1E** represent the combination of values for which the performance calculation algorithm has not been able to identify the IF tones. **Table 6.2** presents the values for these parameters for the best-performance distributions, where the maximum performances are for the spectrogram when the Hamming (P = 0.781), Hanning and Bartlett (P = 0.780 for both windows) windows are used, and for the EMBD (P = 0.778).

In addition, the CC correlation between the studied TFDs of the synthetized ICG real-based signal, and the addition of the WVDs of the two single tone in the synthetized ICG signal is included in the same table. The CC correlation is best for the MBD and worst for some of the spectrograms and S-Method reaching even less than 0.5. Finally, a comparison between the expected and the resulting instantaneous frequencies has been performed using Equations (22) and (23), whose results are also included in **Table 6.2**.

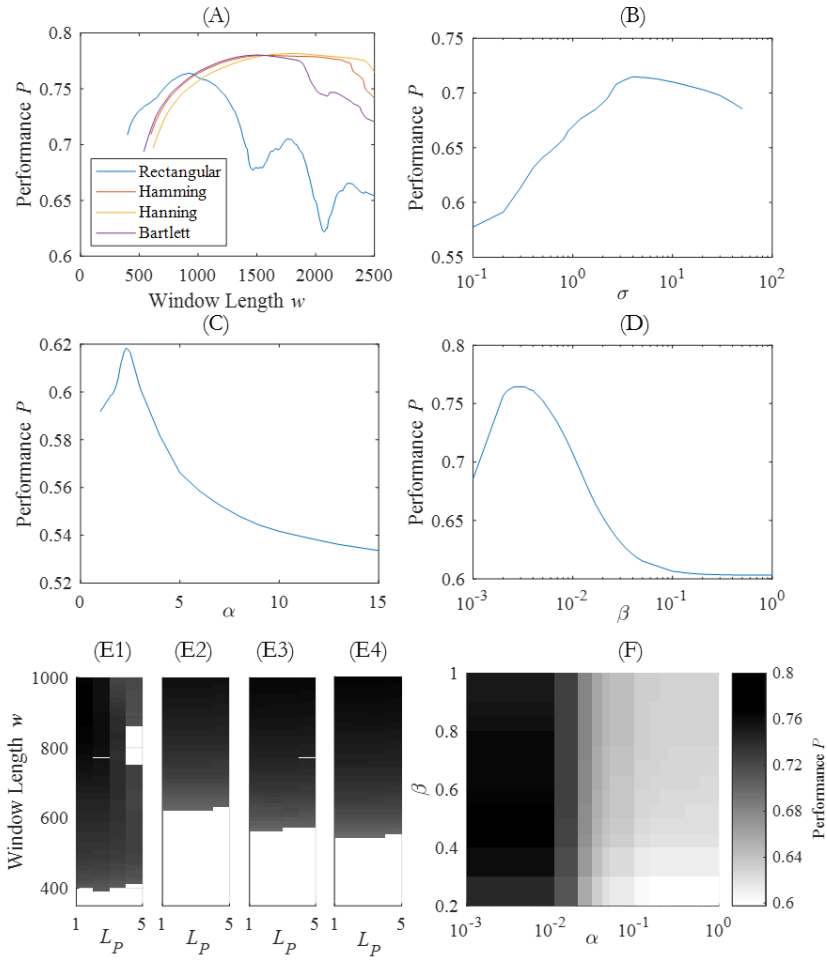

Figure 6.1 TFD Performance optimization results: the resulting performance *P* of the spectrograms (A), ZAM distribution (B), CWD (C), MBD (D), SM (E) and EMBD (F) for varying parameters is plotted. The SM is optimized for a rectangular (E1), Hamming (E2), Hanning (E3) and Bartlett (E4) windows

Table 6.3 includes all the numerical values of the characteristic points for the central slice, corresponding to the instant 5s: the sidelobe amplitudes of tones 1 and 2 (A_{s1} and A_{s2}), the tone amplitudes of tones 1 and 2 (A_1 and A_2), the amplitude of the cross-term between both tones A_x, the bandwidths, V_1 and V_2 and the instantaneous frequencies of the first and second tones are $f_1(n)$ and $f_2(n)$, respectively. **Figure 6.2A** contains the plot of the time slice at t = 5s with the characteristic points used to calculate the performance P according to Equation (25) for the spectrogram with a Barlett window

(column 1), CWD (column 2), and EMBD (column 3). **Figure 6.2B** shows the resulting TFDs for the kernels spectrogram with Hanning window, CWD and EMBD, and **Figure 6.2C** shows the theoretical IFs and the resulting IFs located on the TFDs. Some features of these kernels can be easily seen in **Figure 6.2**. The non-negativity characteristic of the spectrogram provides zero-valued cross-term and secondary term amplitudes easy to locate.

TFD OPTIMIZATION RESULTS

				MSE (%)		PRD (%)	
	Parameters	P	CC	IF_1	IF_2	IF_1	IF_2
WVD		0.698	-	0.013	0.029	0.952	0.727
BJD		0.698	0.557	0.117	0.286	2.907	2.274
SM	Rect. w=929, L_P=1	0.769	0.588	0.000	0.000	1.092	0.902
	Ham. w=999, L_P=2	0.764	0.492	0.000	0.000	0.763	0.409
	Han. w=999, L_P=1	0.757	0.471	0.000	0.000	0.775	0.424
	Bart. w=999, L_P=2	0.765	0.498	0.000	0.000	0.804	0.461
Spect.	Rect. w=919	0.764	0.506	0.019	0.060	1.176	1.043
	Ham. w=1569	0.781	0.495	0.048	0.139	1.870	1.584
	Han. w=1779	0.780	0.501	0.020	0.066	1.194	1.092
	Bart. w=999	0.780	0.448	0.009	0.021	0.795	0.617
CWD	σ=4.12	0.715	0.600	0.077	0.149	2.359	1.638
ZAM	a=2.3	0.618	0.603	0.023	0.086	1.290	1.248
MBD	β=0.0026	0.765	0.686	0.072	0.107	2.272	1.392
EMBD	α=0.002, β=0.988	0.778	0.577	0.077	0.114	2.362	1.432

Table 6.2 Best-performance P and correlation CC of TFDs with their parameter values; MSE and PRD for the resulting and theoretical IFs for the first (IF_1) and second (IF_2) tones.

In **Figure 6.2**, the frequency width of the IFs is larger for the spectrogram than for other kernels such as the EMBD and the CWD. It is also noticeable how the spectrogram and the EMBD kernels provide a softer TFD with fewer cross-terms between the two frequencies, which are prominent in the case of the CWD. A large number of undulations appear in addition to the two main ridges which represent the sum of the two frequency-modulated signals. In the theoretical WVD, the cross-terms are located midway between the interacting components, oscillate proportionally to the distance between the auto-terms and in a direction orthogonal to the line connecting these auto-terms.

Quadratic TFDs in which cross-terms are attenuated relative to the auto-terms in often named a reduced-interference distribution and it is a well-

studied topic in the literature [167], [186]. In general, since auto-terms in the (t,f) plane are usually smooth, their corresponding version in the (ν, τ) plane tends to be concentrated in the origin. On the contrary, **Figure 6.2B** shows that cross-terms tend to be oscillatory in the (t,f) plane which lead to terms far away from the origin in the (ν, τ) plane. Choosing the right kernel in the (ν, τ) plane can filter out information far from the center and can thus attenuate cross-terms. In addition, the starting and final seconds of the TFD seem fuzzier than the rest of the TFD. This fact is to be taken into account when calculating the IFs of the distributions.

SLICE OPTIMIZATION RESULTS

		Characteristic Points in TF Slice							
	$P_{t=5s}$	A_{s1}	IF_1	V_1	A_x	V_2	IF_2	A_2	A_{s2}
WVD	0.668	-0.229	1.19	39.4	0.358	46.4	2.35	0.420	-0.076
BJD	0.522	-0.172	1.22	198.4	0.074	247.8	2.29	0.374	-0.103
SM Rect.	0.770	0.028	1.19	56.1	-0.003	59.7	2.35	0.384	0.022
SM Ham.	0.763	0.000	1.19	75.8	0.000	82.7	2.35	0.395	0.000
SM Han.	0.754	0.000	1.19	85.6	0.000	87.5	2.35	0.420	0.000
SM Bart.	0.767	0.000	1.19	74.5	0.000	80.0	2.35	0.408	0.000
Spect.Rect.	0.757	0.022	1.19	166.0	0.030	178.8	2.38	0.346	0.059
Spect. Ham.	0.776	0.000	1.19	159.3	0.000	286.9	2.35	0.263	0.000
Spect. Han.	0.781	0.000	1.19	174.6	0.000	217.3	2.35	0.333	0.000
Spect. Bart.	0.768	0.000	1.19	228.0	0.000	246.9	2.35	0.402	0.000
CWD	0.716	-0.072	1.19	176.1	0.094	243.8	2.35	0.338	-0.051
ZAM	0.605	-0.456	1.19	86.1	-0.109	109.3	2.35	0.285	-0.167
MBD	0.753	-0.014	1.19	65.00	0.173	83.0	2.35	0.244	0.016
EMBD	0.782	0.004	1.19	119.6	0.037	177.0	2.35	0.267	-0.003

Table 6.3 Slice optimization results: amplitudes $A_{s_1}, A_x, A_2, A_{s2}$, frequency bands V_1 and V_2 (in mHz) of the IF_1 and IF_2 (in Hz) for the calculation of the instant performance $P_{t=5s}$. Amplitudes A_1 are always the unit

Finally, the analysis of the robustness of the different kernels in relation to the signal-to-noise ratio (SNR) is summarized in **Figure 6.3**. Noise in TFDs has been previous analyzed in depth and the bias and variance for different types of additive and multiplicative noise have been determined [187]. The study of the additive Gaussian noise influence on TFDs has led to the design of robust TF distribution using the robust minimax Huber M-estimates [186], [188].

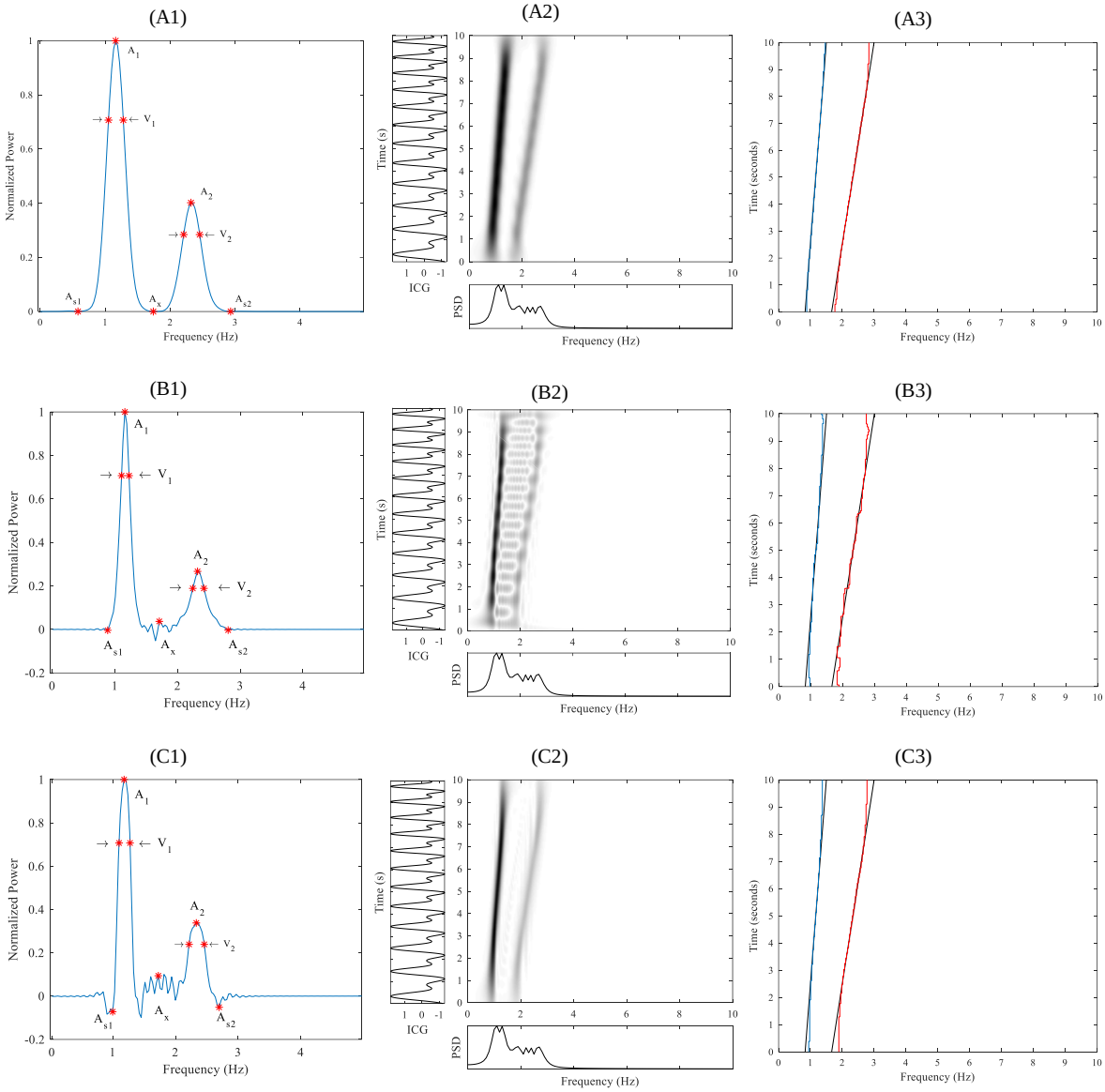

Figure 6.2 Optimized TFD Results: (1) A time slice at t = 5s of the TFD with the characteristics points $A_{s_1}, A_x, A_2, A_{s2}$, and frequency bands V_1 and V_2 in red of the two tones and the cross tones for the calculation of the performance P. (2) The resulting optimized TFD. (3) Location of the resulting first (in blue) and second (in red) IFs, IF_1 and IF_2 against the theoretical results (in black), for each type of analyzed TFD: Spectrogram with a Bartlett window (A), CWD (B), and EMBD (C)

In this study, all kernels except ZAM, CWD and BJD present similar performance P between 0.76 and 0.78 when SNR = 20 dB and such performance decreases at a similar speed for all cases until reaching a performance P between 0.73 and 0.76 when SNR = -5 dB although the case at which the P decreases is slightly higher for EMBD and MBD **Figure 6.3A** and **B**. Regarding **Figure 6.3C**, the MSE values are not similar for all kernels and vary from 0.01 to 0.12 for SNR = 20 dB and from 0.02 to 0.22 for SNR = -5 dB. However, the evolution of the decrease in MSE with decreasing SNR is similar for all kernels and the MSE values remain constant after 10 dB.

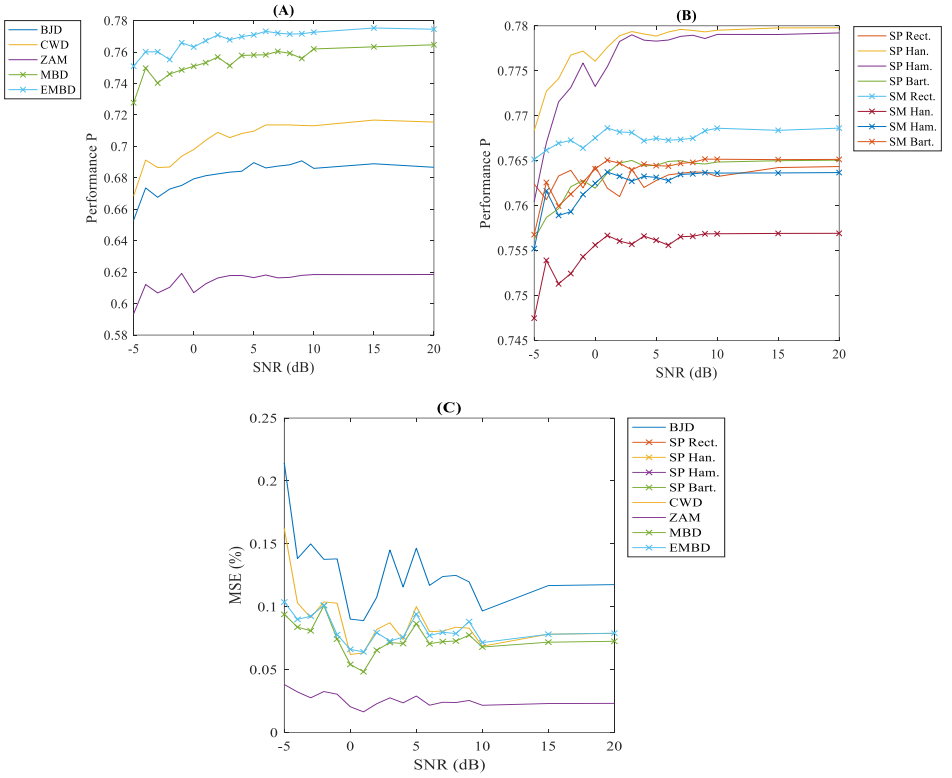

Figure 6.3 TFD results to noise tests. (A) and (B) show the performance P of several TFDs to different SNR rates; (C) shows the root mean square error (MSE) in the detection of the first instantaneous frequency

6.5 Results of TFD Performance for Real ICG Signals

According to the procedure of creation of the synthetic ICG signals explained in Chapter 3, the most frequent pattern has been extracted from every patient with a correlation coefficient of th = 0.85 between ICG beats, as in the case for the synthetized ICG signal described in Chapter 3. All patterns are included in **Figure 6.4**. These patterns have been used to create synthetic ICG signals with known linear time-frequency variations in order to calculate their TFDs with different kernels and test their performances. **Table 6.4** includes the performance P, cross-correlation performance CC, MSE of IF, and PRD of IF. The performance at a single slice in the central time $P_{t=5s}$ has also been included. The performance P is maximum for the spectrogram when either Hanning or Hamming windows are used, and for the EMBD, while the WVD and the ZAM offer the worst results. However, the WVD also offers some of the best results for the location of the instantaneous frequency since MSE and PRD are minimum.

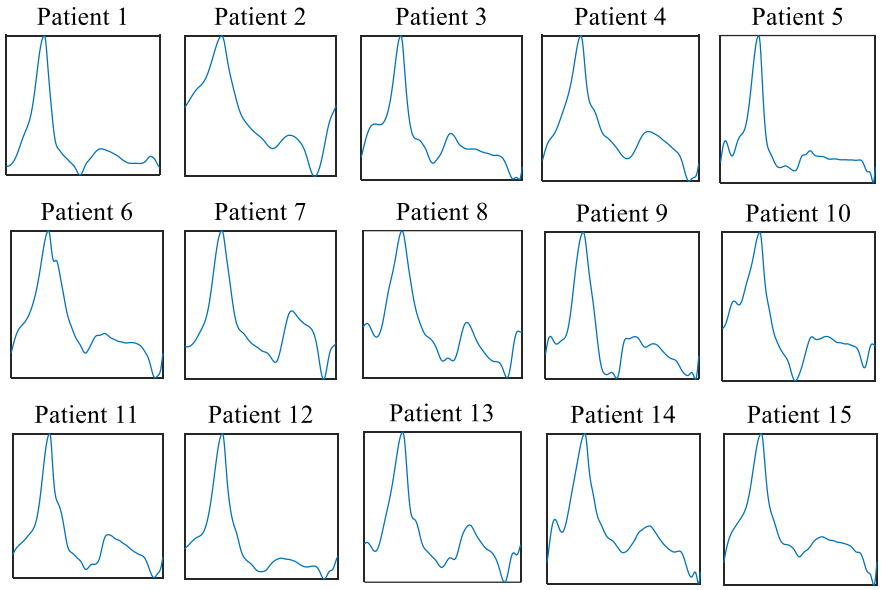

Figure 6.4 Main ICG pattern for all patients in the data base. X-axis is normalized time and y-axis is normalized ICG. Patterns have been normalized to the same time duration in the x axes

TFD RESULTS FOR THE COMPLETE DATABASE

	Performance			MSE (%)		PRD (%)	
	P	$P_{t=5s}$	CC	IF_1	IF_2	IF_1	IF_2
WVD	0.601 ± 0.011	0.610 ± 0.010	-	0.016 ± 0.003	0.017 ± 0.006	1.081 ± 0.099	0.542 ± 0.087
BJD	0.686 ± 0.003	0.684 ± 0.004	0.603 ± 0.027	0.095 ± 0.005	0.196 ± 0.041	2.617 ± 0.074	1.871 ± 0.181
SM Rect.	0.762 ± 0.002	0.762 ± 0.002	0.577 ± 0.004	0.027 ± 0.009	0.030 ± 0.017	1.380 ± 0.230	0.715 ± 0.168
SM Ham.	0.780 ± 0.000	0.780 ± 0.000	0.465 ± 0.002	0.008 ± 0.000	0.009 ± 0.001	0.781 ± 0.013	0.396 ± 0.016
SM Han.	0.780 ± 0.000	0.780 ± 0.001	0.483 ± 0.003	0.008 ± 0.000	0.009 ± 0.000	0.785 ± 0.014	0.415 ± 0.006
SM Bart.	0.765 ± 0.000	0.765 ± 0.000	0.490 ± 0.003	0.009 ± 0.001	0.011 ± 0.001	0.824 ± 0.033	0.446 ± 0.012
Spec. Rect.	0.710 ± 0.003	0.714 ± 0.004	0.657 ± 0.005	0.022 ± 0.009	0.046 ± 0.018	1.244 ± 0.236	0.896 ± 0.153
Spec. Ham.	0.614 ± 0.003	0.620 ± 0.001	0.634 ± 0.014	0.038 ± 0.003	0.145 ± 0.006	1.655 ± 0.067	1.616 ± 0.035
Spec. Han.	0.764 ± 0.002	0.767 ± 0.002	0.621 ± 0.028	0.013 ± 0.001	0.068 ± 0.003	0.964 ± 0.043	1.103 ± 0.028
Spec. Bart.	0.776 ± 0.001	0.782 ± 0.001	0.587 ± 0.003	0.010 ± 0.001	0.020 ± 0.001	0.832 ± 0.037	0.596 ± 0.023
CWD	0.766 ± 0.001	0.767 ± 0.001	0.640 ± 0.027	0.064 ± 0.003	0.121 ± 0.017	2.145 ± 0.052	1.476 ± 0.097
ZAM	0.764 ± 0.000	0.765 ± 0.000	0.692 ± 0.030	0.018 ± 0.001	0.073 ± 0.014	1.154 ± 0.039	1.143 ± 0.102
MBD	0.757 ± 0.000	0.758 ± 0.000	0.798 ± 0.031	0.048 ± 0.003	0.107 ± 0.006	1.863 ± 0.065	1.387 ± 0.042
EMBD	0.765 ± 0.000	0.766 ± 0.000	0.699 ± 0.026	0.054 ± 0.005	0.116 ± 0.005	1.978 ± 0.099	1.445 ± 0.031

Table 6.4 Average of performance measures: performance P, performance $P_{t=5s}$ of the time slice at t = 5s, and cross-correlation performance CC, and instantaneous frequency in MSE and PRD errors for all cases using several TFDs

6.6 Discussion of Results

In this work, the primary key finding is the proposal of an innovative methodology for choosing a suitable TFD for a real biomedical signal. On the one hand, several authors have previously addressed the complexity of selecting kernels for TFDs by using visual methods or characteristics of the signals to analyze [167]. Nevertheless, this work takes into account that such characteristics are often partially unknown and the proposed methodology has been applied to ICG signals. On the other hand, some authors have used wavelet transforms for denoising ICG signals and for locating the characteristics points of the ICG curve [147], [148], [189], [190]. The main difference is that wavelet analysis uses some given analyzing wavelets (such as the so-called Mexican hat or Morlet wavelets) while the objective of this work was to investigate the overall time-frequency content of the ICG signals.

Taking the most characteristic pattern of a patient's ICG signal, a signal with a pre-defined linearly-variant time-frequency characteristics has been constructed and used to calculate the goodness of several TFDs. The

goodness has been calculated using the geometrical characteristics of the TFD according to formulation adapted from prior publications [169], [170], [181], and the MSE and the PRD between the expected and the theoretical IFs of the TFDs. Furthermore, a new performance measure has been introduced taking into account the fact that the IF detected in a WVD for a frequency linearly-variant signal is the best approximation of the instantaneous frequency of the signal.

The second key finding relates to the different TFDs analyzed. In our results, neither the spectrogram nor the newer MBD and EMBD are clearly superior to each other. According to the results in **Table 6.2**, the kernels with largest P performances are the EMBD and the spectrogram when used with Hamming, Hanning or Bartlett windows ($P \in [0.768,0.782]$). The S-Method provides results similar to the spectrogram although slightly inferior. The MBD and the spectrogram with the rectangular windows also present high P performance but it should be noted that the spectrogram is more sensitive to the length of the rectangular window than to the length of the rest of windows, as it can be seen in **Figure 6.1A**. **Figure 6.1F** also shows that the EMBD provides a stable performance P for a large variety of values for the parameters α and β.

The correlation CC is best for MBD and worst for the spectrogram and the S-Method. However, this seems not to define the ability to detect the IF as predicted since the best MSE for both IF_1 and IF_2 is for the spectrogram with the Bartlett window. The MSE and PRD for the WVD is also very low, which is in line with the theoretical description of the WVD having a perfect IF when the signal tone changes in a linear fashion.

Regarding the performance P in the central time slice of the TFDs, the best performance P is such of EMBD followed by the Hanning spectrogram. It is important to note that there are almost no secondary and cross lobes. Nevertheless, the thinnest tone is detected by MBD (after the WVD for the reasons explained above). In fact, the spectrogram provides the widest tones irrespective of the window in use. This is detrimental for the location of instant tones such as the ones used in this work. Moreover, the cross-correlation performance CC has offered poor results for the spectrograms while the resulting CC is best for MBD.

In general, the robustness of the spectrogram is related to the lack of undesirable artifacts present in other TFDs since the non-linearity is introduced in the final step of the spectrogram computation (when taking the squared magnitude). Nonetheless, the spectrogram does not satisfy the

instantaneous frequency criterion of the quadratic class of TFDs and hence it does not allow the exact extraction of the signal IFs from its dominant peaks [167].

Regarding the noise test, the results have shown that no TFD stands out for its resistance to noise. The performance of the spectrogram seems to decrease at a slower speed than the performance of other TFDs with similar performance such as MBD and EMBD. The root mean square errors between the expected IF and the calculated IF follow the same pattern for all TFDs and start to rise for SNR less than 2 dB. Finally, the tests on the whole database of patients confirm the above-mentioned discussion, since the results have been very similar, according to **Table 6.4**.

6.7 Conclusions

The technique explained in this chapter sheds light on the methodological aspects of the selection of the best kernel to analyze ICG signals and the robustness of these kernels to noise has been analyzed. In the case of the ICG signals, some traditional kernels such as BJD could be discarded due to the results of this work. As a result, the final choice of the kernel to use must follow a thorough evaluation of the measurements described in this chapter and the user's experience on the type of signals to analyze.

This page is intentionally left blank.

Chapter 7

TFD-Derived Features for ICG Signals during Anesthesia

Abstract

This chapter explores different TFD-derived features in order to characterize the time-frequency content of ICG signals with a reduced number of information. The features derived by using several kernels are also compared and discriminant analyses were conducted to differentiate between the TFD features from the ICG signals registered before and after the patient's loss of consciousness during anesthesia procedures. The results of this chapter have been accepted for publication in the journal "Methods of Information in Medicine".

7.1 Introduction

TFDs offer a useful insight in the time-frequency content of signals but they contain considerably large amounts of data. Therefore, features are to be extracted from the TFDs in order to improve its characterization. Several authors have proposed different features applied to TFD in order to describe non-stationary signals or to locate events based on the signal entropy, energy concentration measures or singular values decomposition [191]–[194]. This chapter compiles some of those features in order to apply them to the ICG signals from the CMA database explained in Chapter 3. Several kernels are also compared and discriminant analyses were conducted to differentiate between the TFD features from the ICG signals registered before and after the patient's loss of consciousness during anesthesia procedures, as it has been also presented in Chapter 4 and 5.

7.2 TFD-Derived Features

The time variation in the spectrum of a signal can be characterized with several features extracted from its TFDs. This paper analyses a collection of TFD measures based on singular value decomposition (SVD), entropy characteristics, energy concentration and time and frequency characteristics of the ICG signal.

7.2.1 SVD-Based TFD-Derived Features

A TFD of NxM (time samples x frequency samples) can be decomposed using its singular values in the form $\rho = \mathrm{USV}^{\mathrm{H}}$, where U is an NxN matrix, S is an NxM diagonal matrix with positive real singular values σ_{i}, and V^{H} is an MxM real unitary matrix. Following previous works [191]–[193], in this investigation several features are extracted from the singular values σ_{i} of the TFD, such as: $\mathrm{F}_{\mathrm{SVD1}}$, the maximum σ_{i} ; $\mathrm{F}_{\mathrm{SVD2}}$, standard deviation of σ_{i} ; and $\mathrm{F}_{\mathrm{SVD3}}$, the number of non-zero σ_{i} .

7.2.2 Entropy-Based TFD-Derived Features

The concept of Shannon Entropy [195] has been applied to both the design of new TFDs with minimum entropy [194] and the quantification of TFD complexity in TFDs. If the TFD is interpreted as a quasi-probability distribution, a highly-concentrated TFD with a small number of components has a lower entropy than a signal with a large number of components. The TFD complexity (TFCM) in Equation (27) uses both SVD and Shannon entropy concepts and it represents the magnitude and the number of the non-

zero singular values of the TFD [191], [192]. It is a useful feature as their magnitudes have a strong relationship with the information content in the TFD.

$$\mathrm{TFCM} = -\sum_{i=1}^{N} \bar{\sigma}_i \log \bar{\sigma}_i , \qquad \bar{\sigma}_i > 0 \tag{27}$$

where $\bar{\sigma}_i$ are the N normalized singular values, i.e.: $\bar{\sigma}_i = \sigma_i / \sum_{i=1}^{N} \sigma_i$.

If the entropy of a TFD is to be calculated without using its singular values, the Time-Frequency Rényi entropy (TFRE) in Equation (28) is used in substitution of the Shannon entropy [196]. The latter cannot be used for the majority of TFDs as these are not non-negative. TFRE is a statistical tool sensitive to the number of signal components, their time duration and bandwidth, and their amplitude ratios.

$$\mathrm{TFRE}_q = \frac{1}{1-q} \log_2 \sum_{n=1}^{N} \sum_{m=1}^{M} \rho^q[n,m] , q > 2 \tag{28}$$

The TFRE for odd values of q causes zero-mean cross-terms to diminish due to the summation operation. Thus, the TFRE cannot discriminate a high-resolution TFD with significantly reduced cross-terms from a high-resolution TFD without any suppression of cross-terms. The TFD normalized Rényi entropy (TFNRE) in Equation (29) solves this issue so that cross-terms have an overall effect of reducing the TFNRE.

$$\mathrm{TFNRE}_q = -\frac{1}{2} \log_2 \sum_{n=1}^{N} \sum_{m=1}^{M} \left[\frac{\rho[n,m]}{\sum_{n=1}^{N} \sum_{m=1}^{M} |\rho[n,m]|} \right]^q + \log_2 \delta_t \delta_f \tag{29}$$

where δ_t and δ_f are the time and frequency sampling steps, respectively. Baranjiuk et al. [197], [198] analyzed the influence of the parameter q when calculating both TFRE and TFNRE and concluded that non-integer orders are yield complex values and so appeared of limited utility. In this study, a large range of q values (q = {3, 4, …, 14, 15, 18, 21, 24, 27, 30, 35, 40, 45, 50}) have been selected for TFRE and TFNRE in order to analyze its influence.

7.2.3 Extended Time-Domain TFD Features

In order to use statistical time-domain features, such as mean and variance, the one-dimensional time-domain moments have been replaced with

the corresponding two-dimensional TF characteristics according to [199]. **Table 7.1** includes all extended time-domain features.

TIME-FREQUENCY EXTENSION OF TIME-DOMAIN FEATURES

Feature	TF Formulation	
TFD Mean	$\mathrm{m_{TF}} = \frac{1}{\mathrm{NM}} \sum_{\mathrm{n=1}}^{\mathrm{N}} \sum_{\mathrm{m=1}}^{\mathrm{M}} \rho[\mathrm{n,m}]$	(30)
TFD Variance	$\sigma_{\mathrm{TF}}^2 = \frac{1}{\mathrm{NM}} \sum_{\mathrm{n=1}}^{\mathrm{N}} \sum_{\mathrm{m=1}}^{\mathrm{M}} (\rho[\mathrm{n,m}] - \mathrm{m_{TF}})^2$	(31)
TFD Skewness	$\gamma_{\mathrm{TF}} = \frac{1}{(\mathrm{NM}-1)\sigma_{\mathrm{TF}}^3} \sum_{\mathrm{n=1}}^{\mathrm{N}} \sum_{\mathrm{m=1}}^{\mathrm{M}} (\rho[\mathrm{n,m}] - \mathrm{m_{TF}})^3$	(32)
TFD Kurtosis	$\mathrm{k_{TF}} = \frac{1}{(\mathrm{NM}-1)\sigma_{\mathrm{TF}}^4} \sum_{\mathrm{n=1}}^{\mathrm{N}} \sum_{\mathrm{m=1}}^{\mathrm{M}} (\rho[\mathrm{n,m}] - \mathrm{m_{TF}})^4$	(33)
TFD Coef. of variation	$\mathrm{c_{TF}} = \sigma_{\mathrm{TF}} / \mathrm{m_{TF}}$	(34)

Table 7.1 Time-frequency extension of time-domain features

7.2.4 Extended Frequency-Domain TFD Features

The energy concentration measure (ECOME) determines the concentration of the dominant component at each location in the TF domain. Signals with TFD distributed in the TF plane will have a larger ECOME, while concentrated TFDs will have a smaller ECOME.

$$\mathrm{ECOME} = \left(\sum_{\mathrm{n=1}}^{\mathrm{N}} \sum_{\mathrm{m=1}}^{\mathrm{M}} |\rho[\mathrm{n,m}]|^{\frac{1}{\mathrm{r}}} \right)^{\mathrm{r}}, \mathrm{r} > 1 \tag{35}$$

Sub-band energy-based features represent the energy of the ICG signal in different frequency sub-bands. To the best of the authors' knowledge, no previous studies have been published regarding the spectral content of the ICG signals. Therefore, the frequency plane of the TFDs has been divided by visual inspection and by using pairs of logarithmically spaced values. In total, 138 frequency bands have been analyzed and their corresponding features have been calculated using Equation (36).

$$\mathrm{F_{Band_i}} = \sum_{\mathrm{n=1}}^{\mathrm{N}} \sum_{\mathrm{m=M_{i0}}}^{\mathrm{M_{i1}}} \rho[\mathrm{n,m}], \mathrm{i} = 1 \ldots 138 \tag{36}$$

where $\mathrm{M_{i0}}$ and $\mathrm{M_{i1}}$ delimit the starting and end frequencies of the i-th band.

7.3 Selected Features and Statistical Analysis

For the work in this chapter, several TFD kernels have been used: the spectrogram with Hanning window, the Choi-Williams Distribution (CWD), the Zhao-Atlas-Marks distribution (ZAM), the Modified B-Distribution (MBD) and the Extended Modified B-Distribution (EMBD). Their parameters have been selected by using the synthetic signals explained in Chapter 3 and using the methodology presented in Chapter 6. The details of the kernels are included in **Table 6.2**.

In order to characterize signals corresponding to the segment previous to LOC and that after LOC, a range of features were selected in our study. These features are listed in **Table 7.2**.

SELECTED TIME-FREQUENCY FEATURES

Class	Feature Name	Formulation
SVD-based	Maximum SV	F_{SVD1}
	SV Standard Deviation	F_{SVD2}
	SV Range	F_{SVD3}
Entropy-based	TF Complexity	$TFCM$
	TF Rényi Entropy	$TFRE_q$
	TF Normalized Rényi Entropy	$TFNRE_q$
Extended time-domain	Mean	m_{TF}
	Variance	σ^2_{TF}
	Kurtosis	k_{TF}
	Skewness	γ_{TF}
	Coefficient of variation	c_{TF}
Concentration-based	Energy Concentration	$ECOME$
Sub-bands energy-based	Energy in i-th band	$F_{Band_i}, i = 1 \dots 138$

Table 7.2 Selected features to distinguish between pre-LOC and post-LOC ICG segments. All features are n.u.

Quantitative data are presented as mean ± standard deviation and qualitative data as frequency (percentage). A non-parametric test, the Wilcoxon signed-rank test, was used to investigate whether the analyzed features changed after induction of anesthesia.

Features that satisfy this condition were considered for building a linear discriminant function. The leave-one-out method was used for validation. Sensitivity (Sen), specificity (Spe) and the area under the curve (AUC) of the receiver operating characteristic (ROC) curve were calculated to assess the

ability of the studied features to predict the occurrence of LOC. Sen represents the proportion of pre-LOC ICG segments correctly classified as pre-LOC and Spe represents the proportion of post-LOC ICG segments correctly classified as post-LOC.

Grouped sensitivities and specificities are presented as mean [95% confidence interval (CI)]. In the classification, the cut-off values are always the main of the centroids of the groups. Predicted membership is calculated by first producing a discriminant score for each case using a linear discriminant function. Then cases are classified in a concrete group depending on whether their discriminant score is smaller or larger than the cut-off value. Relationship between time-frequency derived indices and patient characteristics was assessed using Pearson's coefficient of correlation (ρ). Significance level was always set at p-value<0.05.

7.4 Results of TFD-Derived Features

After isolating ten-second segments from before and after LOC, TFDs were calculated with different kernels and, then, the features were extracted and analyzed. **Figure 7.1** displays an example of a case analyzed using an EMBD. **Figure 7.1A** shows the pre-LOC TFD and **Figure 7.1B** shows the post-LOC TFD. The main differences between the two states are the content below 1Hz and the instantaneous frequencies, which seem to be lower in **Figure 7.1B**. The subsequent results aim to show tables and figures how the several TFD-derived features reported in **Table 7.2** are related to the patient's state.

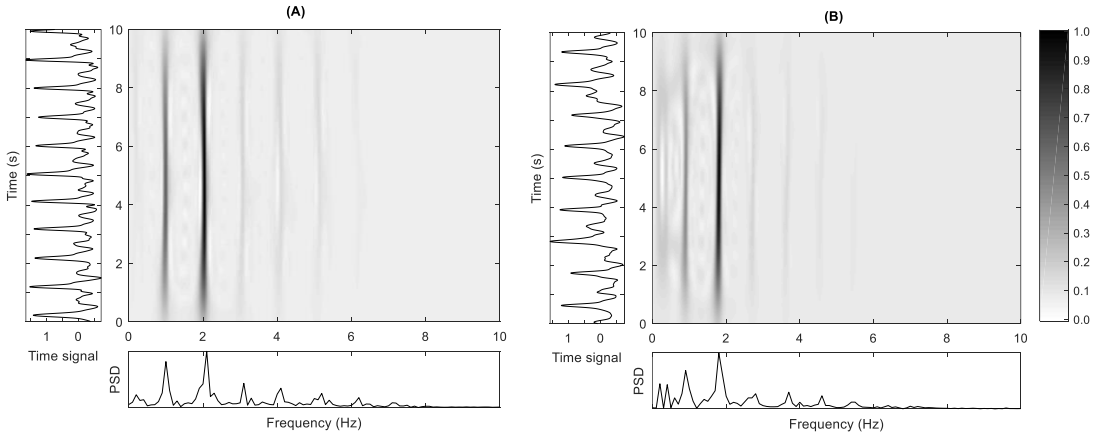

Figure 7.1 EMBD of an ICG segment before LOC (A) and after LOC (B)

7.4.1 SVD-based TFD-derived Features

SVD-based TFD features change from before to after LOC in a statistically significant manner in the case of F_{SVD1}, F_{SVD2} and F_{SVD3} values. **Table 7.3** shows the average values for these features for all the TFD kernels. It can be seen that the defined SVD features are higher before LOC than after LOC. These results have been obtained with values of Sen, Spe and AUC very similar for all kernels and all SVD-based TFD features. In this way, over the different kernels used, Sen(%) is 76.4 [1.1] for F_{SVD1}, 78.0 [0.6] for F_{SVD2} and 65.0 [3.2] for F_{SVD3}. In addition, Spe(%) is 49.2 [0.4] for F_{SVD1}, 51.0 [0.4] for F_{SVD2} and 57.0 [2.5] for F_{SVD3}; AUC is 0.69 [0.01] for F_{SVD1}, 0.70 [0.00] for F_{SVD2} and 0.65 [0.01] for F_{SVD3}. The best SVD-based TFD feature is F_{SVD3} calculated with an EMBD kernel, which presents an AUC = 0.63, Sen = 67.7% and Spe = 60.3%.

SVD-BASED TFD FEATURES

	F_{SVD1}		F_{SVD2}		F_{SVD3}	
	pre-LOC	post-LOC	pre-LOC	post-LOC	pre-LOC	post-LOC
CWD	$(4.0 \pm 3.0)\cdot10^{4}$	$(2.4 \pm 1.6)\cdot10^{4}$	$(9.8 \pm 7.1)\cdot10^{2}$	$(5.6 \pm 3.7)\cdot10^{2}$	$(8.1 \pm 1.4)\cdot10^{1}$	$(7.4 \pm 1.3)\cdot10^{1}$
MBD	$(1.5 \pm 1.1)\cdot10^{5}$	$(9.2 \pm 6.4)\cdot10^{4}$	$(3.6 \pm 2.6)\cdot10^{3}$	$(2.0 \pm 1.4)\cdot10^{3}$	$(1.3 \pm 0.1)\cdot10^{2}$	$(1.2 \pm 0.2)\cdot10^{2}$
EMBD	$(1.4 \pm 1.1)\cdot10^{7}$	$(8.4 \pm 5.8)\cdot10^{6}$	$(3.2 \pm 2.3)\cdot10^{5}$	$(1.8 \pm 1.2)\cdot10^{5}$	$(2.4 \pm 0.6)\cdot10^{2}$*	$(2.1 \pm 0.5)\cdot10^{2}$
Spec. (Han.)	$(1.5 \pm 1.1)\cdot10^{7}$	$(8.3 \pm 5.6)\cdot10^{6}$	$(3.1 \pm 2.3)\cdot10^{5}$	$(1.7 \pm 1.1)\cdot10^{5}$	$(1.0 \pm 0.1)\cdot10^{2}$	$(9.7 \pm 1.2)\cdot10^{1}$
ZAM	$(6.3 \pm 4.7)\cdot10^{6}$	$(3.8 \pm 2.7)\cdot10^{6}$	$(1.6 \pm 1.2)\cdot10^{5}$	$(9.1 \pm 6.0)\cdot10^{4}$	$(5.4 \pm 1.9)\cdot10^{2}$	$(4.6 \pm 1.4)\cdot10^{2}$

Table 7.3 Mean and standard deviation of the SVD-based TFD features. All changes between pre-LOC and post-LOC are statistically significant. * indicates that Sen > 60%, Spe > 60% and AUC > 60%.

7.4.2 Entropy-based TFD-derived Features

Regarding the entropy-based TF features, several results have been obtained. The TFCM presents statistically significant differences between pre-LOC and post-LOC for all kernels (see **Figure 7.2**). In average for all kernels, Sen(%) is 65.4 [4.5], Spe(%) is 51.6 [1.6] and AUC is 0.62 [0.03]. The complexity of the TFD responses is greater during pre-LOC than during post-LOC.

$TFRE_q$ always shows statistically significant differences between pre-LOC and post-LOC for all kernels and for all q values. Furthermore, Sen, Spe and AUC are similar for all q values as seen in **Figure 7.3** and also for all

kernels as **Table 7.4** shows. **Figure 7.3A** shows the $\mathbf{TFRE_q}$ for an exemplary kernel such as the EMBD for all the different q values. $\mathbf{TFRE_q}$ emphasizes high probabilities when q > 1. This figures shows how the values converge as the q increases and the values are always higher for the pre-LOC signals than for the post-LOC signals.

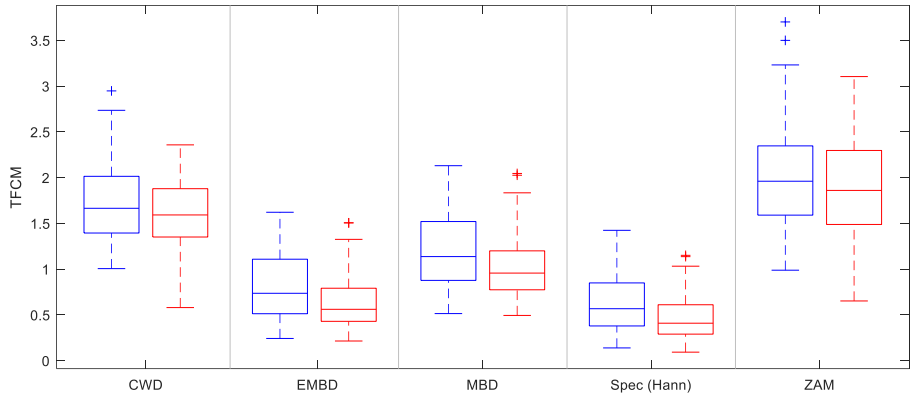

Figure 7.2 TFCM values for different kernels before (blue) and after (red) LOC. All changes are statistically significant

AREA UNDER THE CURVE FOR TIME-FREQUENCY RÉNYI ENTROPY

	Sen(%)	Spe(%)	AUC	pre-LOC $\mathbf{TFRE_{50}}$	post-LOC $\mathbf{TFRE_{50}}$
CWD	61.52 [0.16]	68.90 [0.24]	0.69 [0.00]	-9.26 ± 1.18	-8.51 ± 1.13
MBD	61.07 [0.19]	67.19 [0.48]	0.69 [0.00]	-11.38 ± 1.25	-10.59 ± 1.21
EMBD	63.01 [0.09]	69.33 [0.27]	0.71 [0.00]	-17.64 ± 1.24	-16.77 ± 1.20
Spec. (Han)	62.29 [0.36]	69.92 [0.21]	0.72 [0.00]	-17.15 ± 1.23	-16.22 ± 1.13
ZAM	62.44 [0.27]	69.41 [0.46]	0.70 [0.01]	-16.73 ± 1.22	-15.91 ± 1.15

Table 7.4 Values for Time-Frequency Rényi Entropy: Mean [95% CI] of area under the curve (AUC) of the receiving operating curve (ROC), sensitivity (Sen) and specificity (Spe) of the $\mathbf{TFRE_q}$ feature for all the studied distributions and all q values. $\mathbf{TFRE_{50}}$ values for before and after LOC have also been included

TFNRE also shows statistically significant differences between pre and post-LOC for all q values in the case of the spectrogram and in the case of the EMBD for q ≥ 6. Compared to the TFRE values, the normalization has decreased the AUC below 0.6 in all cases and Sen and Spe are below 60%. **Figure 7.3B** also shows the TFNRE for an exemplary kernel such as the EMBD for all the different q values.

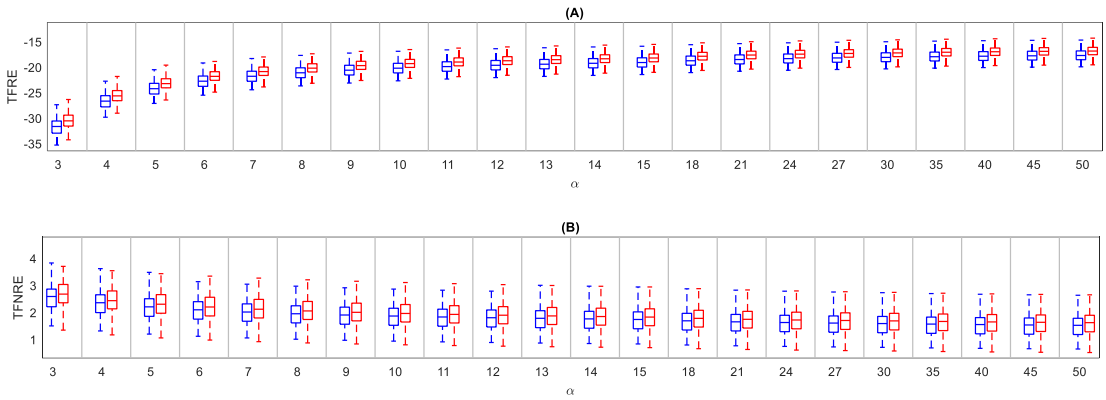

Figure 7.3 Pre (blue) and post-LOC (red) median values for TFRE (A) and TFNRE (B) for the EMBD. Changes between pre-LOC and post-LOC values are always statistically significant (p-value<0.05)

7.4.3 Extended Time-Domain TFD-derived Features

The time-extended TF features show statistically significant differences between the pre-LOC and post-LOC values of $\mathrm{m_{TF}}$ and σ^2_{TF}, for all TFD kernels. In addition, there are also statistically significant differences in the case of $\mathrm{k_{TF}}$ for all TFD kernels except for the CWD and in the case of the γ_{TF} for all TFD kernels except for CWD and ZAM. The difference between the pre-LOC and post-LOC values of $\mathrm{c_{TF}}$ is only statistically significant for the spectrogram. For all TFD kernels, the AUC for these features is 0.70 for $\mathrm{m_{TF}}$ and σ^2_{TF}, and between 0.51 and 0.63 for $\mathrm{k_{TF}}$, γ_{TF} and $\mathrm{c_{TF}}$. Spe is always lower than 60% (between 38.2 and 54.2) for all time-extended TF features and for all kernels but Sen(%) is in average 75.5 [0.3] for $\mathrm{m_{TF}}$ and 85.8 [0.3] for σ^2_{TF}. **Table 7.5** shows that all the time-extended TF features decrease after LOC for the spectrogram. This also occurs for the rest of kernels.

EXTENDED TIME-DOMAIN TFD-DERIVED FEATURES

	pre-LOC	post-LOC
$\mathrm{m_{TF}}$	486.5 ± 340.5	275.0 ± 168.4
σ^2_{TF}	(3.6 ± 5.3)·10^7	(1.0 ± 1.5)·10^7
$\mathrm{k_{TF}}$	16.1 ± 2.8	15.0 ± 2.4
γ_{TF}	319.0 ± 100.9	278.0 ± 87.1
$\mathrm{c_{TF}}$	9.8 ± 1.5	9.5 ± 1.3

Table 7.5 Time-extended TF features of the ICG signals before and after LOC using the spectrogram kernel with a Hanning window. All changes are statistically significant. Features have arbitrary units.

7.4.5 Energy Concentration

ECOME values for all TFD kernels before and after LOC are plotted in **Figure 7.4** and these are higher after LOC than before it. All changes have proven to be statistically significant. In average, Sen(%) is 75.3 [2.1], Spe(%) is 51.6 [1.7] and AUC is 0.72 for all kernels.

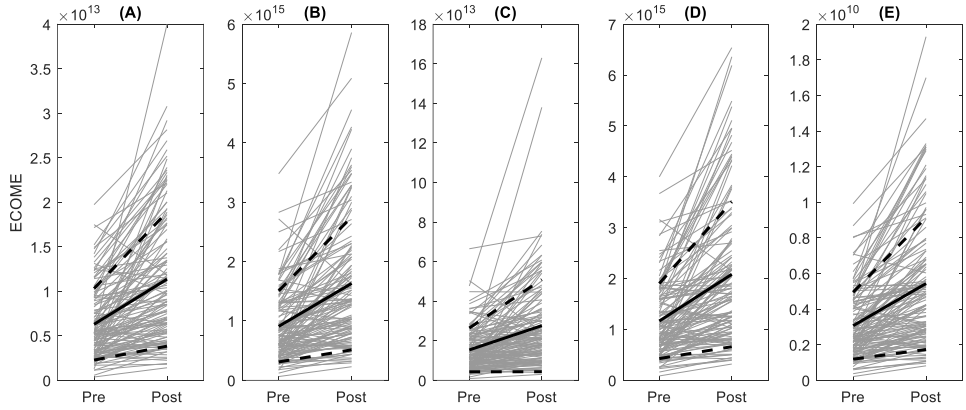

Figure 7.4 Pre and post-LOC ECOME values for the CWD (A), the EMBD (B), the MBD (C), the spectrogram with a Hamming window (D) and the ZAM distribution (E). Changes between pre and post LOC values are always statistically significant (p-value<0.05)

7.4.6 Sub-Bands Energy-based Features

The spectrum of the TFDs has been divided into 138 different frequency bands. The MBD and the ZAM distribution are the ones with the largest number of statistically significant frequency bands, with 114 and 116, respectively. The rest of kernels provide less significant bands: EMBD with 106 bands, CWD with 100 band and the spectrogram with a Hanning window with 91 bands. The spectral content of the TFD bands is always greater before LOC than after LOC. AUC is in almost all cases above 0.6 but both Sen and Spe are not larger than 60% at the same time. **Figure 7.5** shows how the energy in some of the frequency bands changes between before and after LOC. Moreover, this figure also shows how most energy is concentrated between 1 and 4 Hz. The very low frequency from 0 to 0.05 Hz is also prominent, due to the non-zero signal mean.

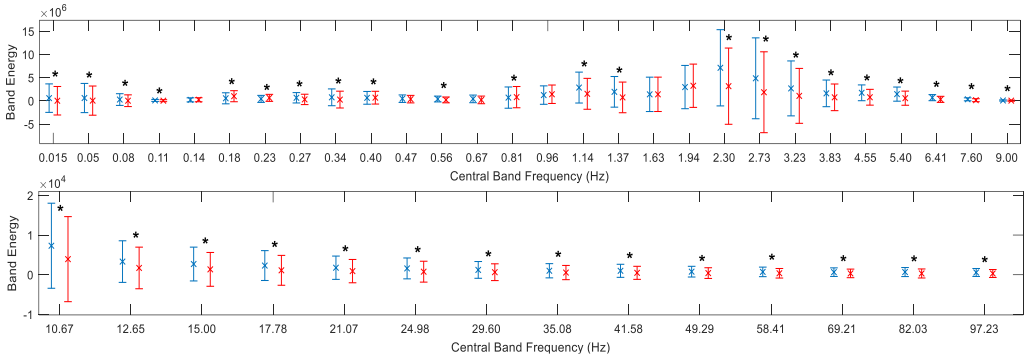

Figure 7.5 Mean and standard deviation of the energy of some bands for the pre-LOC (blue) and post-LOC (red) periods. The kernel used for this figure is the MBD. * indicates that the change is statistically significant (p-value<0.05)

7.5 Discussion of Results

TFDs have been analyzed using five different kernels and information has been extracted using several features based on SVD decomposition, entropy, extended time-domain, concentration and sub-bands energy. All features decreased after LOC. The EMBD kernel offered the largest quantity of features with statistically significant differences with 156 features. There were found 129 features for CWD, 129 for MBD, 147 for the spectrogram and 146 for ZAM distribution. As it can be seen in **Table 7.3**, **Table 7.4**, and **Table 7.5**, after EMBD kernels such as the spectrogram and the ZAM distribution also offer a large amount of significant features but ZAM usually introduces more cross-terms than other distributions.

The robustness of the spectrogram is generally related to the lack of undesirable artifacts present in other TFDs since the non-linearity is introduced in the final step of the spectrogram computation. Nonetheless, the spectrogram does not satisfy the instantaneous frequency criterion of the quadratic class of TFDs and hence it does not allow the exact extraction of the signal IFs from its dominant peaks.

Among all the features which have been analyzed, TFRE is the most successful. For all kernel types and for any q value, TFRE values decrease after the loss of consciousness and both their sensitivity and specificity are always above 60%. Moreover, the AUC is always above 0.6. The increase in the TFRE is theoretically related to the decrease of predictability or the increase of disorder. From a biological point of view, this would imply that

the ICG signals are more deterministic after LOC, which could be related to the mechanical ventilation of the patient during anesthesia. Regarding the sub-bands energy-based features, these show that most of the ICG energy is concentrated between 1 and 4 Hz, since their values are higher than in the rest of frequency band. Nevertheless, sensitivity and specificity of the features should be improved in the future for such features to be adequate for clinical applications.

Our study presents some limitations which must be considered. The pharmacological effects of the drugs infused in the patients may induce different depth of anesthesia states depending on the target concentrations. This is especially true when analyzing signals after LOC. This fact does not reduce the validity of results but should be taken into account especially in future works for which information from depth-of-anesthesia monitors should be included.

7.6 Conclusions

In conclusion, this chapter presents a collection of various features which can be obtained from TFDs. Different kernel TFDs have been calculated and their results have been compared. When analyzing signals representing different anesthetic states, the TF Rényi entropy is the most prominent feature. Regarding the various kernels which have been analyzed, the EMBD is the most successful for the extraction of features showing statistically significant differences in different anesthesia points.

Chapter 8

TFDs and Recurrence Plots for ICG Signals during Anesthesia

Abstract

This chapter extends the work in the previous chapter by analyzing the behavior of features derived from the TFDs during anesthesia. In addition, features from Recurrent Plots – a methodology to analyze periodicities in non-stationary signals – are also included in the analysis. Relationships between all the presented features with hemodynamic parameters and depth of anesthesia are calculated. Finally, several prediction models for CO and depth-of-anesthesia state are discussed.

8.1 Introduction

In the previous chapters, an analysis of TFDs for ICG signals has been presented and some results regarding TFD-derived features have also been analyzed. Nevertheless, the study in Chapter 7 has only considered two different patient states: consciousness and unconsciousness. Therefore, the study presented in the present chapter completes the previous analyses by including complete surgery procedures.

The main objective is to analyze the changes in TFD-derived features in ICG signals during the whole surgeries. This chapter first describes the relationship between TFD-derived features and the depth of anesthesia. It also describes the relationships between TFD-derived features and the hemodynamic state of the patient, defined by the HR, CO, SV, and blood pressure. Finally, the relationship between TFD-derived features and heart rate variability indices described in Chapter 4 is also analyzed. Furthermore, features extracted from recurrence plots of ICG signals are also studied along with TFD-derived features. As a secondary objective, several system such as classification trees and adaptive neuro-fuzzy inference systems (ANFIS) are designed to predict cardiac output and depth of anesthesia by using TFD-derived features.

8.2 Recurrence Plots Features

The Recurrence Plot (RP) graphically displays distance correlations and non-stationarity in time series. No mathematical assumptions regarding the system generating the time series are required and thus this tool is suitable for the analysis of physiological signals such as the ICG [200].

RPs are calculated using an embedding dimension m, a time delay t and a threshold value ε. First, the time series to analyze is embedded to a high-dimensional space with the time-delay embedding technique and a trajectory matrix is obtained [201], [202]. The trajectory matrix X for a time series s_i of length N will be as Equation (37).

$$X = \begin{bmatrix} x_1 \\ x_2 \\ \vdots \\ x_M \end{bmatrix} = \begin{bmatrix} s_1 & s_{1+t} & \cdots & s_{1-(m-1)t} \\ s_2 & s_{2+t} & \cdots & s_{2-(m-1)t} \\ \vdots & \vdots & \ddots & \vdots \\ s_{N-(m-1)t} & s_{N-(m-2)t} & \cdots & s_N \end{bmatrix} \tag{37}$$

Each of the $M = N - t(m-1)$ row vectors x_j in the matrix represents an m-dimensional trajectory point in the reconstructed state-space. The RP of

a signal can be obtained with the state-space reconstruction. The RP is an MxM matrix whose elements can be calculated using Equation (38).

$$R_{i,j} = \Theta\left(\varepsilon - \left\|x_i - x_j\right\|\right) \quad i,j = 1,2,\dots,M \tag{38}$$

where Θ is the Heaviside function and the $\|\cdot\|$ is the Euclidean norm, defined in Equation (39) and Equation (40), respectively. This means that if the distance between x_i and x_j is less than a threshold ε, then $R_{i,j} = 1$.

$$\Theta(z) = \begin{cases} 0, & z \leq 0 \\ 1, & z > 0 \end{cases} \tag{39}$$

$$\forall z = \{z_1, \dots, z_M\}, \qquad \|z\| = \sqrt{|z_1^2| + \cdots + |z_M^2|} \tag{40}$$

The RPs are quantified with the recurrence rate RR_{rec} (percentage of recurrence points in a RP, which corresponds to the correlation sum), the determinism DET (the percentage of recurrence points which form diagonal lines), the entropy ENTR (the Shannon entropy of the probability distribution of the line lengths) and the average diagonal line length L. The more periodic a signal is, the higher RR_{rec} is. It reflects the longest duration of a stable interaction and the average duration of these interactions. DET offers information about the duration of a stable interaction. In our study, ℓ_{min} is 2 samples. Finally, the more different the length of the diagonals are, the more complex the deterministic structure of the RP is and the larger the ENTR value is.

In **Table 8.1**, these measures are explained. In addition, P(ℓ) is the number of diagonal structures whose length is ℓ and p(ℓ) is the probability density of the diagonal structure whose length is ℓ and it is defined as P(ℓ)/sum(P(ℓ)). Finally, ℓ_{min} is a threshold for the minimum length of a line.

Recurrence Plot Features		
RR_{rec}	$\frac{1}{M^2}\sum_{i,j}^{M} R_{i,j}$	(41)
DET	$\frac{\sum_{\ell=\ell_{min}}^{M} \ell P(\ell)}{\sum_{i,j}^{M} R_{i,j}}$	(42)
ENTR	$-\sum_{\ell=\ell_{min}}^{M} p(\ell) \ln p(\ell)$	(43)
L	$\frac{\sum_{\ell=\ell_{min}}^{M} \ell P(\ell)}{\sum_{\ell=\ell_{min}}^{M} P(\ell)}$	(44)

Table 8.1 Features derived from Recurrence Plots

8.3 TFD-Derived Features

For this study of the time-frequency characteristics of the ICG signals, a spectrogram with a rectangular window was constructed for every second of signal. In Chapter 7, spectrograms showed a considerable performance and its Fourier Transform implementation is simple. This was accomplished by using the last 10 seconds of available signal. ICG signal segments for which the associated Signal Quality Index (SQI) was decreasing were discarded. SQI is given by the qCO monitor and it reflects the quality of the signal. All signal segments with an increasing SQI were accepted. TFD-Derived features from Chapter 7 were calculated for those spectrograms: extended time-domain TFD features (mean m_{TF}, variance σ_{TF}^2, skewness γ_{TF}, kurtosis k_{TF}, coefficient of variation c_{TF}), extended frequency-domain TFD features (ECOME), and entropy-based TFD-derived features (Rényi Entropy $TFRE_q$ and normalized Rényi Entropy $TFNRE_q$). Rényi entropies were calculated with q = 3 since the literature research [196]–[198]and results in Chapter 7 showed that this parameter provides efficient results. Furthermore, three additional extended frequency-domain TFD features are calculated [203]:

- TF flux: provides an assessment of the rate of signal energy in the TF domain.

$$\mathcal{FL}_{(\ell,m)} = \sum_{n=1}^{N-\ell}\sum_{k=1}^{M-q} |\rho_z[n+1, k+q] - \rho_z[n,k]| \quad (45)$$

where $\rho_z[n,k]$ is the discretization of the NxM TFD, and ℓ and q determine the direction along which the rate of change of the signal energy is estimated. Three TF flux directions are calculated: the time axis using $(\ell = 0, q = 1)$, the frequency axis using $(\ell = 1, q = 0)$, and the diagonal axis $(\ell = 1, q = 1)$.

- TF flatness: is defined as the ratio of the geometric mean of a TFD divided by its arithmetic mean. It is a useful tool to classify signals whose energy is concentrated in the time-frequency plane from signals whose energy is spread in this same domain.

$$\mathcal{SF} = MN \frac{\prod_{n=1}^{N}\prod_{k=1}^{M}|\rho_z[n,k]|^{\frac{1}{MN}}}{\sum_{n=1}^{N}\sum_{k=1}^{M}\rho_z[n,k]} \tag{46}$$

- Minkowski distance: is a distance measure, which is not sensitive to small values in the TFD. Signals with power distributed over the whole time-frequency plane will have a larger M_2.

$$M_2 = \left(\sum_{n=1}^{N}\sum_{k=1}^{M}|\rho_z[n,k]|^{\frac{1}{2}}\right)^2 \tag{47}$$

The TFD total energy E_{tot}, the five first Instantaneous Frequencies $IF_i, i = 1 \dots 5$, its energies $E_i, i = 1 \dots 5$, and the decay of such energies were also calculated.

8.4 Statistical Analysis

Recurrence Plots are calculated varying the embedding dimension m={2, 3, 4, 5, 6}, the time delay t={1, 33, 62} and a threshold value ε={0.3, 0.5, 0.7}. The first objective of this Chapter was to choose the best combination of parameters t, m and ε to enhance the difference between RPs of ICG signals taken from before and after LOC. Therefore, mean and average of the RP-derived features from before and after LOC were calculated and a discriminant analysis was conducted. The final selection was made based on the best specificity Spe(%), sensitivity Sen(%), and area under the ROC (AUC). A total of 131 patients from the CMA database explained in Chapter 3 were analyzed for selecting the best combination of RP parameters.

As explained in Chapter 2, the index of depth of anesthesia qCON was divided into four different patient states: awakeness (qCON > 80), sedation (qCON $\in$ [60, 80]), general anesthesia (qCON $\in$ [40, 60]) and deep anesthesia (qCON < 40). The probability of prediction of the patient states P_k has been calculated for all TFD-derived and RP-derived features. In this case, both TFD-derived and RP-derived features have been calculated for every second of signal using the last 10 seconds of available signal. The prediction probability P_k has been explained in Chapter 2. Correlations between all TFD-derived and RP-derived features with HRV indices, blood pressure, CO, SV and depth-of-anesthesia index qCON have also been calculated.

In addition, decision trees have been trained to predict the patient state (awakeness, sedation, general anesthesia, and deep anesthesia) by using several TFD-derived features and RP-derived features. Finally, adaptive neuro-fuzzy inference systems (ANFIS) were also trained to predict cardiac output. Decision trees are a type of training systems useful to predict categorical variables (such as the patient's anesthetic state). ANFIS are useful to model a continuous output variable when one or more continuous input variables are available.

8.5 Selection of RP Parameters

An initial RP was calculated as t = 1 sample, m = 3, ε = 0.5. **Figure 8.1A** and **Figure 8.1B** show the trajectory matrix of a pre-LOC ICG signal and a post-LOC ICG signal, respectively. Using the m-dimensional trajectory matrix and Equations (37) and (38), the RPs can be constructed. **Figure 8.2A** shows the RP before the LOC and **Figure 8.2B** shows the RP after LOC. **Figure 8.2C** and **Figure 8.2D** show the recurrence plot with no threshold ε.

Table 8.2 and **Figure 8.3** show the results of the four features extracted from the previous RPs. All RP-derived features show statistically significant difference in the two cases studied (before and after LOC). Sen and AUC are especially high for DET while Spe is higher for L than the rest of features. Both the plots and the table show how all RP-derived features increase after LOC. In general, ENTR is the best parameter in AUC, Spe and Sen.

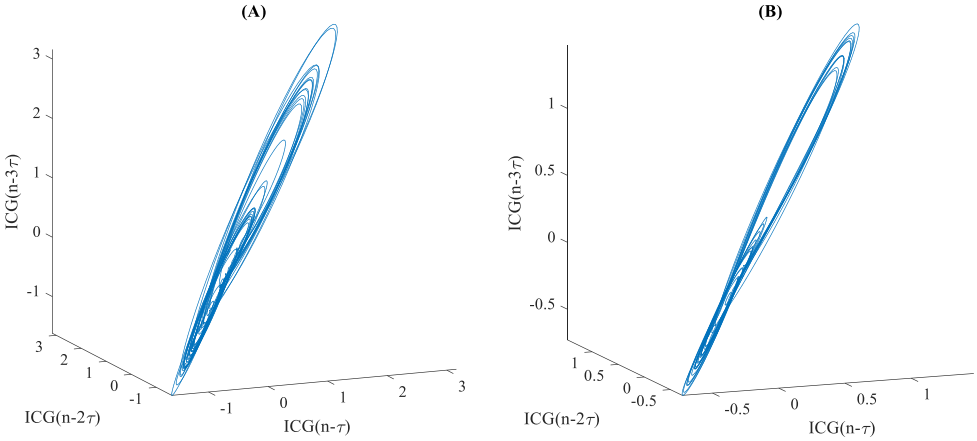

Figure 8.1 Three-dimensional trajectory matrix of a pre-LOC (A) and post-LOC (B) ICG signals. ICG(n-t), ICG(n-2t) and ICG(n-3t) are delayed versions of the ICG signal with m=3 and t=1

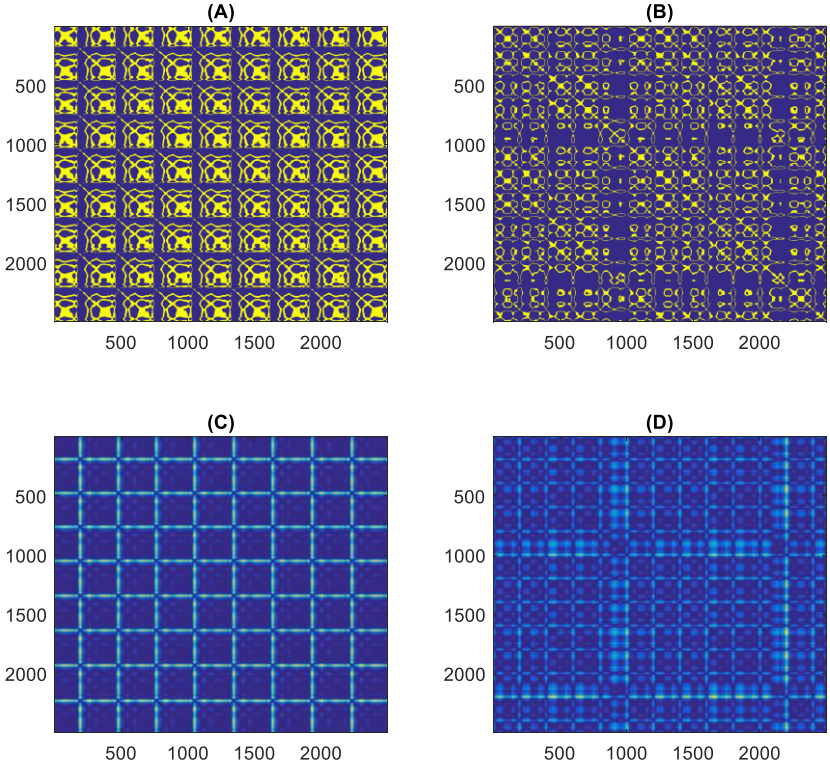

Figure 8.2 Recurrence plots with m=3 and t=1 samples above a threshold $\varepsilon = 0.5$ before (A) and after LOC (B) and recurrence plots with no threshold before (C) and after LOC (D)

DESCRIPTION OF RP-DERIVED FEATURES

	Both	Pre-LOC	Post-LOC	AUC	Sen	Spe
RR_{rec}	0.206 ± 0.036	0.201 ± 0.034	0.212 ± 0.037	0.605	50%	66%
DET	0.997 ± 0.003	0.996 ± 0.004	0.998 ± 0.002	0.718	84%	53%
ENTR	3.120 ± 0.293	3.010 ± 0.289	3.230 ± 0.255	0.716	70%	63%
L	11.6 ± 2.9	10.7 ± 2.5	12.6 ± 2.9	0.700	59%	69%

Table 8.2 Mean, standard deviation and discriminant analysis of the RP-derived features with t = 1 samples, m = 3, and ε = 0.5. All differences have p-value < 0.05, rejecting the hypothesis that the distribution of the difference of the paired values of before and after LOC of a feature comes from a zero-median distribution

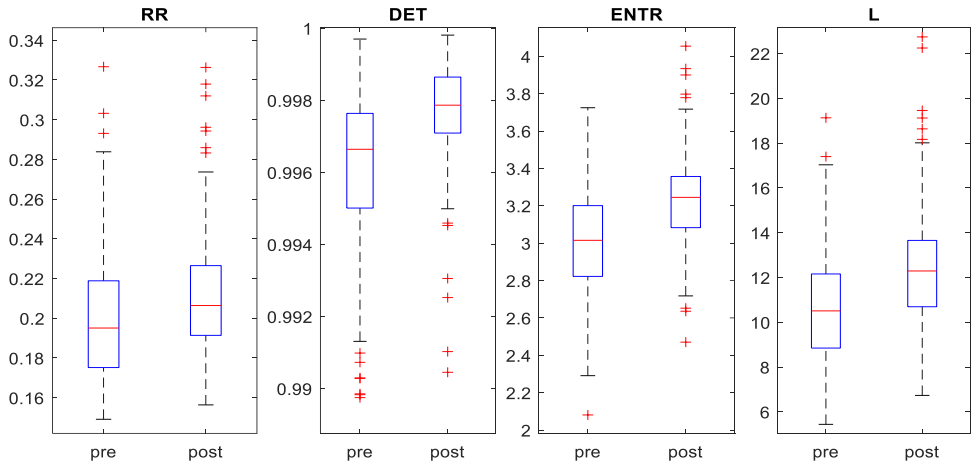

Figure 8.3 Boxplots of the quantification features of the recurrence plots for t = 1 samples, m = 3, and ε = 0.5. On each box, the central mark indicates the median, and the bottom and top edges of the box indicate the 25th and 75th percentiles, respectively. The whiskers extend to the most extreme data points not considered outliers, and the outliers are plotted individually using the '+' symbol

Other combinations of parameters were tested: ε was set to {0.3, 0.5, 0.7}; t was set to {1, 3, 33, 62} samples; m was set to {1, 2, 3, 4, 5, 6}. The delays t = {1, 3} samples were proposed as an initial exercise and t = {33, 62} samples were proposed since they are a multiple of the dominant period (which here is supposed to be a heart rate of 60 bpm). This ensures an accurate reconstruction of a system's underlying attractor [204]. Other studies [205] also propose to use the minimum lag which minimizes the autocorrelation function of the signals since this value maximizes the linear independence of the coordinates of the embedding vector.

Figure 8.4 shows the evolution of the AUC of DET, ENTR, L and RR with t, m and ε. As it can be seen in **Figure 8.4A**, AUC of RP-features decrease with m. **Figure 8.4B** shows that AUC is maximum for t = 33 and

Figure 8.4C shows that AUC is approximately constant with ε for DET and RR_{Rec}. The AUC of L increases with ε while AUC of ENTR decreases. RPs calculated with t = 33 samples, m = 2 and ε = 0.5 were used for the rest of this chapter due to its high AUC, Sen and Spe. **Table 8.3** shows the results for this combination. Other combinations which provided similar results were t = 33, m = 3 and ε = 0.5, and t = 1, m = 4 and ε = 0.5.

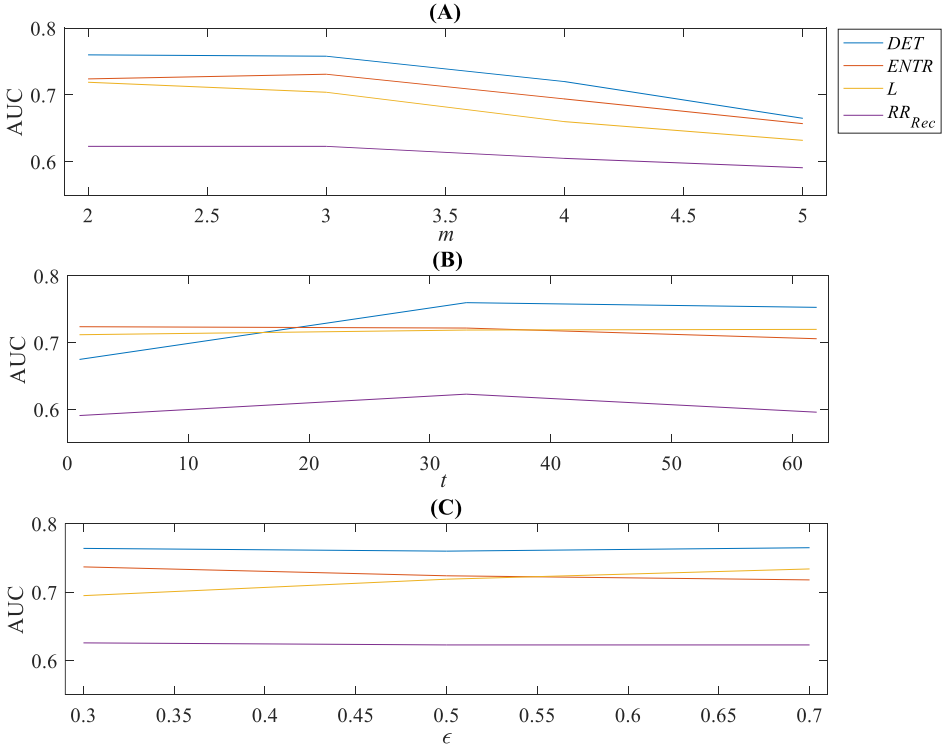

Figure 8.4 Evolution of AUC of the RP-derived features with the RP parameters: dimension m (A), lag t (B) and error ε (C)

DESCRIPTION OF RP-DERIVED FEATURES

	Both	Pre-LOC	Post-LOC	AUC	*Sen*	*Spe*
RR_{rec}	0.114 ± 0.036	0.108 ± 0.033	0.120 ± 0.038	0.623	46%	68%
DET	0.998 ± 0.002	0.997 ± 0.002	0.998 ± 0.001	0.760	81%	53%
ENTR	3.211 ± 0.347	3.074 ± 0.330	3.348 ± 0.309	0.724	67%	65%
L	13.2 ± 4.0	11.8 ± 3.3	14.7 ± 4.1	0.719	63%	70%

Table 8.3 Mean, standard deviation and discriminant analysis of the RP-derived features with t =33, m = 2, ε = 0.5. All differences have p-value < 0.05, rejecting the hypothesis that the distribution of the difference of the pairs of before and after LOC of a feature comes from a zero-median distribution

8.6 Changes in Features with Depth of Consciousness

For this analysis, a total of 83 cases from the CMA database explained in Chapter 3 were analyzed and both TFD-derived and RP-derived features were extracted. The rest of cases were discarded since the SQI was decreasing excessively often (>33% of the case) so that features could not be extracted. The index for depth of consciousness, qCON, was grouped into two different ways. First, the prediction probability P_k for awake/asleep was analyzed. Then, the prediction probability P_k was calculated for the four different states: awakeness, sedation, anesthesia, deep anesthesia. During surgical operations, patients are usually longer in the anesthesia or deep anesthesia states. Therefore, the largest equal amount of data points were selected for every state before calculating P_k values. **Table 8.4** compiles these P_k values. The P_k values have been reassigned according to Equation (48) to avoid directional information. Both TFD-derived and RP-derived features are included.

$$P_k' = |P_k - 0.5| + 0.5 \tag{48}$$

PREDICTION PROBABILITY P_K OF FEATURES

		4 states	2 states			4 states	2 states
IFs	$IF_{1_{mean}}$	0.538	0.594	TF Extended Freq. Features	E_{tot}	0.582	**0.715**
	$IF_{2_{mean}}$	0.538	0.604		$TFRE_q$	0.541	**0.683**
	$IF_{3_{mean}}$	0.531	0.637		$TFNRE_q$	**0.658**	**0.798**
	$IF_{4_{mean}}$	0.533	**0.650**		$\mathcal{FL}_{(0,1)}$	0.549	**0.704**
	$IF_{5_{mean}}$	0.560	0.570		$\mathcal{FL}_{(1,0)}$	0.625	**0.806**
	$IF_{1_{STD}}$	0.615	**0.688**		$\mathcal{FL}_{(1,1)}$	0.609	**0.791**
	$IF_{2_{STD}}$	0.647	**0.741**		$\mathcal{SF}$	0.549	0.628
	$IF_{3_{STD}}$	**0.678**	**0.751**		M_2	0.568	**0.719**
	$IF_{4_{STD}}$	0.646	**0.753**	TF Extended Time Features	m_{TF}	0.578	**0.759**
	$IF_{5_{STD}}$	0.593	**0.650**		σ^2_{TF}	0.539	**0.678**
Energy of IFs	E_1	0.594	**0.676**		γ_{TF}	0.585	**0.701**
	E_2	0.511	**0.723**		k_{TF}	0.566	**0.701**
	E_3	0.584	**0.722**		c_{TF}	**0.658**	**0.798**
	E_4	0.594	**0.699**	RP Extended Features	RR_{rec}	0.534	0.579
	E_5	0.578	**0.759**		DET	0.623	**0.687**
	Decay	0.570	0.532		ENTR	0.616	**0.650**
					L	0.628	**0.676**

Table 8.4 Prediction Probability P_k of calculated TFD-derived and RP-derived features for 2 and 4 patient states. Values above 0.65 are in bold and all values have p-value<0.005

8.7 Studied Correlations

Table 8.5 reports the correlations between CO, SV and HR and several TFD-derived features. All values included are statistically significant (p-value<0.05) and those which are not have been omitted. On the one side, no statistically significant correlations have been found between TFD-derived with blood pressure, HRV or depth of anesthesia. On the other side, no statistically significant correlations have been found between RP-derived with blood pressure, HRV or depth of anesthesia. It can be observed that HR is correlated with the mean of the IFs but CO is correlated with the rest of TFD-derived features. The SV is correlated with both groups of TFD-derived features.

CORRELATION BETWEEN FEATURES AND BLOOD FLOW INDICES

		CO	SV	HR
IFs	$IF_{1_{mean}}$	--	-0.42	0.60
	$IF_{2_{mean}}$	--	-0.40	0.55
	$IF_{3_{mean}}$	--	-0.41	0.59
	$IF_{4_{mean}}$	--	-0.43	0.64
	$IF_{5_{mean}}$	--	-0.43	0.77
TF Ext. Time Feat.	m_{TF}	0.85	0.66	--
	σ^2_{TF}	0.89	0.62	--
	E_{tot}	0.82	0.64	--
TF Extended Freq. Features	$TFRE_q$	-0.87	-0.67	--
	$\mathcal{FL}_{(0,1)}$	0.90	0.70	--
	$\mathcal{FL}_{(1,0)}$	0.72	0.54	--
	$\mathcal{FL}_{(1,1)}$	0.80	0.61	--
Energy of IFs	M_2	0.77	0.58	--
	E_1	0.80	0.51	--
	E_2	0.49	0.48	--
	E_3	0.50	0.35	--
	E_4	0.35	--	--
	E_5	0.85	0.66	--

Table 8.5 Pearson's Correlation values for CO, SV and HR with the studied TFD-derived. Only features with correlations above 0.30 which are statistically significant values have been included. In all cases, p-value<0.05

8.8 Prediction of Depth of Anesthesia using TFD-Derived and RP-derived Features

A fitted binary classification tree has been trained to predict patient depth-of-anesthesia states. Fitted binary classification trees develops predictive models based on both input and output data. First, data has been randomly divided into two sets of training and testing and the same amount of data points from every state were selected for the training and testing sets of data. A decision tree consists of branching conditions where the value of an input variable (also known as predictors, features, or attributes) is compared to a trained weight. The number of branches and the values of weights are determined in the training process.

In this case, the predictors for the patient state have been chosen from among the TFD-derived and RP-derived features with a higher prediction probability P_k. Two classifications for the patient depth-of-anesthesia states have been employed: two states (awake and asleep states) and four states (awakeness, sedation, general anesthesia and deep anesthesia). Performance of the classification trees is calculated as the percentage of correctly predicted data divided the total amount of data in the testing set. Results are included in **Table 8.6**. In such table, if more features are used to train the classification tree, the performance continues decreasing.

For two states, several decision trees provide prediction performance higher to 80%. In this case, the decision tree including $IF_{3_{STD}}$, $TFNRE_q$, c_{TF}, $\mathcal{FL}_{(0,1)}$, $\mathcal{FL}_{(1,1)}$, E_5, and the Minkowski distance M_2 provides a performance of 82% for the two-state case. In the case of decision trees with four states, performances are much inferior.

8.9 Prediction of Cardiac Output using TFD-Derived and RP-derived Features

Several ANFIS have been trained to predict cardiac output during the whole anesthesia procedures. Neuro-fuzzy systems combine two intelligent technologies [206], [207]. Neural networks are low-level computational structures which perform well with raw data but are opaque to the user. Fuzzy logic deals with reasoning at a higher level, using linguistic information acquired from domain experts but it lacks the ability to learn and cannot adjust itself to new environments. The integration of both technologies can combine the parallel computation and learning abilities of neural networks with the

human-like knowledge representation and explanation abilities of fuzzy systems. These systems can thus be trained to develop if-then fuzzy rules and determine membership functions for input and output variables of the system.

PERFORMANCE OF DECISION TREES

	4 states	2 states
$IF_{3_{STD}}$	39%	63%
$TFNRE_q$	33%	67%
c_{TF}	33%	67%
$\mathcal{FL}_{(0,1)}$	37%	74%
$\mathcal{FL}_{(1,1)}$	38%	76%
E_5	39%	76%
M_2	38%	82%
$IF_{4_{STD}}$	35%	81%
$IF_{2_{STD}}$	38%	80%
E_2	37%	75%
E_3	37%	72%

Table 8.6 Prediction performance calculated for each of the decision trees for two and four patient states. Note: each new decision trees includes the previous features

The trained system for the prediction of cardiac output consists of six layers (represented in **Figure 8.5**) and it employs a hybrid learning algorithm combining the least-squares estimator and the gradient descent method: neural connection weights are modified in order to progressively reduce an error measure. Rule consequent parameters are identified on the layer 5 by the least-square estimator and error is back-propagated to update the antecedent parameters which describe the membership function in layer 2 by gradient descent. Both antecedent and consequent parameters are optimized using a combination of the least-squares and backpropagation gradient descent methods. No prior knowledge of rule consequent parameters is required. In the example of **Figure 8.5**, x1 and x2 are any two input indices which enter the model in layer 1. Layer 2 is the fuzzification layer which is followed by layer 3 which is composed by Sugeno-type rules. In a Takagi and Sugeno's fuzzy if-then rule, the output of the rule is a linear combination of input variables plus a constant term, and the final output is the weighted average of each rule's outputs [208].

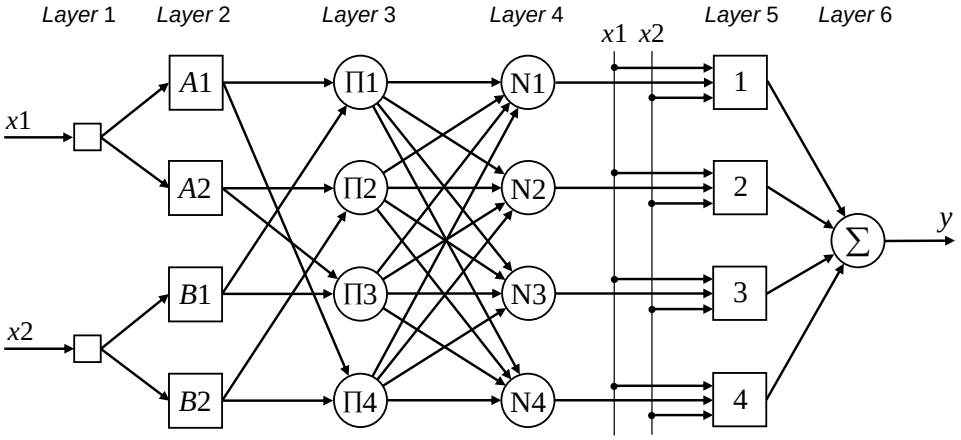

Figure 8.5 ANFIS with four rules: layer 1 is the input layer; layer 2 is the fuzzification layer; in layer 3, the rule layer, each neuron receives an fuzzy input and calculates the firing strength of the single Sugeno-type fuzzy rule it represents; layer 4 normalizes the received firing strength to the sum of firing strengths of all rules; layer 5 also receives the inputs x1 and x2 to calculate the weighted consequent value of a rule; layer 6 sums the outputs of all defuzzification neurons and produces the overall ANFIS output.

In total, one to five features ($\mathcal{FL}_{(0,1)}$, σ^2_{TF}, $\mathrm{TFRE_q}$, $\mathrm{E_5}$, $\mathrm{E_{tot}}$) are used to train an ANFIS system which tries to imitate Cardiac Output through the whole surgery. These features have been chosen according to their correlation with CO and no more features were chosen because the ANFIS error started to increase as the number of features increased. Data were equally divided into the training and testing sets of data (132,200 data points for each set). The error was calculated as the mean RMS difference between the real output and the predicted output of the training and testing sets of data and is included in **Table 8.7**.

ANFIS RESULTS

	Trained RMS (L/min)	Predicted RMS (L/min)
$\mathcal{FL}_{(0,1)}$	0.310	0.392
$\mathcal{FL}_{(0,1)}$, σ^2_{TF}	0.297	0.376
$\mathcal{FL}_{(0,1)}$, σ^2_{TF}, $\mathrm{TFRE_q}$	0.288	0.387
$\mathcal{FL}_{(0,1)}$, σ^2_{TF}, $\mathrm{TFRE_q}$, $\mathrm{E_5}$	0.283	0.390
$\mathcal{FL}_{(0,1)}$, σ^2_{TF}, $\mathrm{TFRE_q}$, $\mathrm{E_5}$, $\mathrm{E_{tot}}$	0.280	0.401

Table 8.7 Trained and predicted RMS for different ANFIS models trained to predict CO with TFD-derived features

As the predicted RMS error shows in **Table 8.7**, a prediction error of around 0.4 L/min in CO represents an error of around 10% of average CO.

Finally, taking into account that CO = SV·HR, the HR index has been also introduced in some of the previous ANFIS to test whether results could be improved. Results are included in **Table 8.8**. The Bland-Altman error has been calculated according to indications in Chapter 2. The ANFIS model with three TFD-derived features ($\mathcal{FL}_{(0,1)}$, σ^2_{TF}, and $TFRE_q$) and HR shows a Bland-Altman error of 14% and predicted RMS error of 0.44 L/min.

ANFIS RESULTS WITH HR INCLUDED

	Trained RMS (L/min)	Predicted RMS (L/min)	Bland-Altman Error
$\mathcal{FL}_{(0,1)}$, σ^2_{TF}, HR	0.248	0.392	15%
$\mathcal{FL}_{(0,1)}$, σ^2_{TF}, $TFRE_q$, HR	0.233	0.438	14%

Table 8.8 Trained and predicted RMS for different ANFIS models trained to predict CO with TFD-derived features and HR

The Bland-Altman analysis has been included along with the regression analysis in **Figure 8.6**. The regression analysis includes de regression line of determination coefficient R^2=0.86 calculated with n=132,200 data points (the testing set). The Bland-Altman analysis shows the limits of agreement (LOA) of the comparison between the predicted CO (CO_{Pred}) and the reference CO (CO_{Ref}) in absolute and percentual value.

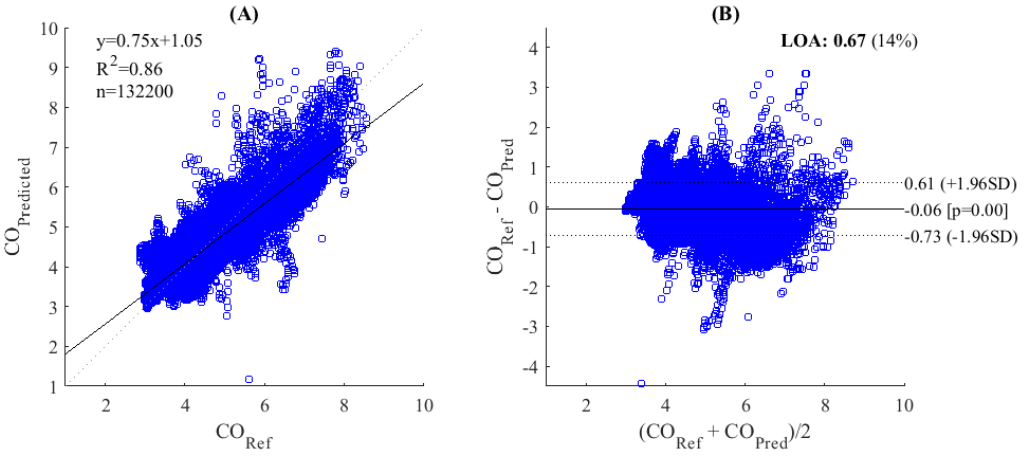

Figure 8.6 Regression analysis (A) and Bland-Altman analysis (B) for the ANFIS model with $\mathcal{FL}_{(0,1)}$, σ^2_{TF}, $TFRE_q$, and HR as predictors.

In **Figure 8.7**, a complete surgery is plotted as a reference. The figure shows how the predicted CO and the reference CO are very similar. Calculations for this concrete case show a total RMS error of 0.191 L/min and a Bland-Altman error of 7.30%. In this concrete case, it is noticeable how the error seems proportional to the magnitude of cardiac output and thus is inferior at the end of the surgery.

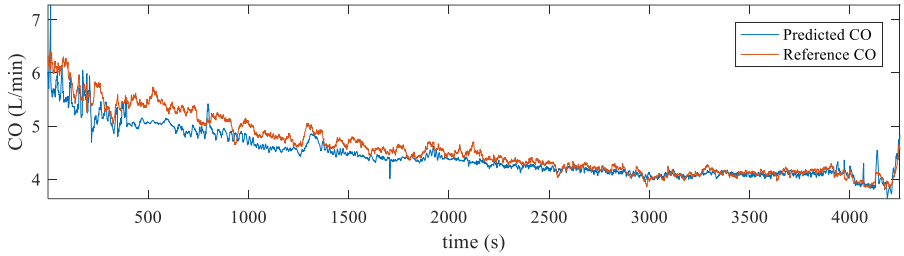

Figure 8.7 Reference and Predicted Cardiac Output for a full surgery

8.10 Discussion and Conclusion

In this analysis, all four RP-derived features decrease after LOC with a statistically significant difference. Moreover, both ENTR and L have an AUC, Sen and Spe above 60% when distinguishing between ICG pre-LOC and post-LOC signals for different combinations of RP parameters, such as referred in **Table 8.2** and **Table 8.3**. Nevertheless, the analysis of the prediction probability shows a low P_k for the RP-derived features, especially when 4 different states are considered, and the correlation of such features with HRV, BP, CO, HR and SV is not statistically significant. Nevertheless, previous studies had used RPs to analyze HRV [209].

Regarding the correlation of the blood flow indices and features, IF energy and TF extended frequency features are related to CO and SV. The highest correlations are with CO for $\mathcal{FL}_{(1,0)}$ (ρ = 0.90), σ^2_{TF} (ρ = 0.89), $TFRE_q$ (ρ = -0.87). The mean of the IFs are directly correlated to SV ($\rho \in$ [-0.43, -0.40]) and inversely correlated to HR ($\rho \in$ [0.55, 0.77]). No other correlations have been found.

When two patient states are considered (awake and asleep states), some of the TFD-derived features provide a good P_k above or around 0.75 (below or around 0.25). This is the case of the $TFNRE_q$, $\mathcal{FL}_{(1,0)}$, $\mathcal{FL}_{(1,0)}$, c_{TF}, STD of IF_2, IF_3, IF_4, and E_5. Nevertheless, when considering four different states, the features with the best prediction probability P_k are only $IF_{3_{STD}}$ (P_k = 0.678), $TFNRE_q$ (P_k = 0.658), c_{TF} (P_k = 0.342). These are promising results but

further analysis is required to improve them. Some of the options for this would be to use more complex TFD kernels such as the ones described in the previous chapters despite requiring a higher computational complexity, to consider 3 patient states instead of four (awakeness, sedation, anesthesia – both general and deep), to use a TFD with a higher time resolution. Currently, the time resolution is 1 Hz but it increase to 250 Hz. These suggestions will be taken into consideration in a future work.

Regarding the prediction models, TFD-derived and RP-derived features do not seem to be good predictors for the patient depth-of-anesthesia state. In the best case, a total of seven features ($\mathrm{IF}_{3_{\mathrm{STD}}}$, $\mathrm{TFNRE_q}$, $\mathrm{c_{TF}}$, $\mathcal{FL}_{(0,1)}$, $\mathcal{FL}_{(1,1)}$, E_5, M_2, $\mathrm{IF}_{4_{\mathrm{STD}}}$, $\mathrm{IF}_{2_{\mathrm{STD}}}$, E_2, and E_3) can be used to train a classification tree to predict patient state with a resulting performance of 82% calculated as the ratio of correctly predicted data when only two states are considered and of 38% when four states are considered.

Furthermore, ANFIS models trained to predict CO seem to provide promising results. The ANFIS model trained with three TFD-derived features ($\mathcal{FL}_{(0,1)}$, σ^2_{TF}, $\mathrm{TFRE_q}$) and the patient's heart rate provides LOA = 14%, which is far below the 30% acceptable for the interchangeability of indices, according to explanations in Chapter 2 [79] .

As explained before, no statistically significant correlations have been found between TFD-derived or RP-derived features with blood pressure, HRV. Nevertheless, as **Table 8.5** shows, TFD-derived features of the ICG seem to be related to the HR and to CO (which is also ultimately related to HR). In addition, ANFIS models with TFD-derived features have proved to predict CO with good results. TFD-derived features of the ICG could provide further information for the calculation of cardiac output. This hypothesis would need to be further investigated.

This page is left bank

Chapter 9

Validation Study of a Cardiac Output Monitor

Abstract

This chapter is based on an excerpt of an article published during the present Doctoral Thesis [210]. A comparison between the LiDCOrapid monitor and the qCO monitor is presented. The Bland-Altman method is used for such comparison.

9.1 Introduction

The aim of this last chapter is to report a performance test of the qCO using the LiDCOrapid as a reference. The two devices can monitor the CO continuously, but with different methods. The qCO detects variations in the impedance, while LiDCOrapid processes the pressure waveform to estimate the CO [47].

Several studies report an improved outcome with the usage of LiDCOrapid to guide goal-directed fluid therapy after emergency laparotomy [211], a reduced length of hospital stay in colorectal surgery [212], and in high-risk abdominal and bariatric surgery [213]. Therefore, the aim of this study was to compare the behaviors of LiDCOrapid and the new qCO device during anesthesia procedures in the operatory room.

9.2 Methods

Fifteen patients undergoing major surgery under general anesthesia at the Zhongshan Hospital in Shanghai were assessed in this observational study. Details of the patients and operations were reported in **Table 3.1**.

The synchronization between both devices was ensured by annotating the exact start time given by the two devices. Data values of cardiac output were not taken into consideration when there was an instantaneous variation of either HR, CO or SV greater than 25% which was not justified from a clinical point of view. This led to a total rejection rate of < 2% for LiDCOrapid and < 1% for qCO. Two patients (one for gastrostomy and another one for cytoreductive surgery) were excluded due to excessive noise, and thus a total of thirteen patients remained to be considered for this study. To create the pairs of cardiac output values, each CO point from qCO was paired with the closest CO point by LiDCOrapid within a time difference of one second between both points.

9.2.1 Statistical Analysis

The qCO agreement with the LiDCOrapid's signal was assessed using different statistical techniques: regression and Bland-Altman analysis. The Bland-Altman analysis is explained in Chapter 2.

A regression analysis was conducted to estimate the relationship between the cardiac outputs calculated by the LiDCOrapid and qCO monitors. Regression can show whether pairs of indices are related but a high correlation does not imply a good agreement between two methods. Bland-Altman

analysis for repeated measurements per patient were used for the pool of patients to assess the agreement between qCO and LiDCOrapid. The Bland-Altman plot, also known as difference plot, is a method to compare two techniques (usually one of them as a reference) for the measurement of the same parameter. The correlation is shown by plotting the differences between the measurements produced by both methods against the mean value of such measurements.

A linear mixed model with random effects was used to adjust for the interaction between the two methods and the time replicates of patients, resulting in a common standard deviation (SD) to calculate the limits of agreement (LOA) with its upper and lower limits determined by the mean difference between data from the reference and studied method ± 1.96 SD [82], [214], [215]. The percentage error was calculated as the ratio of 2 SD of the bias to the mean CO and was considered clinically acceptable when it was 30% or less, as proposed by Critchley and Critchley [79], [80]. Before computing the Bland-Altman plot, according to Squara et al. [216], each recording should be divided into unchanging, increasing and decreasing periods and the description of a device can only be estimated on unchanging, stable periods.

9.3 Results

Data from 13 patients, 8 males and 5 females were included into final analysis. Not a single patient suffered from any complication in the context of the present study. Blood loss, fluid administration and hypotension periods after induction were not included into our analysis. **Figure 9.1** displays one of the cases. In this figure, it is visible that qCO and LiDCOrapid share a common overall trend. However, LiDCOrapid shows several sudden drops in cardiac output for which there is no reported clinical evidence and which are not followed by the qCO monitor.

Patient hemodynamic data are reported in **Table 3.1**. According to qCO, cardiac output ranged 4.5 ± 0.5 L/min, stroke volume 69.6 ± 8.8 mL/beat. According to LiDCOrapid, these values were 4.5 ± 0.7 L/min and 69.8 ± 10.9 mL/beat, respectively. Heart rate was the same for both devices: 64.8 ± 7.5 bpm. Non-significant differences were observed between qCO and LiDCOrapid regarding those values.

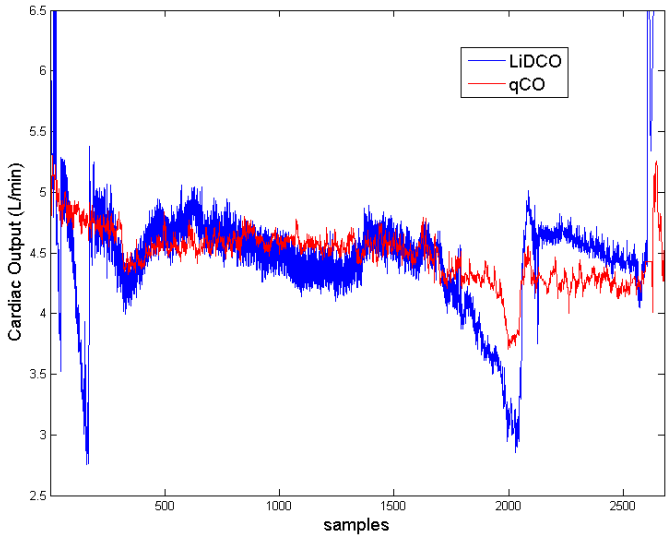

Figure 9.1 The cardiac output assessed by the qCO and the LiDCOrapid. The figure shows an example of a recording obtained with qCO and LiDCOrapid

HEMODYNAMIC CHARACTERISTICS	
Surgery duration (min)	135.1 ± 59.63
Cardiac Output (L/min)	4.5 ± 0.5 (qCO); 4.5 ± 0.7 (LiDCOrapid)
Stroke Volume (mL/beat)	69.6 ± 8.8 (qCO); 69.8 ± 10.9 (LiDCOrapid)
Heart Rate (bpm)	64.8 ± 7.5 (qCO and LiDCOrapid)

Table 9.1 Hemodynamic characteristics. All values are presented as mean ± standard deviation

The operative procedures, whose type is also reported in **Table 9.1**, lasted 113 [88 200] minutes (median and 25, 75-percentiles). A median of 3,557 [2,407 6,996] points (median and 25, 75-percentiles) were paired from qCO and LiDCO cardiac output.

Regression analysis showed no good indication of proportional bias (r^2=0.3987, p-value<0.05). This analysis and the Bland-Altman plot are included in **Figure 9.2** and **Figure 9.3**, respectively. The Bland-Altman plot compares the differences in CO values against the mean of the total measures of both methods, qCO and LiDCOrapid. In **Figure 9.3**, the black solid line represents the mean difference and the dotted lines represent the accepted limits of agreement (mean difference ± 2 SD). The standard deviation has been corrected for the pooled data using two variances: that for repeated differences between the two methods on the same subject and that for the differences between the averages of the two methods across subjects.

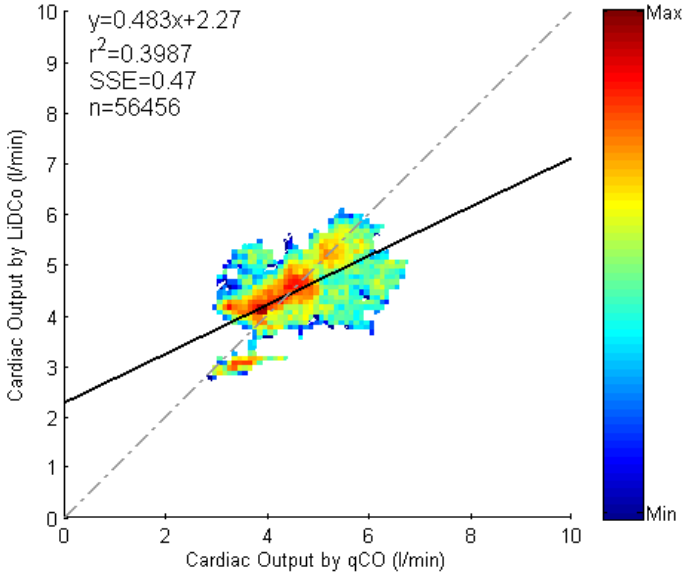

Figure 9.2 Regression analysis of the pool data

In this case, the Bland-Altman analysis shows a mean bias of -0.03 ± 0.71 L/min. Upper and lower limits of agreement are 1.4 and -1.4, respectively. Percentage error was 29%, which is just below the recommended 30% [79], [80]. The color bar ranges from a 0 to 1043 in logarithmic units, so the areas outside the limits of agreement are not relevant compared to the rest of the figure.

9.4 Discussion

There is a reasonable amount of studies on the LiDCOrapid technology. In a study by Phan and colleagues [217], LiDCOrapid showed an increase of 41% after a fluid bolus measurement. When comparing the test device to thermodilution, the Kappa statistic (a statistic which measures inter-rater agreement for categorical data) showed fair agreement of 0.28. After vasopressor administration, there was also significant variation in the change in cardiac output. Using Bland-Altman analysis, the precision of LiDCOrapid in comparison to thermodilution showed minimal bias, but wide limits of agreement with percentage errors of 54.2%. In this study, other instruments were also tested against thermodilution with similar results. These findings indicated that LiDCOrapid, VigileoFlotrac and Oesophageal Doppler

Monitor (ODM) differ in their responses, do not always provide the same information as thermodilution and should not be used interchangeably to track cardiac output changes.

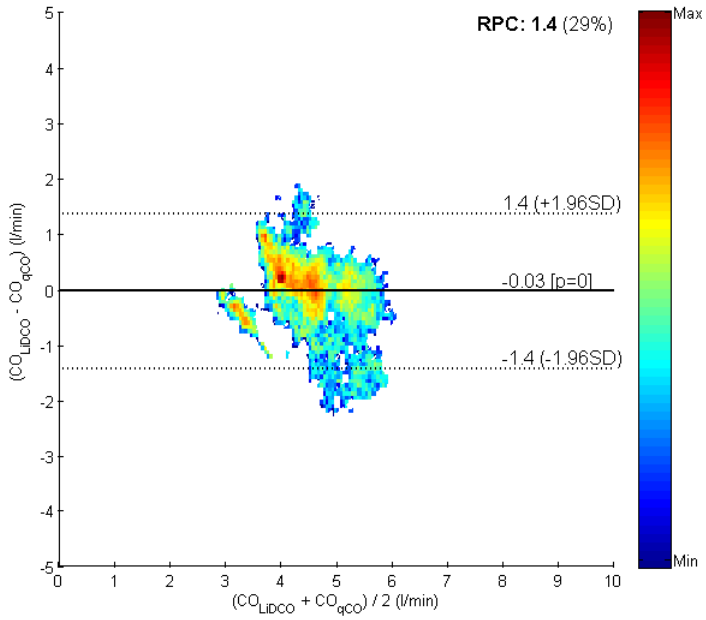

Figure 9.3 Bland-Altman plot of comparing the differences in CO values against the mean of the total measures of qCO and LiDCOrapid. The color column indicates the number of points in each square

Nordström and colleagues [38] compared ODM and LiDCOrapid for stroke volume (SV) optimization during colorectal surgery using fluid challenges. For 172 paired SV values, the overall correlation was $\rho = 0.39$, and bias (limits of agreement) -28 [-91 35] mL, percentage error 70%. The ability of LiDCOrapid to track changes in SV compared to ODM was weak with a concordance rate of 80%, and a sensitivity and specificity of 48% and 81%, respectively, to detect a positive fluid challenge.

Davies and colleagues [54] conducted a study where simultaneous reading of SV, stroke volume variation (SVV) and pulse pressure variation (PPV) from LiDCOrapid and FloTrac were taken in 20 patients and compared with ODM. The main conclusion was that SV measured by the FloTrac and LiDCOrapid systems does not correlate with the ODM, has poor concordance and a clinically unacceptable percentage error. However, SVV measured by the LiDCOrapid has clinical utility.

Costa and colleagues [49] studied the level of agreement between cardiac output obtained by LiDCOrapid and continuous cardiac output (CCO) and intermittent cardiac output (ICC) obtained by the pulmonary artery catheter (PAC) in patients after liver transplantation. The performance of LiDCOrapid was moderate in detecting changes in ICO.

The current study statistically describes the new qCO monitor. It therefore constitutes an initial validation of this new monitor. Today, clinicians can choose amongst a wide variety of less-invasive or noninvasive devices to calculate cardiac output. Each device consists on a proprietary software algorithm which processes different types of signals. However, several studies have demonstrated a lack of accuracy in these monitors [38], [49], [54], [79], [217]–[219]. Quantium Medical qCO monitors is born from the intention of applying advanced signal processing techniques to bioimpedance signals in order to offer a totally noninvasive device to measure cardiac output.

Our main finding is the acceptable percentage error of the qCO monitor compared to the LiDCOrapid system. It should be mentioned that several studies have previously demonstrated the validity of monitors using a technology similar to qCO in comparison to gold standards. The NICOM monitor (Cheetah Medical) [220] compared to thermodilution showed a mean bias of -0.81 with 95% limits of agreement of [-3.54, +1.92]. Cardiac output by NICOM was also more precise than by thermodilution (precision of 3.5±0.3% for NICOM versus 9.6±6.1% for thermodilution, p-value<0.001).

In our study, the Bland-Altman plot between qCO and LiDCO shows that the majority of values adjusted to the agreement limits and the hot spots are distributed near zero (represented with the hottest colors in **Figure 9.3**). The mean bias is -0.03 and the limits of agreement are +1.4 and -1.4. Given the large sample size (56,456 total samples), this distribution of the points demonstrates a very low bias.

In a similar study performed for the validation of electrical velocimetry (EV) with cardiac magnetic resonance imaging (CMR) as referenced in [68], the authors admitted an insufficient agreement and referred to a Bland-Altman plot with a mean bias of 1.2 ± 1.4 L/min. This represents a higher mean bias and wider limits of agreement compared to the data published in the present article. Consequently, it is possible to affirm that nearly identical results can be provided from qCO and LiDCOrapid.

Our study presents a number of limitations which must be considered. First, the observational protocol included a variety of surgical operations and did not include exact measuring points. It is especially important to note that this variety of surgical operations can imply different requirements in fluid management. Although this introduces a higher variability in our findings, it was useful to characterize the general behavior of the qCO monitor. Nonetheless, one should recognize that this methodology might not provide sufficiently clean data to make perfect comparisons between technologies.

This is also linked with the fact that segmentation into unchanged, increasing and decreasing periods was not possible. Some authors [216] have stated that the comparison and analysis of medical devices must be conducted during stable periods. However, the analysis of the trends in our recordings showed a lack of many unchanged periods and, therefore, the analysis of the bias was performed on all data and not only on the data with unchanging trend. At the same time, this implies an important limitation although it should also be noted that the purpose of this work was to compare the behavior of both instruments under the same varying conditions.

As previously mentioned, LiDCOrapid is not a gold standard. Further studies against gold standards, such as the pulmonary artery catheter, will be required in order to complete the validation of the new qCO monitor. Moreover, in future studies, more protocol-based procedures would be highly recommended. Outcome studies are also a powerful tool to take into account in order to validate the benefits of the usage of the qCO monitor. Furthermore, the implementation of more detailed protocols will also allow determination of the trending ability of changes between qCO and other gold standard technologies.

Finally, future studies will need to include the analysis of the precision of the qCO device as reported in [73]. Precision is a major issue in clinical monitoring which has also been cited for other devices during the discussion but not analyzed for the case of the qCO.

9.5 Conclusions

In conclusion, the results indicate that cardiac output calculated with the qCO monitor is comparable to the values calculated by the LiDCOrapid monitor. In line with this and previous studies [102], [221], the qCO has demonstrated a very low bias with the LiDCOrapid monitor in a variety of different situations.

Future studies need to be performed to compare the qCO with a gold standard in order to ensure a complete validation. Certainly, the availability and reliability of noninvasive cardiac output devices make cardiac output monitoring an attractive option for all clinical situations.

This page is intentionally left blank.

Chapter 10

Conclusions and Future Work

Abstract

In this final chapter the most important findings and contributions of the present dissertation are summarized, from the concept of the devices used in this research to the application and possible uses of the fast impedance measurements performed. In addition, several guidelines for further work in the topic are proposed.

10.1 Conclusions

As it was stated in the Introduction, the main objective of this Doctoral Thesis was «the development of signal treatment techniques for the thoracic bioimpedance signals in order to create an innovative hemodynamic monitor». This main objective was also divided into several minor objectives.

The present Doctoral Thesis incorporates a presentation on the available cardiac output monitoring technologies. Regarding the different options, patient risk is related to invasiveness, which is, in turn, inversely related to accuracy. Thus, the invasive Swan-Ganz catheter continues to be the gold standard of the technique but its invasiveness – and associated risk for the patient – implies that this measurement device is only used in critically ill patients in which the improved accuracy compensates for the increased risk. In the rest of cases, minimally invasive and noninvasive monitors are preferred and the competition lies on the accuracy of such techniques.

This Doctoral Thesis has produced a considerable amount of clinical data grouped in different databases. The clinical trials conducted in Barcelona, Hong Kong, Santiago and Shanghai are valuable resources which have been used to validate the methodologies discussed in this text. In Barcelona, Santiago and Shanghai, the anesthesia were induced with propofol and remifentanil or fentanyl. Sevoflurane was also used for maintenance in some cases.

The previous databases have also permitted to test different relationships between blood flow, blood pressure and heart rate variability in this concrete anesthetic context. During anesthesia, there was a decrease in cardiac output and blood pressure after loss of consciousness. Except from the index reflecting the normalized high-frequency spectral power of the HRV, the rest of HRV indices also decreased after LOC indicating a decrease in both sympathetic and vagal activity. Such exception indicates that although both high-frequency and low-frequency components of the HRV decrease after the onset of anesthesia, the high-frequency power decreases less than the low-frequency power does. Gender differences in HR and CO, and age differences in HRV measurements were also found after LOC. In addition to these results, a new method to create synthetic signals with known time-frequency characteristics has been designed and implemented using the ICG signals.

Concerning the relationship between ICG and ECG signals, RR and CC segments are very much comparable ($\rho = 0.998$, p-value < 0.0005). In fact, this can be used in cardiac output monitors in order to check that the R and

C points are properly located on the ECG and ICG signals. The time delay between the electrical activity of the heart (represented by the ECG) and its mechanical activity (represented by the ICG) can be measured with the RC segment or the ratio RC/RR. The ratio RC/RR is inversely proportional to RR and is lower than 30% for RR intervals between 700 and 1000 ms, which would correspond to a heart rate of 86 and 60 bpm, respectively.

Time-Frequency Distributions (TFD) have been widely studied in this Doctoral Thesis. The basic knowledge of TFD has been reviewed and a new method to test TFD kernels with multi-tone synthetic signals based on real biomedical signals has been designed and implemented. It consists on using well-known, synthetic signals to check how different kernels can locate the instantaneous frequencies of the synthetic signals. In the case of the ICG signals, some traditional kernels such as Born-Jordan Distribution (BJD) could be discarded due to the results of this work. A new performance parameter has also been designed as the correlation between the studied TFDs of the synthetized ICG real-based signal and the addition of the Wigner-Ville Distributions (WVD) of the two single tone in the synthetized ICG signal. Nevertheless, the final choice of the kernel to use must follow a thorough evaluation of the performance measurements described in chapter 6 and it also depends on the available knowledge of the type of signals to analyze.

A wide range of TFD features has been presented and calculated on ICG signals. These features were based on different characteristics of the signals: single-value decomposition, entropy, concentration, time or frequency characteristics. Feature values from before and after the loss of consciousness during anesthesia have been compared and several TFD features have proven to be significantly different in these two situations. These features have also been calculated on TFDs with different kernels. When analyzing different anesthetic states, the TF Rényi entropy was the most prominent feature. Regarding the various kernels which were analyzed, the Extended Modified Beta Distribution (EMBD) was the most successful for the extraction of features showing statistically significant differences in different anesthesia points.

Many of the different TFD features used in this Doctoral Thesis also correlate with the patients' cardiac output, stroke volume and heart rate. Furthermore, the prediction probability P_k of many of the TFD-derived features to detect two anesthesia states (awake/asleep) is also acceptable,

reaching up to 0.798 for the normalized Rényi Entropy. Nevertheless, results are less promising for the ability of those TFD-derived features to differentiate between four patient states (awakeness, sedation, general anesthesia and deep anesthesia) and the prediction probability was always less than 0.68.

Decision trees have been trained to differentiate between two and four states. For two states, several decision trees provided prediction performance (ratio of correctly predicted results over the total of decisions) higher to 80%, although for four states, results were much inferior. Finally, several ANFIS systems have also been trained to predict cardiac output by using TFD-derived features and Heart Rate with excellent results. The best results have been obtained with an ANFIS system which combines three TFD-derived features (Rényi Entropy, Flux, and TF signal variance) and heart rate. This provided a Bland-Altman error of 14% and predicted RMS error of 0.44 L/min, which is considered satisfactory.

The qCO monitor includes several algorithms developed in this Doctoral Thesis and a comparison against one of its main competitors, the LiDCO monitor, has been included at the end of this work. This work has in conclusion enabled the qCO monitor to improve its resistance to noise and its calculation methods of cardiac output.

From a business perspective, the success of this Doctoral Thesis relies on three main points:

- the filing of a patent containing the algorithms discussed in this Doctoral Thesis;
- the CE mark of the qCO monitor;
- and the business decision to engage in new clinical trials to continue developing this monitor based on the results of this Doctoral Thesis.

10.2 Ongoing and Future Work

As explained in the previous section, Quantium Medical continues to develop and improve the qCO monitor for noninvasive cardiac output monitoring. The TFD-derived and RP-derived features explained in Chapter 8 continue to be developed and tested over the CMA database explained in Chapter 3. Several approaches have already been mentioned in Chapter 8.

Future steps will also be based on the consecution of a new database comparing the qCO with a gold standard monitor (or similar). Further techniques explained in this Doctoral Thesis will be then added to new impedance cardiography signals recorded by the qCO monitor and the cardiac output calculated will be compared to a gold standard.

This page is intentionally left blank.

Publications, Patents and Conference Contributions

Publications

Escrivá Muñoz J, Gambús Cerrillo P, Jensen EW, Vallverdú M (2017). Anesthesia Loss of Consciousness Effects on RC Cardiac Interval, Heart Period and Arterial Blood Pressure. PLOS ONE. Submitted.

Escrivá Muñoz J, Pan Y, Ge S, Jensen EW, Vallverdú M (2107). Performance of Time-Frequency Distributions for Impedance Cardiography Signals. Medical & Biological Engineering & Computing. Accepted.

Escrivá Muñoz J, Gambús Cerrillo P, Jensen EW, Vallverdú M (2017). Time-Frequency Features for Impedance Cardiography Signals during Anesthesia Using Different Distribution Kernels. Methods of Information in Medicine. Accepted.

Escrivá Muñoz J, Gabarrón E, Fort P, Pan Y, Ge S, Liao Q, Vallverdú M (2016). Comparison of Two Cardiac Output Monitors, qCO and LiDCO, during General Anesthesia. M J Anest 1(1): 002.

Palomar A, Escrivá Muñoz J, Melià U, Clariá F, Guaita M, Santamaria J, Vallverdú M (2017). Acceleration and deceleration processes in cardiac rhythm for the assessment of daytime sleepiness. PLOS ONE. Submitted.

Patents

Escrivá Muñoz J, Jensen EW (2017). System and Method for Estimating the Stroke Volume and/or the Cardiac Output of a Patient. Patent Application Number: EP17382625.6

Conference Contributions

Escrivá Muñoz J, Galea Cazorla A, González Pijuán C, Vallverdú M, Caminal P, Jensen EW (2016). Generación de bioseñales sintéticas mediante series de Fourier variantes en el tiempo. XXXVII Jornadas de Automática, Madrid.

Gabarrón E, Escrivá J, Jospin M, Fontanet J, Jensen EW, Gambús PL (2015). Noninvasive cardiac output measurement by impedance plethysmography under general anesthesia, European Society of Anesthesiology, Berlin.

References

[1] W. G. Kubicek, J. N. Karnegis, R. P. Patterson, D. A. Witsoe, and R. H. Mattson, "Development and evaluation of an impedance cardiac output system.," *Aerosp. Med.*, vol. 37, no. 12, pp. 1208–12, Dec. 1966.

[2] E. E. C. de Waal, F. Wappler, and W. F. Buhre, "Cardiac output monitoring.," *Curr. Opin. Anaesthesiol.*, vol. 22, no. 1, pp. 71–77, 2009.

[3] A. A. V. José M. Ferrero Corral, José M. Ferrero y de Loma-Osorio, F. Javier Saiz Rodríguez, *Bioelectronics. Señales bioeléctricas*. SPUPV, 1994.

[4] R. Gordan, J. K. Gwathmey, and L.-H. Xie, "Autonomic and endocrine control of cardiovascular function.," *World J. Cardiol.*, vol. 7, no. 4, pp. 204–14, Apr. 2015.

[5] M. Sabe and F. J. Heupler, "Cardiac output," in *Cardiovascular Hemodynamics – An Introductory Guide*, S. Anwaruddin, J. M. Martin, J. C. Stephens, and A. T. Askari, Eds. 2013, pp. 65–71.

[6] D. Reuter, A. Kirchner, T. Felbinger, F. Weis, E. Kilger, P. Lamm, and a E. Goetz, "Usefulness of left ventricular stroke volume variation to assess fluid responsiveness in patients with reduced cardiac function," *Crit Care Med*, vol. 31, no. 5, pp. 1399–404, 2003.

[7] Friesen, "A comparison of the noise sensitivity of nine QRS detection algorithms," *IEEE Trans. Biomed. Eng.*, vol. 34, pp. 1878–83, 1990.

[8] Task Force of The European Society of Cardiology and The North American and S. of P. and Electrophysiology, "Guidelines on heart rate variability," *Eur. Heart J.*, pp. 354–381, 1996.

[9] R. P. Patterson, "Fundamentals of impedance cardiography," *IEEE Eng. Med. Biol. Mag.*, vol. 8, no. 1, pp. 35–38, 1989.

[10] E. Soler, M. Faus, R. Burguera, J. Fernandez, and P. Mula, *Anestesiología*. 2016.

[11] O. Tirel, C. Chanavaz, J. Y. Bansard, F. Carré, C. Ecoffey, L. Senhadji, and E. Wodey, "Effect of remifentanil with and without atropine on heart rate variability and RR interval in children," *Anaesthesia*, vol. 60, no. 10, pp. 982–989, 2005.

[12] K. Shinohara, H. Aono, G. K. Unruh, J. D. Kindscher, and H. Goto, "Suppressive effects of remifentanil on hemodynamics in baro-denervated rabbits.," *Can. J. Anaesth.*, vol. 47, no. 4, pp. 361–366, 2000.

[13] M. A. Wujtewicz, L. Hasak, P. Twardowski, E. Zabul, and R. Owczuk, "Evaluation of the relationship between baseline autonomic tone and the vagotonic effect of a bolus dose of remifentanil," *Anaesthesia*, vol. 71, no. 7, pp. 823–828, 2016.

[14] M. Zaballos, C. Jimeno, J. Almendral, F. Atienza, D. Patiño, E. Valdes, J. Navia, and M. Anadón, "Cardiac electrophysiological effects of remifentanil: study in a closed-chest porcine model," *Br. J. Anaesth.*, vol. 103, no. 2, pp. 191–198, 2009.

[15] A. Vanegas Saavedra, *Anestesia intravenosa*. Editorial Médica Internacional, 2009.

[16] C. S. Deutschman, A. P. Harris, and L. A. Fleisher, "Changes in heart rate variability under propofol anesthesia: a possible explanation for propofol-induced bradycardia.," *Anesth. Analg.*, vol. 79, no. 2, pp. 373–377, 1994.

[17] Q. Liu, A. Kong, R. Chen, C. Qian, S. Liu, B. Sun, L. Wang, L. Song, and J. Hong, "Propofol and arrhythmias: two sides of the coin.," *Acta Pharmacol. Sin.*, vol. 32, no. 6, pp. 817–23, 2011.

[18] A. V Krassioukov, A. W. Gelb, and L. C. Weaver, "Action of propofol on central sympathetic mechanisms controlling blood pressure.," *Can. J. Anaesth.*, vol. 40, no. 8, pp. 761–9, 1993.

[19] T. J. Ebert, "Sympathetic and hemodynamic effects of moderate and deep sedation with propofol in humans.," *Anesthesiology*, vol. 103, no. 1, pp. 20–4, 2005.

[20] N. Kanaya, N. Hirata, S. Kurosawa, M. Nakayama, and A. Namiki, "Differential effects of propofol and sevoflurane on heart rate variability.," *Anesthesiology*, vol. 98, no. 1, pp. 34–40, 2003.

[21] T. J. Ebert, M. Muzi, R. Berens, D. Goff, and J. P. Kampine, "Sympathetic responses to induction of anesthesia in humans with propofol or etomidate," *Anesthesiolog*, vol. 76, pp. 725–733, 1992.

[22] B. J. Robinson, T. J. Ebert, T. . O'Brien, M. D. Colinco, and M. Muzi, "Mechanisms whereby propofol mediates peripheral vasodilation in humans," *1Anesthesiology*, vol. 86, pp. 64–72, 1997.

[23] Hu. Xu, M. Aibiki, S. Yokono, and K. Ogli, "Dose-dependent effects of

propofol on renal sympathetic nerve activity, blood pressure and heart rate in urethane-anesthetized rabbits," *Eur. J. Pharmacol.*, vol. 387, no. 1, pp. 79–85, 2000.

[24] O. Tiurmina, L. Conlay, and O. Medvedev, "Propofol suppresses sympathetic activity and inhibits the baroreceptor reflex in waking rats," *Eksp Klin Farmakol.*, vol. 56, no. 2, pp. 21–24, 1993.

[25] H. Dupont, P. Squara, H. Dupong, and P. Squara, "Cardiac output monitoring," *Curr. Opin. Anaesthesiol.*, vol. 9, no. 6, pp. 490–494, 1996.

[26] P. E. Marik, "Noninvasive cardiac output monitors: a state-of the-art review.," *J. Cardiothorac. Vasc. Anesth.*, vol. 27, no. 1, pp. 121–34, Feb. 2013.

[27] M. Cecconi, C. Corredor, N. Arulkumaran, G. Abuella, J. Ball, R. M. Grounds, M. Hamilton, and A. Rhodes, "Clinical review: Goal-directed therapy - what is the evidence in surgical patients? The effect on different risk groups," *Crit. care*, vol. 17, no. 2, p. 209, 2013.

[28] M. A. Hamilton, M. Cecconi, and A. Rhodes, "A systematic review and meta-analysis on the use of preemptive hemodynamic intervention to improve postoperative outcomes in moderate and high-risk surgical patients," *Anesth. Analg.*, vol. 112, no. 6, pp. 1392–1402, Jun. 2011.

[29] S. J. Parker and O. Boyd, "Haemodynamic optimisation: are we dynamic enough?," *Crit. Care*, vol. 15, no. 5, p. 1003, 2011.

[30] S. T. Gurgel and P. do Nascimento, "Maintaining tissue perfusion in high-risk surgical patients," *Anesth. Analg.*, vol. 112, no. 6, pp. 1384–1391, Jun. 2011.

[31] M. C. Bellamy, "Wet, dry or something else?," *Br. J. Anaesth.*, vol. 97, no. 6, pp. 755–757, Sep. 2006.

[32] H. G. Wakeling, M. R. McFall, C. S. Jenkins, W. G. A. Woods, W. F. A. Miles, G. R. Barclay, and S. C. Fleming, "Intraoperative oesophageal Doppler guided fluid management shortens postoperative hospital stay after major bowel surgery," *Br. J. Anaesth.*, vol. 95, no. 5, pp. 634–642, Sep. 2005.

[33] E. Widmaier, R. Hershel, and K. Strang, *Vander's human physiology: the mechanisms of body function*, 14th ed. New York, 2016.

[34] D. A. Hett and M. M. Jonas, "Non-invasive cardiac output monitoring.," *Intensive Crit. Care Nurs.*, vol. 20, no. 2, pp. 103–8, Apr. 2004.

[35] B. Saugel, M. Cecconi, J. Y. Wagner, D. A. Reuter, and Reu, "Noninvasive continuous cardiac output monitoring in perioperative and intensive care medicine," *Br. J. Anaesth.*, vol. 114, no. 4, pp. 562–575, Apr. 2015.

[36] T. Nishikawa and S. Dohi, "Errors in the measurement of cardiac output by thermodilution," *Can. J. Anaesth.*, vol. 40, no. 45, pp. 142–153.

[37] C. K. Hofer, M. T. Ganter, and A. Zollinger, "What technique should I use to measure cardiac output?," *Curr. Opin. Crit. Care*, vol. 13, no. 3, pp. 308–17, Jun. 2007.

[38] J. Nordström, C. Hällsjö-Sander, R. Shore, H. Björne, and R. P. Mahajan, "Stroke volume optimization in elective bowel surgery: A comparison between pulse power wave analysis (LiDCOrapid) and oesophageal Doppler (CardioQ)," *Br. J. Anaesth.*, vol. 110, no. 3, pp. 374–380, Mar. 2013.

[39] A. Feldheiser, V. Pavlova, K. Weimann, O. Hunsicker, M. Stockmann, M. Koch, A. Giebels, K.-D. Wernecke, and C. D. Spies, "Haemodynamic optimization by oesophageal doppler and pulse power wave analysis in liver surgery: a randomised controlled trial.," *PLoS One*, vol. 10, no. 7, p. e0132715, 2015.

[40] E. O'Loughlin, M. Ward, A. Crossley, R. Hughes, A. P. Bremner, and T. Corcoran, "Evaluation of the utility of the Vigileo FloTrac ™ , LiDCO ™ , USCOM and CardioQ ™ to detect hypovolaemia in conscious volunteers: a proof of concept study," *Anaesthesia*, vol. 70, no. 2, pp. 142–149, Feb. 2015.

[41] N. Zoremba, J. Bickenbach, B. Krauss, R. Rossaint, R. Kuhlen, and G. Schälte, "Comparison of electrical velocimetry and thermodilution techniques for the measurement of cardiac output.," *Acta Anaesthesiol. Scand.*, vol. 51, no. 10, pp. 1314–9, Nov. 2007.

[42] K. Ameloot, P. Palmers, and M. L. N. G. Malbrain, "The accuracy of noninvasive cardiac output and pressure measurements with finger cuff," *Curr. Opin. Crit. Care*, vol. 21, no. 3, p. 1, 2015.

[43] K. Ameloot, K. Van De Vijver, O. Broch, N. Van Regenmortel, I. De Laet, K. Schoonheydt, H. Dits, B. Bein, and M. L. N. G. Malbrain, "Nexfin noninvasive continuous hemodynamic monitoring: validation against continuous pulse contour and intermittent transpulmonary thermodilution derived cardiac output in critically ill patients," *Sci. World J.*, 2013.

[44] R. B. P. de Wilde, J. J. Schreuder, P. C. M. van den Berg, and J. R. C. Jansen, "An evaluation of cardiac output by five arterial pulse contour techniques during cardiac surgery," *Anaesthesia*, vol. 62, no. 8, pp. 760–768, 2007.

[45] M.-O. Fischer, M. Diouf, R. B. P. De Wilde, H. Dupont, J.-L. Hanouz, and E. Lorne, "Evaluation of cardiac output by 5 arterial pulse contour techniques using trend interchangeability method," *Med. (United States)*, vol. 95, no. 25, pp. 1–7, 2016.

[46] I. Mowat, E. Todman, and S. Jaggar, "Validation of the LiDCO™ pulse contour system in patients with impaired left ventricular function.," *Anaesthesia*, vol. 67, no. 2, p. 188; author reply 188-9, Feb. 2012.

[47] B. Mora, I. Ince, B. Birkenberg, K. Skhirtladze, E. Pernicka, H. J. Ankersmit, and M. Dworschak, "Validation of cardiac output measurement with the LiDCO™ pulse contour system in patients with impaired left ventricular function after cardiac surgery.," *Anaesthesia*, vol. 66, no. 8, pp. 675–81, Aug. 2011.

[48] M. D. Wiles, W. J. D. Whiteley, C. G. Moran, and I. K. Moppett, "The use of LiDCO based fluid management in patients undergoing hip fracture surgery under spinal anaesthesia: neck of femur optimisation therapy - targeted stroke volume (NOTTS): study protocol for a randomized controlled trial.," *Trials*, vol. 12, p. 213, 2011.

[49] M. G. Costa, P. Chiarandini, L. Scudeller, L. Vetrugno, L. Pompei, G. Serena, S. Buttera, and G. Della Rocca, "Uncalibrated continuous cardiac output measurement in liver transplant patients: LiDCOrapid™ system versus pulmonary artery catheter.," *J. Cardiothorac. Vasc. Anesth.*, vol. 28, no. 3, pp. 540–6, Jun. 2014.

[50] M. Nakasuji, A. Okutani, T. Miyata, N. Imanaka, M. Tanaka, K. Nakasuji, and M. Nagai, "Disagreement between fourth generation FloTrac and LiDCOrapid measurements of cardiac output and stroke volume variation during laparoscopic colectomy," *J. Clin. Anesth.*, vol. 35, pp. 150–156, Dec. 2016.

[51] K. Suehiro, K. Tanaka, M. Mikawa, Y. Uchihara, T. Matsuyama, T. Matsuura, T. Funao, T. Yamada, T. Mori, and K. Nishikawa, "Improved performance of the fourth-generation FloTrac/Vigileo system for tracking cardiac output changes.," *J. Cardiothorac. Vasc. Anesth.*, vol. 29, no. 3, pp. 656–62, 2015.

[52] J.-H. Chin, W.-J. Kim, J.-H. Choi, Y. A. Han, S.-O. Kim, and W.-J. Choi, "Unreliable tracking ability of the third-generation FloTrac/Vigileo™ system for changes in stroke volume after fluid administration in patients with high systemic vascular resistance during laparoscopic surgery," *PLoS One*, vol. 10, no. 11, p. e0142125, 2015.

[53] J.-Y. Kim, B.-R. Kim, K.-H. Lee, K.-W. Kim, J.-H. Kim, S.-I. Lee, K.-T. Kim, W.-J. Choe, J.-S. Park, and J.-W. Kim, "Comparison of cardiac output derived from FloTrac™/Vigileo™ and impedance cardiography during major abdominal surgery.," *J. Int. Med. Res.*, vol. 41, no. 4, pp. 1342–9, 2013.

[54] S. J. Davies, S. Minhas, R. J. T. Wilson, D. Yates, and S. J. Howell, "Comparison of stroke volume and fluid responsiveness measurements in commonly used technologies for goal-directed therapy.," *J. Clin. Anesth.*, vol. 25, no. 6, pp. 466–74, Sep. 2013.

[55] S. B. Nicia, T. A. Van Veelen, J. Stens, M. M. W. Koopman, and C. Boer, "Detection of volume loss using the Nexfin device in blood donors," *Anaesthesia*, vol. 71, no. 2, pp. 163–170, 2016.

[56] J. J. Vos, M. Poterman, P. P. Salm, K. Van Amsterdam, M. M. R. F. Struys, T. W. L. Scheeren, and A. F. Kalmar, "Noninvasive pulse pressure variation and stroke volume variation to predict fluid responsiveness at multiple thresholds: a prospective observational study," *Can. J. Anesth. Can. d'anesthésie*, vol. 62, no. 11, pp. 1153–1160, 2015.

[57] J. Y. Wagner, J. Grond, J. Fortin, I. Negulescu, M. Schöfthaler, and B. Saugel, "Continuous noninvasive cardiac output determination using the CNAP system: evaluation of a cardiac output algorithm for the analysis of volume clamp method-derived pulse contour," *J. Clin. Monit. Comput.*, vol. 30, no. 4, pp. 487–493, Aug. 2016.

[58] C. Ilies, G. Grudev, J. Hedderich, J. Renner, M. Steinfath, B. Bein, N. Haake, and R. Hanss, "Comparison of a continuous noninvasive arterial pressure device with invasive measurements in cardiovascular postsurgical intensive care patients: A prospective observational study.," *Eur. J. Anaesthesiol.*, vol. 32, no. 1, pp. 20–8, 2015.

[59] S. Scolletta, F. Franchi, S. Romagnoli, R. Carl&#224, A. Donati, L. P. Fabbri, F. Forfori, Jos&#233, S. Laviola, V. Mangani, G. Maj, G. Martinelli, L. Mirabella, A. Morelli, P. Persona, and D. Payen, "Comparison between doppler-echocardiography and uncalibrated pulse contour method for cardiac output measurement: a multicenter observational study," *Crit. Care Med.*, vol. 44, no. 7, pp. 1370–1379, 2016.

[60] Y. Sugo, T. Ukawa, S. Takeda, H. Ishihara, T. Kazama, and J. Takeda, "A novel continuous cardiac output monitor based on pulse wave transit time.," *Conf. Proc. IEEE Eng. Med. Biol. Soc.*, vol. 2010, no. C, pp. 2853–2856, 2010.

[61] H. Ishihara, Y. Sugo, M. Tsutsui, T. Yamada, T. Sato, T. Akazawa, N. Sato, K. Yamashita, and J. Takeda, "The ability of a new continuous cardiac output monitor to measure trends in cardiac output following implementation of a patient information calibration and an automated exclusion algorithm," *J. Clin. Monit. Comput.*, vol. 26, no. 6, pp. 465–471, 2012.

[62] S. a Smith, a E. Russell, M. J. West, and J. Chalmers, "Automated non-invasive measurement of cardiac output: comparison of electrical bioimpedance and carbon dioxide rebreathing techniques.," *Br. Heart J.*, vol. 59, pp. 292–298, 1988.

[63] C. K. Hofer, S. Rex, and M. T. Ganter, "Update on minimally invasive hemodynamic monitoring in thoracic anesthesia.," *Curr. Opin. Anaesthesiol.*, vol. 27, no. 1, pp. 28–35, 2014.

[64] C. L. Parmley and R. M. Pousman, "Noninvasive cardiac output monitoring," pp. 675–680.

[65] M. H. Drazner, B. Thompson, P. B. Rosenberg, P. A. Kaiser, J. D. Boehrer, B. J. Baldwin, D. L. Dries, and C. W. Yancy, "Comparison of impedance cardiography with invasive hemodynamic measurements in patients with

heart failure secondary to ischemic or nonischemic cardiomyopathy," *Am. J. Cardiol.*, vol. 89, no. 8, pp. 993–995, 2002.

[66] B. D. Spiess, M. a. Patel, L. O. Soltow, and I. H. Wright, "Comparison of bioimpedance versus thermodilution cardiac output during cardiac surgery: Evaluation of a second-generation bioimpedance device," *J. Cardiothorac. Vasc. Anesth.*, vol. 15, no. 5, pp. 567–573, 2001.

[67] R. Simon, O. Desebbe, R. Henaine, O. Bastien, J.-J. Lehot, and M. Cannesson, "Comparaison des valeurs de debit cardiaque obtenues a l'aide d'un nouveau systeme d'impedancemetrie thoracique avec les donnees du catheter arteriel pulmonaire en postoperatoire de chirurgie cardiaque. [Comparison of ICG thoracic bioimpedance cardiac outp," *Ann. Fr. Anesth. Reanim.*, vol. 28, no. 6, pp. 537–541, 2009.

[68] F. Trinkmann, M. Berger, C. Doesch, T. Papavassiliu, S. O. Schoenberg, M. Borggrefe, J. J. Kaden, and J. Saur, "Comparison of electrical velocimetry and cardiac magnetic resonance imaging for the non-invasive determination of cardiac output," *J. Clin. Monit. Comput.*, 2015.

[69] T. W. Jones, D. Houghton, S. Cassidy, G. a. MacGowan, M. I. Trenell, and D. G. Jakovljevic, "Bioreactance is a reliable method for estimating cardiac output at rest and during exercise," *Br. J. Anaesth.*, pp. 1–2, 2015.

[70] O. Broch, J. Carbonell, C. Ferrando, M. Metzner, A. Carstens, M. Albrecht, M. Gruenewald, J. Höcker, M. Soro, M. Steinfath, J. Renner, and B. Bein, "Accuracy of an autocalibrated pulse contour analysis in cardiac surgery patients: a bi-center clinical trial," *BMC Anesthesiol.*, vol. 15, no. 1, p. 171, 2015.

[71] L. J. Montenij, W. F. Buhre, S. A. de Jong, J. H. Harms, J. A. van Herwaarden, C. L. J. J. Kruitwagen, and E. E. C. de Waal, "Arterial pressure waveform analysis versus thermodilution cardiac output measurement during open abdominal aortic aneurysm repair: a prospective observational study.," *Eur. J. Anaesthesiol.*, vol. 32, no. 1, pp. 13–9, 2015.

[72] M. Cecconi, A. Rhodes, J. Poloniecki, G. Della Rocca, and R. M. Grounds, "Bench-to-bedside review: the importance of the precision of the reference technique in method comparison studies--with specific reference to the measurement of cardiac output.," *Crit. Care*, vol. 13, no. 1, p. 201, Jan. 2009.

[73] M. Cecconi, D. Dawson, R. M. Grounds, and A. Rhodes, "Lithium dilution cardiac output measurement in the critically ill patient: Determination of precision of the technique," *Intensive Care Med.*, vol. 35, no. 3, pp. 498–504, 2009.

[74] P. Squara, D. Denjean, P. Estagnasie, A. Brusset, J. C. Dib, C. Dubois, P. Squara, D. Denjean, P. Estagnasie, A. Brusset, J. C. Dib, and · C Dubois, "Noninvasive cardiac output monitoring (NICOM): a clinical validation,"

Intensive Care Med, vol. 33, pp. 1191–1194, 2007.

[75] I. Sergeev, S. Schookin, O. Rutkovsky, and O. Medvedev, "Method of noninvasive impedance monitoring of the cardiovascular system parameters," in *3rd Russian-Bavarian Conference on Biomedical Engineering*, 2007.

[76] N. M. Albert, "Bioimpedance cardiography measurements of cardiac output and other cardiovascular parameters," *Crit. Care Nurs. Clin. North Am.*, vol. 18, pp. 195–202, 2006.

[77] L. A. H. Critchley, Y. Zhang, J. A. J. H. Critchley, and R. C. K. Chung, "A comparison of two impedance cardiographs using head-up tilting and trend analysis," *J. Clin. Monit. Comput.*, vol. 17, no. 2, pp. 153–160, 2002.

[78] H. H. Woltjer, H. J. Bogaard, and P. M. J. M. de Vries, "The technique of impedance cardiography," *Eur. Heart J.*, vol. 18, no. 9, pp. 1396–1403, Sep. 1997.

[79] L. a H. Critchley and J. a J. H. Critchley, "A meta-analysis of studies using bias and precision statistics to compare cardiac output measurement techniques," *J. Clin. Monit. Comput.*, vol. 15, no. 2, pp. 85–91, 1999.

[80] L. a. Critchley, A. Lee, and A. M. H. Ho, "A critical review of the ability of continuous cardiac output monitors to measure trends in cardiac output," *Anesth. Analg.*, vol. 111, no. 5, pp. 1180–1192, 2010.

[81] J. Bland and D. Altman, "Statistical methods for assessing agreement between two methods of clinical measurement," *Lancet*, vol. 1, pp. 307–10, 1986.

[82] J. M. Bland and D. G. Altman, "Agreement between methods of neasurement with nultiple observations per individual," *J. Biopharm. Stat.*, vol. 17, no. 4, pp. 571–582, 2007.

[83] P. S. Myles and J. Cui, "Using the Bland-Altman method to measure agreement with repeated measures," *Br. J. Anaesth.*, vol. 99, no. 3, pp. 309–311, 2007.

[84] a C. Perrino, J. Fleming, and K. R. LaMantia, "Transesophageal Doppler cardiac output monitoring: performance during aortic reconstructive surgery.," *Anesth. Analg.*, vol. 73, no. 6, pp. 705–710, 1991.

[85] W. D. Simith, R. C. Dutton, and N. T. Smith, "Measuring the performance of anesthetic depth indicators," *Am. Soc. Anesthesiol.*, 1996.

[86] E. Jensen, P. L. Gambus, P. Pineda, J. F. Valencia, M. Jospin, Struys, and H. E. M. Vereecke, "Prediction of response to tetanic stimulation : what is best , an interaction model or a direct brain measurement ?," pp. 0–1.

[87] E. W. Jensen, J. F. Valencia, a. López, T. Anglada, M. Agustí, Y. Ramos, R. Serra, M. Jospin, P. Pineda, and P. Gambus, "Monitoring hypnotic effect and nociception with two EEG-derived indices, qCON and qNOX, during

general anaesthesia," *Acta Anaesthesiol. Scand.*, vol. 58, no. 8, pp. 933–941, 2014.

[88] J. Fontanet, E. Gabarrón, M. Jospin, M. Vallverdú, P. L. Gambus, and E. W. Jensen, "Comparison of the qNOX and ANI indices of nociception during propofol and remifentanil anaesthesia," no. Esgco, pp. 243–244, 2014.

[89] J. Fontanet, E. W. Jensen, M. Jospin, E. Gabarrón, M. Vallverdú, and P. L. Gambús, "The effect of nociceptive stimulation on the qNOX and qCON," in *23rd International Society for Anaesthetic Pharmacology Annual Meeting*, 2014, no. October.

[90] P. P. Pineda, "Reduction of propofol influence on the qNOX pain / nociception index .," vol. 99, no. 4, p. 2011, 2011.

[91] J. Fernández-Candil, E. Vila, S. Pancreu, M. Lamora, and P. L. Gambús, "Establishing loss of consciousness by changes in EEG Propofol concentration and clinical correlates," in *Euro-Neuro 2014*, 2014.

[92] B. Musizza, A. Stefanovska, P. McClintock, M. Palus, J. Petrov, S. Ribaric, and F. Bajrovic, "Interactions between cardiac, respiratory and EEG-δ oscillations in rats during anaesthesia," *Physiology*, vol. 580, no. 1, 2007.

[93] M. Steriade, A. Nuñez, and F. Amzica, "A novel slow (< 1 Hz) oscillation of neocortical neurons in vivo: depolarising and hyperpolarising components," *J. Neurosci.*, vol. 13, 1993.

[94] C. F. Minto, T. W. Schnider, and S. L. Shafer, "Pharmacokinetics and pharmacodynamics of remifentanil. II. Model application.," *Anesthesiology*, vol. 86, no. 1, pp. 24–33, Jan. 1997.

[95] T. W. Schnider, C. F. Minto, S. L. Shafer, and P. L. Gambus, "The influence of age on propofol pharmacodynamics," *Anesthesiology*, vol. 90, no. 6, pp. 1502–1516, 1990.

[96] Pan and Tompkins, "A real-time QRS detection algorithm," *IEEE Trans. Biomed. Eng.*, vol. 3, pp. 230–6, 1985.

[97] R. E. Klabunde, *Cardiovascular Physiology Concepts*, Second Edi. 2012.

[98] M. Kluckow and N. Evans, "Relationship between blood pressure and cardiac output in preterm infants requiring mechanical ventilation," *J Pediatr*, vol. 129, no. 4, pp. 506–512, 1996.

[99] R. Katori, "Normal cardiac output in relation to age and body size," *Tohoku J. Exp. Med.*, vol. 128, no. 4, pp. 377–387, 1979.

[100] M. Brandfonbrener, M. Landowne, and N. W. Shock, "Changes in cardiac output with age," *Circulation*, vol. 12, no. 4, pp. 557–566, Oct. 1955.

[101] G. Boss and J. Seegmiller, "Age-related physiological changes and their

clinical significance," *West. J. Med.*, vol. 135, no. 6, pp. 434–440, 1981.

[102] E. Gabarrón, J. Escrivá, M. Jospin, E. W. Jensen, and P. L. Gambús, "Non-invasive cardiac output measurement by impedance plethysmography under general anaesthesia," in *Euroanaesthesia, European Society of Anaesthesiology (ESA)*, 2015, pp. 4–6.

[103] S. Hidaka, M. Kawamoto, S. Kurita, and O. Yuge, "Comparison of the effects of propofol and midazolam on the cardiovascular autonomic nervous system during combined spinal and epidural anesthesia," *J. Clin. Anesth.*, vol. 17, no. 1, pp. 36–43, 2005.

[104] J. M. Huston and K. J. Tracey, "The pulse of inflammation: heart rate variability, the cholinergic anti-inflammatory pathway, and implications for therapy," *J Intern Med.*, vol. 269, no. 1, pp. 45–53, 2011.

[105] R. Lampert, J. D. Bremmer, S. Su, A. Miller, F. Lee, F. Cheema, J. Goldberg, and V. Vaccarino, "Decreased heart rate variability is associated with higher levels of inflammation in middle-aged men," *Am. Heart J.*, vol. 156, no. 4, p. 759.e1-7, 2008.

[106] R. P. Sloan, M. Heather, and K. J. Travey, "RR interval variability is inversely related to inflammatory markers: the CARDIA study," *Mol. Med. Cambridge Mass*, vol. 13, pp. 30–39, 2007.

[107] Y. Momota, K. Kaneda, K. Arishiro, N. Kishimoto, S. Kanou, and J. Kotani, "Changes in blood pressure during induction of anesthesia and oral and maxillofacial surgery by type and timing of discontinuation of antihypertensive drugs.," *Anesth. Prog.*, vol. 57, no. 10, pp. 13–17, 2010.

[108] A. C. Guyton, "The relationship of cardiac output and arterial pressure control.," *Circulation*, vol. 64, no. 6, pp. 1079–1088, 1981.

[109] P. Salvi, *Pulse Waves*, vol. 1. Springer, 2012.

[110] S. M. Musa, I. Adam, and M. F. Lutfi, "Heart rate variability and autonomic modulations in preeclampsia," *PLoS One*, vol. 11, no. 4, 2016.

[111] P. A. Lotufo, L. Valiengo, I. M. Benseñor, and A. R. Brunoni, "A systematic review and meta-analysis of heart rate variability in epilepsy and antiepileptic drugs," *Epilepsia*, vol. 53, no. 2, pp. 272–282, Feb. 2012.

[112] A. R. Burton, A. Fazalbhoy, and V. G. Macefield, "Sympathetic responses to noxious stimulation of muscle and skin," *Front. Neurol.*, vol. 7, p. 109, 2016.

[113] Hadase M Azuma A Zen K Asada S Kawasaki T et. al., "Very low frequency power of heart rate variability is a powerful predictor of clinical prognosis in patients with congestive heart failure.," *Circ. J.*, vol. 68, 2004.

[114] A. Shu, L. Zhan, H. Fang, E. Lv, X. Chen, M. Zhang, and Q. Wang, "Evaluation of remifentanil anesthesia for off-pump coronary artery bypass grafting surgery using heart rate variability," *Exp. Ther. Med.*, vol. 6, no. 1, pp.

253–259, 2013.

[115] S. B. Park, B. C. Lee, and K. S. Jeong, "Standarized tests of heart rate varibility for autonomic function tests in healthy koreans," *Int. J. Neurosci.*, vol. 117, no. 12, pp. 1707–1717, Jan. 2007.

[116] M. Pagani, F. Lombardi, S. Guzzetti, O. Rimoldi, R. Furlan, P. Pizzinelli, G. Sandrone, G. Malfatto, S. Dell'Orto, and E. Piccaluga, "Power spectral analysis of heart rate and arterial pressure variabilities as a marker of sympatho-vagal interaction in man and conscious dog.," *Circ. Res.*, vol. 59, no. 2, 1986.

[117] R. H. Fagard, "A population-based study on the determinants of heart rate and heart rate variability in the frequency domain.," *Verh. K. Acad. Geneesk. Belg.*, vol. 63, no. 1, pp. 57-89–1, 2001.

[118] G. Piccirillo, F. L. Fimognari, E. Viola, and V. Marigliano, "Age-adjusted normal confidence intervals for heart rate variability in healthy subjects during head-up tilt.," *Int. J. Cardiol.*, vol. 50, no. 2, pp. 117–24, Jun. 1995.

[119] W. Kubicek and R. P. Patterson, "Impedance cardiography as a non-invasive method of monitoring cardiac functions and other parameters of the cardiovascular system," *Ann. New York Acad. Sci.*, pp. 724–732, 1970.

[120] J. Malnivuo and R. Plonesey, *Bioelectromagnetism: principles and applications of bioelectric and biomagnetic fields*. Oxford University Press, 1995.

[121] W. G. Kubicek, R. P. Patterson, and D. A. Witsoe, "Impedance cardiography as a noninvasive method of monitoring cardiac function and other parameters of the cardiovascular system," *Ann. N. Y. Acad. Sci.*, vol. 170, pp. 724–732, 1970.

[122] J. H. Meijer, S. Boesveldt, E. Elbertse, and H. W. Berendse, "Using time interval parameters from impedance cardiography to evaluate autonomic nervous function in Parkinson's disease," *IFMBE Proc.*, vol. 17, p. 596, 2007.

[123] M. Cieslak, W. S. Ryan, A. Macy, R. M. Kelsey, J. E. Cornick, M. Verket, J. Blascovich, and S. Grafton, "Simultaneous acquisition of functional magnetic resonance images and impedance cardiography," *Psychophysiology*, vol. 52, no. 4, pp. 481–488, 2015.

[124] D. B. Newlin and R. W. Levenson, "Pre-ejection period: measuring beta-adrenergic influences upon the heart.," *Psychophysiology*, vol. 16, no. 6, pp. 546–553, 1979.

[125] K. A. M. Janssens, H. Riese, A. M. Van Roon, J. A. M. Hunfeld, P. F. C. Groot, A. J. Oldehinkel, and J. G. M. Rosmalen, "Are cardiac autonomic nervous system activity and perceived stress related to functional somatic symptoms in adolescents? The TRAILS study," *PLoS One*, vol. 11, no. 4, pp.

1–12, 2016.

[126] A. E. Van Dijk, R. Van Lien, M. Van Eijsden, R. J. B. J. Gemke, T. G. M. Vrijkotte, and E. J. De Geus, "Measuring cardiac autonomic nervous system (ANS) activity in children.," *J. Vis. Exp.*, no. 74, p. e50073, 2013.

[127] R. Talley, J. Meyer, and J. McNay, "Evaluation of the pre-ejection period as an estimate of myocardial contractility in dogs," *The American Journal of Cardiology*, pp. 384–391, 1971.

[128] H. Ashouri, L. Orlandic, and O. T. Inan, "Unobtrusive estimation of cardiac contractility and stroke volume changes using ballistocardiogram measurements on a high bandwidth force plate," *Sensors (Switzerland)*, vol. 16, no. 6, 2016.

[129] E. Generaal, N. Vogelzangs, G. J. Macfarlane, R. Geenen, J. H. Smit, E. J. C. de Geus, J. Dekker, and B. W. Penninx, "Biological stress systems, adverse life events, and the improvement of chronic multisite musculoskeletal pain across a 6-year follow-up," *J. Pain*, vol. 18, no. 2, pp. 155–165, 2017.

[130] S. Duschek, A. Hoffmann, G. A. Reyes del Paso, and U. Ettinger, "Autonomic cardiovascular control and executive function in chronic hypotension," *Ann. Behav. Med.*, vol. 51, no. 3, pp. 442–453, 2017.

[131] J. D. Biesheuvel, M. G. Vervloet, R. M. Verdaasdonk, and J. Meijer, "Initial Systolic Time Interval (ISTI) as a Predictor of Intradialytic Hypotension (IDH)," *J. Phys. Conf. Ser.*, vol. 434, p. 12036, 2013.

[132] J. H. Meijer, S. Boesveldt, E. Elbertse, and H. W. Berendse, "Method to measure autonomic control of cardiac function using time interval parameters from impedance cardiography.," *Physiol. Meas.*, vol. 29, no. 6, pp. S383-91, 2008.

[133] F. Hoekstra, E. Habers, T. W. J. Janssen, R. M. Verdaasdonk, and J. H. Meijer, "Relationship between the initial systolic time interval and RR-interval during an exercise stimulus measured with impedance cardiography," *J. Phys. Conf. Ser.*, vol. 224, no. April, pp. 2–5, 2010.

[134] J. H. Meijer, F. Hoekstra, E. Habers, R. M. Verdaasdonk, and T. W. J. Janssen, "Dynamic response of the initial systolic time interval to a breathing stimulus measured with impedance cardiography," *J. Phys. Conf. Ser.*, vol. 224, p. 12119, 2010.

[135] A. Smorenberg, E. J. Lust, R. M. Verdaasdonk, a B. J. Groeneveld, and J. H. Meijer, "Prediction and monitoring of fluid responsiveness after coronary bypass surgery using the Initial Systolic Time Interval: Preliminary results," *J. Phys. Conf. Ser.*, vol. 224, no. April, p. 12122, 2010.

[136] A. Smorenberg, E. J. Lust, A. Beishuizen, J. H. Meijer, R. M. Verdaasdonk, and A. B. J. Groeneveld, "Systolic time intervals vs invasive predictors of fluid responsiveness after coronary artery bypass surgery.," *Eur. J. Cardiothorac.*

Surg., vol. 44, no. 5, pp. 891–7, 2013.

[137] M. A. J. M. Van Eijnatten, M. J. Van Rijssel, R. J. A. Peters, R. M. Verdaasdonk, and J. H. Meijer, "Comparison of cardiac time intervals between echocardiography and impedance cardiography at various heart rates," *J. Electr. Bioimpedance*, vol. 5, no. 1, pp. 2–8, 2014.

[138] R. Van Lien, N. M. Schutte, J. H. Meijer, and E. J. C. de Geus, "Estimated preejection period (PEP) based on the detection of the R-wave and dZ/dt-min peaks does not adequately reflect the actual PEP across a wide range of laboratory and ambulatory conditions," *Int. J. Psychophysiol.*, vol. 87, no. 1, pp. 60–69, 2013.

[139] J. D. Biesheuvel, M. G. Vervloet, R. M. Verdaasdonk, and J. Meijer, "Initial systolic time interval (ISTI) as a predictor of intradialytic hypotension (IDH)," *J. Phys. Conf. Ser.*, vol. 434, p. 12036, 2013.

[140] J. Muehlsteff, X. L. Aubert, and M. Schuett, "Cuffless estimation of systolic blood pressure for short effort bicycle tests: The prominent role of the pre-ejection period," *Annu. Int. Conf. IEEE Eng. Med. Biol. - Proc.*, pp. 5088–5092, 2006.

[141] M. Wong and Y. T. Zhang, "The effects of pre-ejection period on the blood pressure estimation using pulse transit time," *2008 5th Int. Summer Sch. Symp. Med. Devices Biosens.*, pp. 254–255, 2008.

[142] T. L. Whitsett and L. I. Goldberg, "Effects of levodopa on systolic preejection period, blood pressure, and heart rate during acute and chronic treatment of Parkinson's disease.," *Circulation*, vol. 45, no. 1, pp. 97–106, 1972.

[143] R. Shannon, K. Maher, J. Satinga, H. Royal, and J. Wei, "Comparison of differences in the hemodynamic response to passive postural stress in healthy subjects greater than 70 years and less than 30 years of age.," *Am. J. Cardiol.*, vol. 67, no. 13, pp. 1110–1116, 1991.

[144] A. Sherwood, M. Allen, P. Obrist, and A. Langer, "Evaluation of beta-adrenergic influences on cardiovascular and metabolic adjustments to physical and psychological stress.," *Psychophysiology*, vol. 23, no. 1, pp. 89–104, 1986.

[145] N. Westerhof, J.-W. Lankhaar, and B. E. Westerhof, "The arterial windkessel," *Med. Biol. Eng. Comput.*, pp. 131–141, 2009.

[146] J. H. Meijer, E. Elbertse, S. Boesveldt, H. W. Berendse, and R. M. Verdaasdonk, "Using the Initial Systolic Time Interval to assess cardiac autonomic function in Parkinson's disease," *J. Electr. Bioimpedance*, vol. 2, no. 1, pp. 98–101, 2011.

[147] L. Y. Shyu, Y. S. Lin, C. P. Liu, and W. C. Hu, "The detection of impedance

cardiogram characteristic points using wavelet transform," *Comput. Biol. Med.*, vol. 34, no. 2, pp. 165–175, 2004.

[148] S. Chabchoub, S. Mansouri, and R. Ben Salah, "Impedance cardiography signal denoising using discrete wavelet transform," *Australas. Phys. Eng. Sci. Med.*, vol. 39, no. 3, pp. 655–663, 2016.

[149] B. Boashash, G. Azemi, and J. M. O'Toole, "Time-frequency processing of nonstationary signals: Advanced tfd design to aid diagnosis with highlights from medical applications," *IEEE Signal Process. Mag.*, vol. 30, no. 6, pp. 108–119, 2013.

[150] B. Boashash and M. Mesbah, "A time-frequency approach for newborn seizure detection," *IEEE Eng. Med. Biol. Mag.*, vol. 20, no. 5, pp. 54–64, 2001.

[151] N. Stevenson, M. Mesbah, and B. Boashash, "Quadratic time-frequency distribution selection for seizure detection in the newborn.," in *IEEE Engineering in Medicine and Biology Society Conference*, 2008, pp. 923–6.

[152] B. Boashash, N. Ali, T. Ben-jabeur, N. A. Khan, and T. Ben-jabeur, "Time-frequency features for pattern recognition using high-resolution TFDs: A tutorial review," *Digit. Signal Process.*, vol. 40, pp. 1–30, 2015.

[153] L. Rankine, M. Mesbah, and B. Boashash, "A matching pursuit-based signal complexity measure for the analysis of newborn EEG," *Med. Biol. Eng. Comput.*, vol. 45, no. 3, pp. 251–260, 2007.

[154] L. Rankine, N. Stevenson, M. Mesbah, and B. Boashash, "A nonstationary model of newborn EEG," *IEEE Trans. Biomed. Eng.*, vol. 54, no. 1, pp. 19–28, 2007.

[155] U. Melia, M. Vallverdú, F. Clariá, J. Valls-Solé, and P. Caminal, "Auditory and nociceptive stimuli responses in the electroencephalogram," *Methods Inf. Med.*, vol. 54, no. 3, pp. 209–214, 2014.

[156] F. Clariá, M. Vallverdú, J. Riba, S. Romero, M. J. Barbanoj, and P. Caminal, "Characterization of the cerebral activity by time-frequency representation of evoked EEG potentials.," *Physiol. Meas.*, vol. 32, no. 8, pp. 1327–1346, 2011.

[157] H. H. Huang, H. L. Chan, P. L. Lin, C. P. Wu, and C. H. Huang, "Time-frequency spectral analysis of heart rate variability during induction of general anaesthesia," *Br. J. Anaesth.*, vol. 79, pp. 754–758, 1997.

[158] H.-L. Chan, H.-H. Huang, and J.-L. Lin, "Time-frequency analysis of heart rate variability during transient segments," *Ann. Biomed. Eng.*, vol. 29, no. 11, pp. 983–996, 2001.

[159] N. Aimie-salleh, M. B. Malarvili, and A. C. Phillip, "Quantitative comparison of time frequency distribution for heart rate variability using performance measure," *J. Wirel. Netw. Commun.*, vol. 5, no. 2A, pp. 1–5, 2015.

[160] M. Orini, R. Bailón, L. Mainardi, and P. Laguna, "Synthesis of HRV signals

characterized by predetermined time-frequency structure by means of time-varying ARMA models," *Biomed. Signal Process. Control*, vol. 7, no. 2, pp. 141–150, 2012.

[161] M. B. Malarvili, M. Mesbah, and B. Boashash, "Time-frequency analysis of heart rate variability for neonatal seizure detection," *EURASIP J. Adv. Signal Process.*, vol. 2007, 2007.

[162] G. Blain, O. Meste, A. Blain, and S. Bermon, "Time-frequency analysis of heart rate variability reveals cardiolocomotor coupling during dynamic cycling exercise in humans.," *Am. J. Physiol. Heart Circ. Physiol.*, vol. 296, no. 5, pp. H1651–H1659, 2009.

[163] a F. Quiceno-Manrique, J. B. Alonso-Hernández, C. M. Travieso-González, M. a Ferrer-Ballester, and G. Castellanos-Domínguez, "Detection of obstructive sleep apnea in ECG recordings using time-frequency distributions and dynamic features.," *Conf. Proc. IEEE Eng. Med. Biol. Soc.*, vol. 2009, pp. 5559–5562, 2009.

[164] R. Yu and E. C. Tan, "Comparison of different time-frequency distributions in pitch detection," in *ICICS-PCM 2003 - Proceedings of the 2003 Joint Conference of the 4th International Conference on Information, Communications and Signal Processing and 4th Pacific-Rim Conference on Multimedia*, 2003, vol. 2, no. 1, pp. 817–821.

[165] M. N. Souza and P. Caloba, "A comparison between fourier and biological auditory based time-frequency distributions, applied to the speech signals," in *IEEE 39th Midwest Symposium on Circuits and Systems*, 1997, pp. 807–810.

[166] L. Shang, Z. M. Hussain, and R. Harris, "Performance of QTFDs in blind source separation of speech signals," in *Spread Spectrum Techniques and Applications, 2004 IEEE Eighth International Symposium on*, 2004, no. 2, pp. 905–908.

[167] B. Boashash, *Time-Frequency Signal Analysis and Processing: a Comprehensive Reference*. Elsevier, 2003.

[168] F. Hlawatsch and P. Flandrin, "The interference structure of the Wigner distribution and related time-frequency signal representation," in *The Wigner Distribution - Theory and Applications in Signal Processing*, 1997, pp. 59–133.

[169] V. Sucic and B. Boashash, "Parameter selection for optimising time-frequency distributions and measurements of time-frequency characteristics of non-stationary signals," in *Proc. IEEE Internat. Conf. on Acoustics, Speech and Signal Processing (ICASSP'01)*, 2001, vol. 6, pp. 3557–3560.

[170] V. Sucic and B. Boashash, "Optimisation algorithm for selecting quadratic time-frequency distributions: Performance results and calibration," in *6th International Symposium on Signal Processing and Its Applications, ISSPA 2001*, 2001,

vol. 1, pp. 331–334.

[171] D. L. Jones and T. W. Parks, "A high resolution data-adaptive time-frequency," *IEEE Trans. Acoust. Speech Signal Process.*, vol. 38, no. 12, pp. 2127–2135, 1990.

[172] L. Stanković, "Measure of some time-frequency distributions concentration," *Signal Processing*, vol. 81, no. 3, pp. 621–631, 2001.

[173] S. Pikula and P. Beně, "Comparison of measures of time-frequency distribution optimization," in *Ultra Modern Telecommunications and Control Systems and Workshops (ICUMT), 2016 8th International Congress on*, 2016, pp. 314–319.

[174] W. J. Williams, "Renyi information and signal-dependent optimal kernel design," *1995 Int. Conf. Acoust. Speech, Signal Process.*, vol. 2, pp. 997–1000, 1995.

[175] D. Boutana, M. Benidir, F. Marir, and B. Barkat, "A comparative study of some time-frequency distributions using Rényi criterion," in *13th European Signal Processing Conference: EUSIPCO'2005*, 2005, no. 2.

[176] L. Stankovic, "Method for time-frequency analysis," *IEEE Trans. Signal Process.*, vol. 42, no. 1, pp. 225–229, 1994.

[177] M. K. Emresoy and A. El-Jaroudi, "Iterative instantaneous frequency estimation and adaptive matched spectrogram," *Signal Processing*, vol. 64, pp. 157–165, 1998.

[178] L. J. Stanković and V. Katkovnik, "Instantaneous frequency estimation using higher order L-Wigner distributions with data-driven order and window length," *IEEE Trans. Inf. Theory*, vol. 46, no. 1, pp. 302–311, 2000.

[179] L. Stanković and V. Katkovnik, "The Wigner distribution of noisy signals with adaptive time-frequency varying window," *IEEE Trans. Signal Process.*, vol. 47, no. 4, pp. 1099–1108, Apr. 1999.

[180] Z. Hussain and B. Boashash, "Multi-component IF estimation," in *Proceedings of the Tenth IEEE Workshop on Statistical Signal and Array Processing (Cat. No.00TH8496)*, pp. 559–563.

[181] V. Sucic and B. Boashash, "An approach for selecting a real-life signal best-performing time-frequency distribution," in *Signal Processing and Its Applications, 2003. Proceedings. Seventh International Symposium on*, 2003, pp. 125–128.

[182] I. Djurovic and L. Stankoic, "Influence of high noise on the instantaneous frequency estimation using quadratic time-frequency distributions," *IEEE Signal Process. Lett.*, vol. 7, no. 11, pp. 317–319, Nov. 2000.

[183] B. Barkat and B. Boashash, "Instantaneous frequency estimation of polynomial FM signals using the peak of the PWVD: statistical performance in the presence of additive gaussian noise," *IEEE Trans. Signal Process.*, vol. 47, no. 9, pp. 2480–2490, 1999.

[184] V. Katkovnik and L. Stankovic, "Instantaneous frequency estimation using the Wigner distribution with varying and data-driven window length," *IEEE Trans. Signal Process.*, vol. 46, no. 9, pp. 2315–2325, 1998.

[185] I. Djurović and L. Stanković, "Influence of high noise on the instantaneous frequency estimation using quadratic time-frequency distributions," *IEEE Signal Process. Lett.*, vol. 7, no. 11, pp. 317–319, 2000.

[186] I. Djurović, V. Katkovnik, and Lj. Stanković, "Median filter based realizations of the robust time-frequency distributions," *Signal Processing*, vol. 81, no. 8, pp. 1771–1776, Aug. 2001.

[187] L. Stanković, "Analysis of noise in time-frequency distributions," *IEEE Signal Process. Lett.*, vol. 9, no. 9, pp. 286–289, 2002.

[188] P. J. Huber and E. Ronchetti, *Robust statistics*. Wiley, 2009.

[189] P. C. Choudhari and D. M. S. Panse, "Denoising of radial bioimpedance signals using adaptive wavelet packet transform and Kalman filter," *IOSR J. VLSI Signal Process.*, vol. 5, no. 1, pp. 1–8, 2015.

[190] R. Stepanov, S. Podtaev, P. Frick, and A. Dumler, "Beat-to-beat cardiovascular hemodynamic parameters based on wavelet spectrogram of impedance data," *Biomed. Signal Process. Control*, vol. 36, pp. 50–56, 2017.

[191] B. Boashash, L. Boubchir, and G. Azemi, "A methodology for time-frequency image processing applied to the classification of non- stationary multichannel signals using instantaneous frequency descriptors with application to newborn EEG signals," *J. Adv. Signal Proccessing*, vol. 117, pp. 1–21, 2012.

[192] M. Fani, G. Azemi, and B. Boashash, "EEG-based automatic epilepsy diagnosis using the instantaneous frequency with sub-band energies," *Int. Work. Syst. Signal Process. their Appl. WOSSPA*, pp. 187–190, May 2011.

[193] B. Boashash, L. Boubchir, and G. Azemi, "Improving the classification of newborn EEG time-frequency representations using a combined time-frequency signal and image approach," in *2012 11th International Conference on Information Science, Signal Processing and their Applications (ISSPA)*, 2012, pp. 280–285.

[194] S. Aviyente and W. J. Williams, "Minimum entropy time-frequency distributions," *IEEE Signal Process. Lett.*, vol. 12, no. 1, pp. 37–40, Jan. 2005.

[195] C. Shannon and W. Weaver, *The Mathematical Theory of Communication*. Urbana, Illinois: University of illinois Press, 1964.

[196] W. J. Williams, M. L. Brown, and A. O. Hero, "Uncertainty, information and time-frequency distributions," *Proc. SPIE Int. Soc. Opt. Eng.*, vol. 1566, pp.

144–156, 1991.

[197] R. G. Baraniuk, P. Flandrin, A. J. E. M. Janssen, and O. J. J. Michel, "Measuring time-frequency information content using the Renyi entropies," *IEEE Trans. Inf. Theory*, vol. 47, no. 4, pp. 1391–1409, May 2001.

[198] P. Flandrin, R. G. Baraniuk, and O. Michel, "Time-Frequency Complexity and Information," in *Proceedings of ICASSP '94. IEEE International Conference on Acoustics, Speech and Signal Processing*, 1994.

[199] B. Boashash, G. Azemi, N. A. Khan, and N. Ali Khan, "Principles of time–frequency feature extraction for change detection in non-stationary signals: Applications to newborn EEG abnormality detection," *Pattern Recognit.*, vol. 48, no. 3, pp. 616–627, 2014.

[200] R. Sun and Y. Wang, "Predicting termination of atrial fibrillation based on the structure and quantification of the recurrence plot," *Med. Eng. Phys.*, vol. 30, no. 9, pp. 1105–1111, 2008.

[201] F. Takens, *Dynamical Systems of Turbulence*. Berlin: Springer, 1981.

[202] F. Takens, "Detecting strange attractors in turbulence," *Lect. Notes Math.*, vol. 898, no. 366–381, 1981.

[203] B. Boashash and S. Ouelha, "Designing high-resolution time-frequency and time-scale distributions for the analysis and classification of non-stationary signals: a tutorial review with a comparison of features performance," *Digit. Signal Process.*, vol. 1, pp. 1–33, 2017.

[204] P. T. Walling and K. N. Hicks, "Nonlinear changes in brain dynamics during emergence from sevoflurane anesthesia: preliminary exploration using new software.," *Anesthesiology*, vol. 105, no. 5, pp. 927–35, Nov. 2006.

[205] E. Bradley and H. Kantz, "Nonlinear time-series analysis revisited," *Chaos*, vol. 25, no. 9, 2015.

[206] J.-S. R. Jang, C.-T. Sun, and E. Mizutani, "Neuro-Fuzzy And Soft Computing Jang: a computational approach to learning and machine intelligence." p. 640, 1997.

[207] M. Buragohain and C. Mahanta, "A novel approach for ANFIS modelling based on full factorial design," *Appl. Soft Comput. J.*, vol. 8, no. 1, pp. 609–625, 2008.

[208] T. Takagi and M. Sugeno, "Fuzzy Identification of Systems and Its Application to Modeling and Control," *Transaction on Systems, Man, and Cybernetics*, vol. 15. pp. 116–132, 1985.

[209] U. R. Acharya, K. P. Joseph, N. Kannathal, C. M. Lim, and J. S. Suri, "Heart rate variability: A review," *Med. Biol. Eng. Comput.*, vol. 44, pp. 1031–1051, 2006.

[210] J. Escrivá, E. Gabarrón, P. Fort, Y. Pan, G. Shengjin, Q. Liao, and M. Vallverdú Ferrer, "Comparison of two cardiac output monitors, qCO and LiDCO, during general anesthesia," *Mathews J. Anesth.*, vol. 1, no. 1, pp. 1–8, 2016.

[211] S. Huddart, C. J. Peden, M. Swart, B. McCormick, M. Dickinson, M. A. Mohammed, and N. Quiney, "Use of a pathway quality improvement care bundle to reduce mortality after emergency laparotomy," *Br. J. Surg.*, vol. 102, no. 1, pp. 57–66, Jan. 2015.

[212] T. E. Miller, J. K. Thacker, W. D. White, C. Mantyh, J. Migaly, J. Jin, A. M. Roche, E. L. Eisenstein, R. Edwards, K. J. Anstrom, R. E. Moon, and T. J. Gan, "Reduced length of hospital stay in colorectal surgery after implementation of an enhanced recovery protocol.," *Anesth. Analg.*, vol. 118, no. 5, pp. 1052–61, May 2014.

[213] Koff, M. Richard, M. R. Novak, M. Canneson, and T. M. Dodds, "Elevated PPV Predicts an Increased Length of Stay and Morbidity during High Risk Abdominal Surgery," in *Proceedings of the 2010 Annual Meeting of the American Society Anesthesiologists.*, 2010.

[214] B. Carstensen, J. Simpson, and L. C. Gurrin, "Statistical models for assessing agreement in method comparison studies with replicate measurements," *Int. J. Biostat.*, vol. 4, no. 1, pp. 1–26, 2008.

[215] J. M. Bland and D. G. Altman, "Measuring agreement in method comparison studies," *Stat. Methods Med. Res.*, vol. 8, no. 2, pp. 161–179, 1999.

[216] P. Squara, M. Cecconi, A. Rhodes, M. Singer, and J. D. Chiche, "Tracking changes in cardiac output: Methodological considerations for the validation of monitoring devices," *Intensive Care Med.*, vol. 35, no. 10, pp. 1801–1808, 2009.

[217] T. D. Phan, R. Kluger, C. Wan, D. Wong, and A. Padayachee, "A comparison of three minimally invasive cardiac output devices with thermodilution in elective cardiac surgery," *Anaesth. Intensive Care*, vol. 39, no. 6, pp. 1014–1021, Nov. 2011.

[218] M. Heringlake, U. Handke, T. Hanke, F. Eberhardt, J. Schumacher, H. Gehring, and H. Heinze, "Lack of agreement between thermodilution and electrical velocimetry cardiac output measurements," *Intensive Care Med*, vol. 33, pp. 2168–72, 2007.

[219] J. Truijen, J. J. van Lieshout, W. A. Wesselink, and B. E. Westerhof, "A recent meta-analysis comprehensively," *J. Clin. Monit. Comput.*, vol. 26, no. 4, pp. 267–78, Aug. 2012.

[220] J. D. Rich, S. L. Archer, and S. Rich, "Noninvasive cardiac output

measurements in patients with pulmonary hypertension.," *Eur. Respir. J.*, vol. 42, no. 1, pp. 125–33, Jul. 2013.

[221] M. Jospin, J. P. Aguilar, P. L. Gambus, E. W. Jensen, M. Vallverdu, and P. Caminal, "Validation of the qCO cardiac output monitor during Valsalva maneuver," *Proc. Annu. Int. Conf. IEEE Eng. Med. Biol. Soc. EMBS*, pp. 240–243, 2012.